SCIENCE CHINA
Physics, Mechanics & Astronomy

• Invited Review •
Special Topic: Advances in Pulsed Laser Synthesis of Nanoparticles in Liquids

July 2022 Vol. 65 No. 7: 274202
https://doi.org/10.1007/s11433-021-1835-x

Generation of nanomaterials by reactive laser-synthesis in liquid

Laysa M. Frias Batista, Ashish Nag, Victoria K. Meader, and Katharine Moore Tibbetts*

Department of Chemistry, Virginia Commonwealth University, Richmond VA 23284, USA

Received October 16, 2021; accepted December 15, 2021; published online April 11, 2022

Nanomaterials with tailored structures and surface chemistry are in high demand, as these materials play increasingly important roles in biology, catalysis, energy storage, and manufacturing. Their heightened demand has attracted attention towards the development of synthesis routes, particularly, laser-synthesis techniques. These efforts drove the refinement of laser ablation in liquid (LAL) and related methods over the past two decades and have led to the emergence of reactive laser-synthesis techniques that exploit these methods' characteristic, non-equilibrium conditions. Reactive laser-synthesis approaches foster unique chemical reactions that enable the formation of composite products like multimetallic nanoparticles, supported nanostructures, and complex minerals. This review will examine emerging reactive laser-synthesis methods in the context of established methods like LAL. The focus will be on the chemical reactions initiated within the laser plasma, with the goal of understanding how these reactions lead to the formation of unique nanomaterials. We will provide the first systematic review of laser reaction in liquid (LRL) in the literature, and bring a focus to the chemical reaction mechanisms in LAL and *reactive*-LAL techniques that have not yet been emphasized in reviews. Discussion of the current challenges and future investigative opportunities into reactive laser-synthesis will impart guidance for researchers interested in designing reactive laser-synthesis approaches to novel nanomaterial production.

laser ablation in liquids, laser reduction in liquids, nanoparticles

PACS number(s): 61.46.-w, 68.08.-p, 52.38.-r

Citation: L. M. Frias Batista, A. Nag, V. K. Meader, and K. M. Tibbetts, Generation of nanomaterials by reactive laser-synthesis in liquid, Sci. China-Phys. Mech. Astron. **65**, 274202 (2022), https://doi.org/10.1007/s11433-021-1835-x

1 Introduction

Laser synthesis and materials-processing enable industrial applications such as additive manufacturing [1-3] and 3D printing [4-6], as well as emerging platforms for nanophotonics [7], nanolithography [8], batteries [9], nanofluidic biochips [10], and bioprinting [11]. Although laser processing of solid materials is often performed under vacuum or simply in air, laser synthesis in liquid media has unique advantages for applications such as colloidal nanoparticle production. Colloidal nanoparticles are formed directly in the liquid medium upon ablation, and the liquid environment eliminates the formation of hazardous aerosols during laser-processing [12]. Moreover, laser synthesis in liquid satisfies "green chemistry" principles [13]. Toxic chemical reducing agents and surfactants are extraneous, and little if any hazardous chemical waste is produced [14]. For these reasons, laser-synthesis of nanomaterials in liquid has become an increasingly relevant area of research, as evidenced by the multitude of reviews and perspectives published in just the last decade [14-31] as well as the emergence of startup companies producing laser-synthesized nanoparticles [31].

*Corresponding author (email: kmtibbetts@vcu.edu)

Laser-synthesis in liquid is classified into three techniques that vary by target and laser-fluence (Figure 1, top). Laser ablation in liquid (LAL) targets a solid. High-fluence laser fragmentation in liquid (LFL) and low-fluence laser melting in liquid (LML) both target colloids or suspensions. The liquid media can be water or an organic solvent such as ethanol, acetone, or toluene. The targets are metals, alloys, semiconductors, or oxides. The array of liquid media and targets typically used for LAL, LFL, and LML is summarized in ref. [31]. LAL can simultaneously generate two nanoproducts: nanoparticles in solution, produced from material ablated off of the solid target; and nanostructures etched on the solid target surface [31]. LFL and LML use either commercial-grade powders that can be as large as microscale or nanoparticles generated through LAL, as their starting target. In LFL, high-fluence laser irradiation fragments the initial particles through surface-evaporation with nanosecond laser pulses, or Coulomb explosion with femtosecond pulses [20,32]. In contrast, LML uses low-fluence nanosecond pulses to produce sub-micron spheres from the starting material, through melting and diffusion coalescence of the initial particles [20, 33].

If the target material and resulting product have similar or identical compositions, then the synthesis avenue is considered a physical technique. Therefore, LAL, LFL, and LML are all considered physical synthesis techniques, generated by physical processes such as ablation, fragmentation, and melting; although chemical reactions do take place and are described in many other reviews [20, 22, 25, 31]. Reactive laser-synthesis techniques were honed to exploit the unique non-equilibrium chemistry initiated by laser excitation. These techniques include reactive laser ablation in liquid (RLAL), reactive laser fragmentation in liquid (RLFL), and laser reduction in liquid (LRL) (Figure 1, bottom). Although the acronyms "RLAL" and "RLFL" are often used to denote laser-synthesis involving *any* chemical reaction (e.g., metal oxidation in water) [20, 31], we wish to further narrow these definitions to describe a clearer set of goals. Hence, in this work, the terms "RLAL" and "RLFL" refer only to syntheses wherein molecular precursors like metal salts or complexes are added to the liquid medium for the purpose of inducing chemical reactions that will generate products with entirely distinct compositions from the starting materials. Such specifically designed reactive laser-synthesis thereby combines the physical processes induced by LAL and LFL with non-equilibrium chemical reactions driven by the decomposition of the liquid medium and the high, transient temperatures achieved in the laser plasma. This combination produces new composite nanomaterials with metastable phases, which often cannot be produced by other means. To avoid confusion throughout this review, please refer to Table 1 for clarifications about the terminology we will be using.

The present review highlights advances in reactive laser-synthesis, with a particular emphasis on the current state of knowledge about chemical reaction pathways and mechanisms that lead to nanomaterial formation. Because other reviews have already covered specific classes of laser-synthesized nanomaterials [27-29], their applications [22-24, 26, 30], and the physical mechanisms of laser ablation [21, 25], those topics will not be discussed in detail here. Instead, we will consider the reactive laser-synthesis literature from a chemical perspective, which we hope will bestow any laser-synthesis enthusiasts with physics and engineering backgrounds some degree of chemical intuition that can be applied to experimental or synthetic design strategies. Moreover, despite the extensive available information about the physical mechanisms of LAL, including initial material ejection on picosecond to nanosecond timescales [34-37], the formation and collapse of cavitation bubbles on microsecond timescales [38-40], and the growth of nanoparticles on microsecond to millisecond timescales [41-43], comparatively little is known about the chemical reactions occurring on these timescales. This knowledge-gap between physical and chemical properties presents an opportunity for future computational and experimental investigations to elucidate these reactions, improving control over the structures and properties of nanomaterials created through reactive laser-synthesis. We will highlight such opportunities throughout this review.

The remainder of this work is structured as follows: First, sect. 2 introduces the primary chemical reactions that occur upon laser-induced decomposition of water and organic

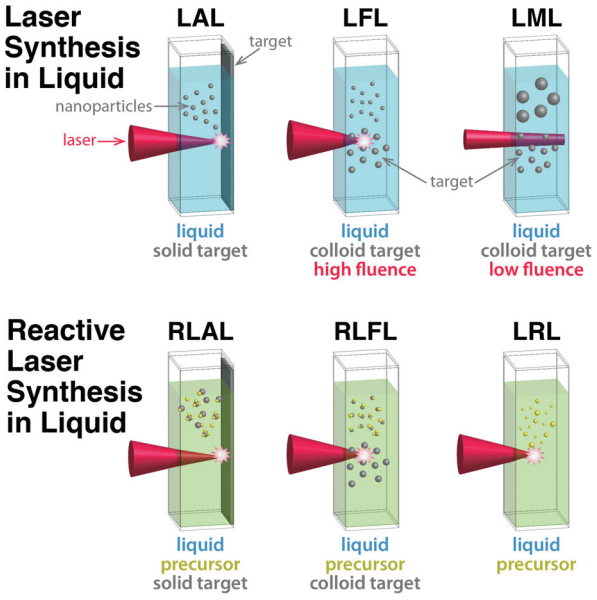

Figure 1 (Color online) Schematic illustration of laser-synthesis in liquid methods LAL, LFL, and LML (top) and reactive laser synthesis methods RLAL, RLFL, and LRL (bottom).

Table 1 For the purposes of this review LAL, LFL, and LML refer to primarily physical synthesis techniques, and their counterparts RLAL and RLFL refer to techniques with additional non-equilibrium chemical reactions facilitated by supplemental starting materials. Molecular precursors often, but not always, contain metal ions

Abbreviation	Term	Target material
LAL	laser ablation in liquid	solid
LFL	laser fragmentation in liquid	colloid/suspension
LML	laser melting in liquid	colloid/suspension
LRL	laser reduction in liquid	molecular precursor
RLAL	reactive laser ablation in liquid	solid and molecular precursor
RLFL	reactive laser fragmentation in liquid	colloid/suspension and molecular precursor

liquids. These reactions underlie all reactive laser-synthesis processes. Second, the consequences of these chemical reactions on LAL, LFL, and LML syntheses will be discussed through selected literature examples in sect. 3. Third, nanomaterials synthesized by LRL and its associated chemical reactions will be extensively reviewed in sect. 4, because this technique has received less attention in previous laser-synthesis reviews. Fourth, sect. 5 will cover the diverse array of nanomaterials that can be obtained from RLAL and RLFL syntheses using added molecular precursors, including their formation mechanisms when known or proposed. Finally, sect. 6 will present an outlook on the future of reactive laser-synthesis, highlighting the many opportunities for expanding the field.

2 Laser-induced chemical reactions in liquid

This section introduces the fundamental chemical reactions in both water and organic solvents, induced by interaction with intense, pulsed lasers. As will be discussed in sect. 3, these reactions have important effects on the products of LAL, LFL, and LML syntheses. Here, we will focus on the chemistry rather than the fundamental physics of laser-matter interactions in liquid. For more information on these processes, including plasma formation, plasma quenching in the liquid, and cavitation bubble dynamics, we refer interested readers to several excellent review articles [14, 25, 44, 45].

2.1 Reactions in water

The effects of intense laser pulses on water, including the physical mechanisms of water ionization and the temporal dynamics of the electron density in the plasma, have been investigated extensively by Vogel and collaborators [46-48], and have been reviewed already [49, 50]. Briefly, laser interaction with water produces a localized, weakly-ionized plasma. This plasma may produce optical breakdown, supercontinuum emission, or both. Optical breakdown of water occurs when the free-electron density, ρ_e, exceeds the critical value $\rho_e = 1.8 \times 10^{20}$ cm^{-3} [51]. Optical breakdown can be initiated in water by laser pulses with femtosecond through nanosecond pulse durations that meet particular peak-irradiance, and fluence requirements [48]. The fluence requirement for the optical breakdown in water when using nanosecond pulses is reduced substantially in the presence of metal nanoparticles [52, 53]. With pulses smaller than 100 fs, supercontinuum emission can occur at very low fluence, even below the optical breakdown threshold. In these conditions, supercontinuum emission will produce low-density plasma (LDP) with an electron density of $\rho_e \sim 1\times10^{18}$-$3\times10^{18}$ cm^{-3} and a broad spectral emission spanning the visible-near-IR range [54]. These plasmas, the high-density associated with optical breakdown, and low-density associated with supercontinuum emission, generate the chemical reactions described below. It should be noted that the same reactive chemical species are produced independently of laser pulse duration, although the specifics of water decomposition processes induced by femtosecond, picosecond, and nanosecond lasers may result in different relative yields of reaction products. Finally, we note that the laser-generated reaction products resemble those produced when water undergoes radiolysis with γ rays, high-energy electrons, and electrical discharges [55-57].

The interaction between intense visible or near-IR laser pulses and water triggers direct ionization through the absorption of n photons,

$$H_2O \xrightarrow{nh\nu} e^- + H_2O^{\bullet+} \quad (1)$$

to produce a free electron and a water radical cation, $H_2O^{\bullet+}$. The electron becomes hydrated, e^-_{aq}, on a timescale of ~300 fs [58]. The ultrafast emergence of the e^-_{aq} absorption band at ~800 nm can be resolved using the pump-probe technique of transient absorption spectroscopy with femtosecond laser pulses [58]. In pure water, e^-_{aq} has a lifetime of up to 100 ns as measured by flash photolysis [59], although its lifetime is substantially shortened in the presence of the electron scavenger H_3O^+ through the reaction

$$H_3O^+ + e^-_{aq} \longrightarrow H^\bullet + H_2O, \quad (2)$$

which reduces the lifetime of the hydrated electron to (40 ± 1) ps in strongly acidic solution [58]. Other electron scavengers such as N_2O [60] and IO_3^- [61] also reduce the lifetime of e_{aq}^-. Hydrated electrons are the primary reducing agent in LRL using femtosecond and picosecond pulses under both optical breakdown and LDP conditions [62-65], as will be further discussed in sect. 4.

Meanwhile, the water radical cation rapidly decomposes, on a timescale of (46 ± 10) fs as measured by X-ray transient absorption, by proton-transfer to a neutral water molecule [66]

$$H_2O^{\bullet+} + H_2O \longrightarrow OH^{\bullet} + H_3O^+ \tag{3}$$

producing a hydroxyl radical, $OH^{\bullet}$, and a hydronium cation, H_3O^+. Hydroxyl radicals primarily react through geminate recombination with hydrated electrons [67],

$$e_{aq}^- + OH^{\bullet} \longrightarrow OH^- \tag{4}$$

to produce OH^- on a timescale of (14.2 ± 0.4) ps [66]; although they will also undergo slower recombinations with one another, on a timescale of ~10 ns-10 μs [59],

$$2OH^{\bullet} \longrightarrow H_2O_2 \tag{5}$$

to form the stable product, H_2O_2. Hydrogen peroxide, H_2O_2, has been detected in numerous studies of ultrashort (i.e., femtosecond and picosecond) laser irradiation of water [63, 68-74], and drives LRL reactions like AuNP growth [63, 74-77].

Finally, a hydrated electron can also recombine with two water molecules within ~1 ns [78],

$$2e_{aq}^- + 2H_2O \longrightarrow H_2 + 2OH^- \tag{6}$$

to form hydroxyl anions and the stable product H_2.

In addition to ionization, laser interaction can generate highly exciting water molecules,

$$H_2O \xrightarrow{nh\nu} H_2O^* \tag{7}$$

that may undergo multiple reactions by colliding with neighboring water molecules [56]

$$H_2O^* + H_2O \longrightarrow H^{\bullet} + OH^{\bullet} + H_2O, \tag{8}$$

$$H_2O^* + H_2O \longrightarrow H_2 + O^{\bullet} + H_2O \tag{9}$$

producing both the stable product H_2, and reactive radicals. The $H^{\bullet}$ formed by eqs. (2) and (8) recombine to form additional H_2, and the $O^{\bullet}$ radicals formed in eq. (9) can similarly recombine to form O_2. The decomposition of laser-generated H_2O_2 has also been found to result in O_2 formation [69]. All three stable products (H_2, O_2, and H_2O_2), have been detected from femtosecond laser excitation of water [68, 69, 74, 79, 80], nanosecond laser irradiation of aqueous colloidal metal nanoparticle solutions [52, 81], and nanosecond-pulsed LAL of metal targets in water [82-84].

The reactions eq. (1) through eq. (9) and their timescales are summarized in Figure 2, along with the corresponding plasma and target lattice dynamics known from LAL with femtosecond, picosecond, and nanosecond laser-pulses [25]. It should be noted that plasma and lattice-dynamics will be the same whether they are induced by femtosecond or few-picosecond laser pulses, because these pulse durations are all shorter than the electron-lattice coupling time. Ablation with nanosecond pulses, in contrast, induces distinct dynamics because radiation is still present when the target disintegrates [25, 34-36]. For all pulse durations, reactive electrons and $OH^{\bullet}$ radicals, in addition to O_2 and H_2, are already present when the target lattice disintegrates ~1-10 ns after initiation of LAL. The products, O_2, H_2, and H_2O_2, have all been formed by the time the cavitation bubble develops ~1 μs after excitation. Hence, these species can all play an important role in nanoparticle formation within the cavitation bubble. In particular, the formation of reactive oxygen species (ROS), whether transient like $OH^{\bullet}$ or long-lived like H_2O_2, can induce nanoparticle oxidation. The effects of these reactions on LAL and LFL products will be discussed in sect. 3.

2.2 Reactions in organic solvents

Replacing water with organic solvents (such as alkanes, alcohols, ketones, or aromatics) as the laser-synthesis medium opens up a plethora of new options. Organic media both allows the production of carbon-based nanomaterials, and substantially alters the products of LAL and LFL. Although the reaction pathways induced by laser-decomposition of organic solvents are not as thoroughly characterized as are those for water (discussed in sect. 2.1) numerous transient and stable species known to contribute to nanomaterial formation are produced. This section will present the chemical reactions that bring about these species before reviewing the unique nanomaterials that may be formed by laser ablation of pure and mixed organic solvents.

2.2.1 Transient chemical species from organic solvent ablation

As with water, organic molecules (R) can be ionized by multiphoton absorption upon laser interaction

$$R \xrightarrow{nh\nu} e^- + R^{\bullet+} \tag{10}$$

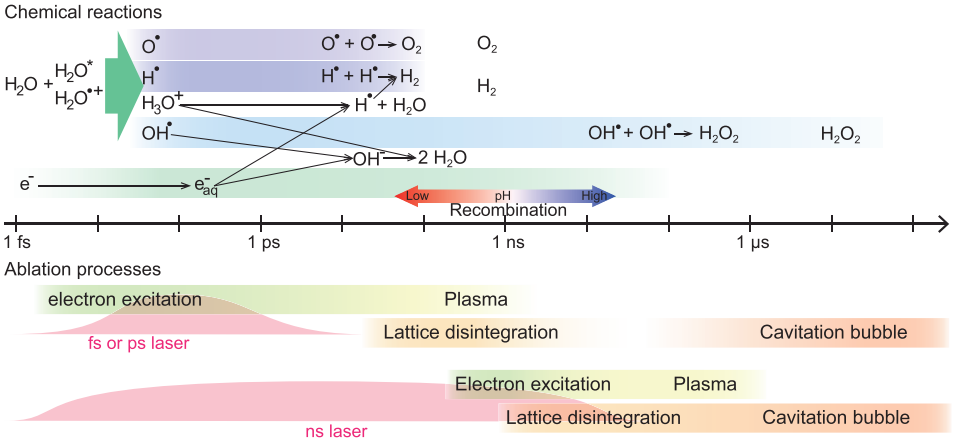

Figure 2 (Color online) Schematic illustration of the timescales of chemical reactions and ablation processes during LAL in water.

to produce a free electron and radical cation, $R^{\bullet+}$. Solvated electrons, with lifetimes of microseconds in organic media at temperatures below 100 K, have been observed in radiolysis experiments with flash-photolysis measurements [85]. Transient absorption measurements of octanes using 400 nm, 40 fs excitation pulses have observed the solvated-electron absorption feature centered around 1400 nm within ~100 fs of excitation [86-89]. This solvated electron signal decays on a timescale of about 400 fs because of geminate recombination [87]. Femtosecond flash-radiolysis measurements of room temperature alcohols indicate that electrons can become solvated on ~10 ps timescales and endure for 100 ps or longer. Their lifetimes increase as the number of carbon atoms in the alcohol increases [90]. The addition of electron scavengers like N_2O and CCl_4 reduces the lifetimes of solvated electrons from >2 ns to <100 ps in *n*-dodecane [91].

Unlike the rapidly decaying water radical cation, organic radical cations ($R^{\bullet+}$) can persist for nanoseconds or longer in room temperature solutions [91-94], although their lifetimes are substantially reduced in the presence of electron scavengers [91, 92]. However, these radical cations typically participate in several reactions before geminate recombination. For instance, cations generated from alkanes (RH_2) might undergo dehydration, dimerization, and hydrogen transfer [93-95],

$$RH_2^{\bullet+} \longrightarrow R^{\bullet+} + H_2, \tag{11}$$

$$RH_2^{\bullet+} + RH_2 \longrightarrow (2RH_2)^{\bullet+}, \tag{12}$$

$$RH_2^{\bullet+} + RH_2 \longrightarrow RH^\bullet + RH_3^+ \tag{13}$$

to produce various cationic species. Radical anions ($R^{\bullet-}$) can also form through electron attachment and undergo dissociation reactions [91, 96].

Neutral radical species can also form via multiphoton solvent excitation. For example, benzyl derivatives (Ph–CH_2–X) will undergo homolysis,

$$Ph{-}CH_2{-}X \xrightarrow{nh\nu} Ph{-}CH_2^\bullet + X^\bullet \tag{14}$$

to produce the stable benzyl radical, $Ph{-}CH_2^\bullet$ [97-99]. Yields of this benzyl radical from toluene excited at 248 nm are substantially enhanced when using nanosecond pulses, as compared to femtosecond pulses, as measured by the magnitude of the benzyl radical's transient absorption signal at 320 nm [99]. Increased yield is attributed to the population of the excited toluene triplet state, which is the precursor to benzyl radical formation [97]. Other neutral reactive species, like C_2 and $CH^\bullet$, have been observed from laser irradiation of pure aromatic solvents [99, 100]. Moreover, the observation of C_2 upon LAL of a carbon target in water using transient optical emission spectroscopy (OES) [101] has indicated that similar reactive species are produced during laser interaction with pure solvents and solid carbon targets.

2.2.2 *Stable reaction products*

Ablating solvents with a laser gives rise to the many reaction pathways discussed thus far, and these reactions ultimately culminate in stable molecular products. The resulting molecules can be identified through chromatography and mass spectrometry (Table 2). Small molecules, including H_2, CH_4, and C_2H_2, are produced in a wide array of solvents [102-104], as would be expected on the basis of the known transient intermediates discussed in sect. 2.2.1. The formation of polycyclic aromatic molecules from benzene [102, 105-107] can be attributed to dimerization of the initial benzene radical cations (eq. (12)) and related reactions. These products are formed using laser pulses with nanosecond through femtosecond durations. However an increased yield of these products was observed using picosecond pulses than nanosecond pulses, which has been attributed to the higher, ionization-enhancing electric fields obtainable

with picosecond pulses [102]. The incorporation of oxygen into some of these products has been ascribed to reactions between dissolved water and O_2 in benzene solution, which form $OH^{\bullet}$ [105, 106]. Additional oxidized products, including diols and quinones, are especially prevalent when a benzene-water bilayer is irradiated using a femtosecond pulse [105, 107], demonstrating the influence of ROS even when using organic solvents.

Irradiating pure solvents with femtosecond pulses yields not only small hydrocarbons and aromatics, but also linear chains of sp-hybridized carbons: polyynes (C_nH_2) [103, 108-112]. Polyynes have unique properties that are useful for optoelectronic applications, but they are difficult to produce via conventional synthesis methods [113]. Using femtosecond laser irradiation, polyynes up to $C_{14}H_2$ have been produced in octane and benzene media [108, 110, 111]; and $C_{18}H_2$ has been produced in toluene [112]. The formation of polyynes through femtosecond laser irradiation of liquid media is consistent with the observation of reactive intermediates such as C_2 and CH in the laser plasma [99, 100]. These detected intermediates likely coalesce into the observed linear carbon chains [103, 108-112]. Although hours of femtosecond irradiation are required to produce detectable quantities of polyynes, the creation of these synthetically challenging molecules directly from pure solvent is a testament to the power of laser ablation synthesis.

Beyond molecular products, the direct ablation of certain solvents produces various nanocarbon materials. Ablating pure benzene with femtosecond pulses yields amorphous carbon particles [111, 114], whereas both hydrophobic and hydrophilic oxidized carbon particles can be formed from a benzene-water bilayer [105, 107]. Carbon dots with <10 nm diameters have been produced from pure toluene ablation via unfocused, low-fluence nanosecond pulses [115, 116]. The ablation time significantly influences size and morphology of the carbon nanomaterial products produced by a Nd:YAG laser at 1064 nm: ablation for 5 min produced graphene sheets (Figure 3(a)-(c)), whereas ablation for 10 min produced a mixture of graphene sheets and <5 nm carbon dots (Figure 3(d)-(e) [115]. The authors attributed this result to a sequential mechanism wherein the excited toluene molecules coalesce to form graphene sheets, which are subsequently fragmented by the laser pulses (Figure 3(f)). Apart from pure carbon nanomaterials, femtosecond ablation has yielded carbon dots doped with nitrogen if in acetonitrile [117], with fluorine if in hexafluorobenzene [118], and with chlorine if in carbon tetrachloride [119]. Collectively, these diverse carbon products highlight how laser-induced reactions in organic media can produce unique carbon-based nanomaterials that are otherwise difficult to synthesize with conventional methods.

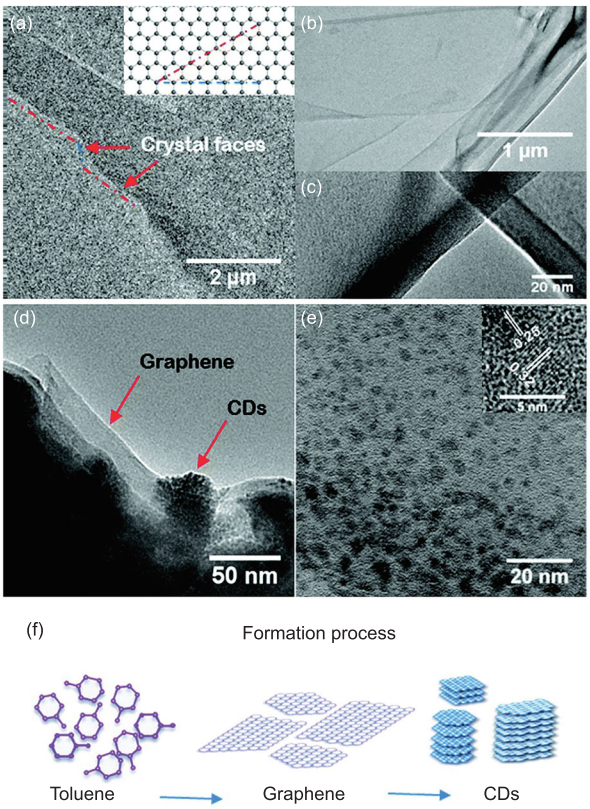

Figure 3 (Color online) TEM images of carbon products from toluene irradiated for 5 min (a)-(c) and 10 min (d)-(e). Inset of (a) shows zigzag and armchair edges of the crystal faces as indicated by blue and red lines. Inset of (e) shows the HRTEM image of the CDs. The proposed formation process is shown in panel (f). Reproduced from ref. [115] with permission from the Royal Society of Chemistry.

3 Properties of laser-synthesis products arising from chemical reactions

The solvent reactions discussed in sect. 2 have myriad effects on the physical properties of the nanomaterial products of LAL, LML, and LFL; dictating their compositions, sizes, phases, and so on. This section will highlight studies from the literature illustrating chemical reactions that result in oxidation, reduction, and incorporation of carbon into metal nanoparticles (MNPs). We will focus specifically on reactions whose outcomes are likely dependent on solvent molecules, and suggest potential future research endeavors. Thorough, tabulated summaries of nanoparticles obtained from LAL, LFL, and LML in various liquids are available in other reviews [30, 31].

3.1 Metal oxidation

Metal oxidation during LAL, due to water reactivity, has been known since the first LAL report by Ogale et al. [120] in

Table 2 Molecular products formed through laser ablation of pure solvents, under proceeding laser conditions. [102]: 1064 nm, 10 ns, and 20 ps; [106]: 800 nm, 30 fs; [105, 107]: 800 nm, 40 fs; [103, 110]: 800 nm, 90 fs; [108, 109]: 800 nm, 100 fs; [112]: 800 nm, 35 fs; [104]: 800 nm, 36 ps

Product	Alkanes	Benzene	Toluene	Acetone	Acetonitrile
H_2	[102]	[102]	[102]	–	[104]
CH_4	[102]	[102]	[102]	[103]	[104]
C_2H_2	[102, 108]	[102]	[102]	–	[104]b)
C_2H_4	[102, 108]	[102]	[102]	–	–
CO	–	–	–	[103]	–
C_2H_6	[102]	–	–	–	–
Toluene	–	[102]	–	–	–
Phenol	–	[105-107]	–	–	–
Phenylacetylene	–	[106]	–	–	–
Biphenyl	–	[102, 105-107]	–	–	–
Phenanthrene	–	[102]	–	–	–
Anthracene	–	[102]	–	–	–
C_nH_2a)	[108-110]	[111]	[112]	[103]	–

a) Polyynes with n in the range of n = 6-14. b) Not assigned in original reference.

1987. In this experiment, FeO nanoparticles were produced by LAL of iron metal in water. Since this early study, the production of various metal oxides from aqueous LAL and LFL of metals has been reported in hundreds of studies, and well-reviewed [27]. Metal-target oxidation occurs as ROS in the plasma and cavitation bubble (typically $OH^{\bullet}$, H_2O_2, $O_2^{\bullet -}$, and dissolved O_2) react with ablated metal atoms. The evidence for the contribution of dissolved O_2 to metal oxidation during LAL and LFL has been observed in studies on copper [121] and antimony sulfite [122]; these MNPs exhibited decreased oxidation when their water media was degassed before ablation. As degassing the media decreases oxidation, supplementing the liquid with additives can enhance oxidation; further controlling the properties of the products. For instance, adding NaCl increases both the surface charge density and the surface oxidation of gold nanoparticles (AuNPs) synthesized by LFL, which is credited to the *in situ* production of $Cl^{\bullet}$ radicals that bolster the oxidizing effects of ROS [123].

Although uncontrolled oxidation is usually undesirable in laser-synthesis, ablation in a strongly oxidizing H_2O_2 solution can substantially change nanoparticle composition. For example, LAL of a $Au_{73}Fe_{27}$ target produced AuNPs in pure water, as compared to $Au_{96}Fe_4$ nanoparticles with iron oxide shells when H_2O_2 is added [124]. Ablation in H_2O_2 solution also enables extensive control over nanoparticle size and morphology, as illustrated in Figure 4. LFL of AuNPs in NaOH and H_2O_2 produced gold clusters with a mean size of 2.1 nm, compared to 3.5 nm in NaOH alone (Figure 4(a), (b)) [125]. Whereas LAL of a copper target in pure water produced mixed Cu_2O and CuO cubes that precipitated within two weeks (Figure 4(c)), ablation in H_2O_2 solution produced colloidally stable $Cu(OH)_2$ needle-like structures, that converted into polycrystalline CuO needles upon drying (Figure 4(d)) [126].

Stable hydrogen and oxygen molecules, H_2 and O_2, have been directly detected during LAL of metal targets in water [82-84], and during laser-irradiation of aqueous solutions containing colloidal metal nanoparticles [52, 81]. Moreover, $OH^{\bullet}$ formation in irradiated MNP solutions has been indirectly detected using fluorescent radical scavengers [53], and $OH^{\bullet}$ has been directly detected with time-resolved OES during LAL of titanium in water [127]. These observations suggest that the water-decomposition reactions discussed in sect. 2.1 play an important role in determining the properties of LAL-synthesis products.

To better understand the conditions comprising oxidations of metal nanoparticles during LAL, namely water-decomposition and the reactions between ablated metals and water molecules, Kalus et al. [83] designed an experiment in which the production of H_2, O_2, and H_2O_2 could be quantified for seven metals with different redox potentials during LAL in water (Figure 5). The amount of H_2 produced increased much more dramatically when easily-oxidized metal targets like iron, titanium, and aluminum were used; as compared to targets like gold, platinum, silver, and copper (Figure 5(a)). An inverse correlation therefore emerged between H_2 yield and H_2/O_2 ratio with the standard reduction-potential of the metal (Figure 5(b), (c)).

The high yield of H_2 for metals with negative standard reduction-potentials ($E^0 < 0$ V) is attributable to these potentials lying below that of the H_2 formation potential ($2H^+ + 2e^- \longrightarrow H_2$, $E^0 = 0$ V). This relationship results in the direct oxidation of the bulk-metal target and ablated metal species by the surrounding water molecules, releasing H_2 [83]. Nevertheless, detectable quantities of H_2 and O_2 upon ablation

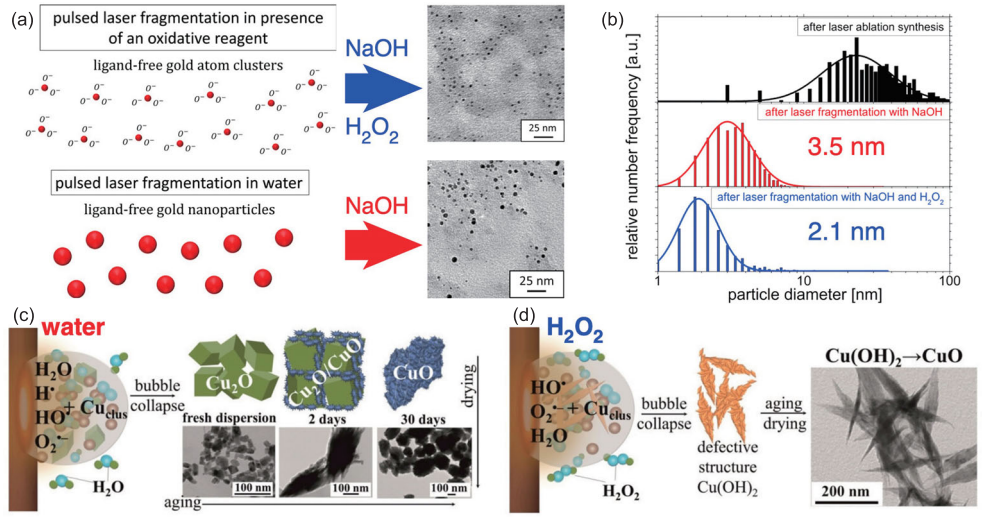

Figure 4 (Color online) Scheme of LFL in aqueous NaOH with (top, blue) and without (bottom, red) H_2O_2, with TEM images of resulting AuNPs (a) and size distributions of LFL AuNPs (b). Schematic illustration of reactive species from LAL of copper in water (c) and H_2O_2 (d) with resulting particle morphologies. Adapted from ref. [125] (a), (b), copyright 2016, with permission from Elsevier; and ref. [126] (c), (d), copyright 2019 American Chemical Society.

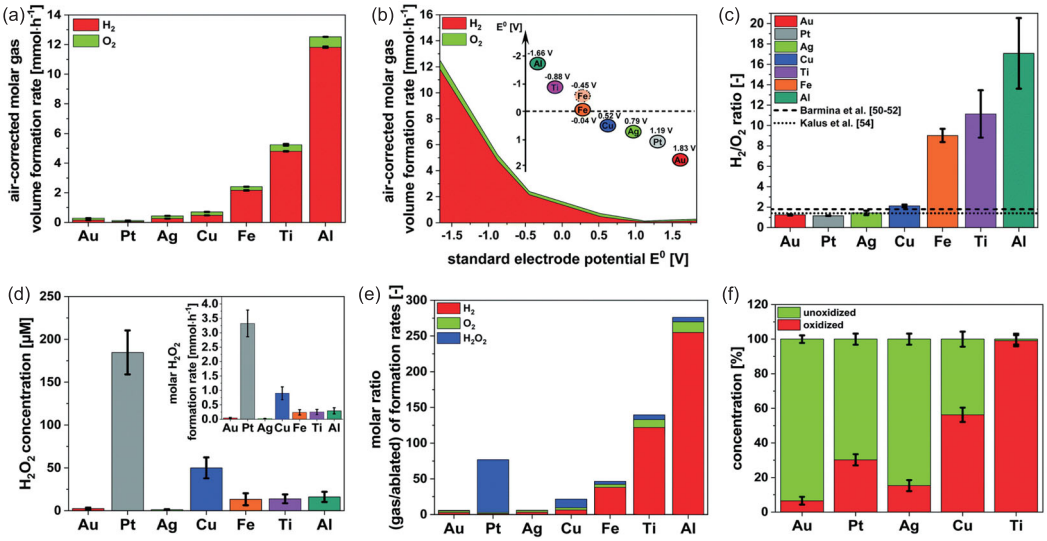

Figure 5 (Color online) Formation rate of H_2 and O_2 upon ablation of metal in water (a); the same data plotted as a function of metal redox-potential (b). Ratio of H_2/O_2 (c). H_2O_2 concentration after LAL (d). Total molar ratio of byproducts relative to ablated metal nanoparticles (e). Oxidation fraction of ablated metal nanoparticles, as measured by XPS (f). Adapted from ref. [83] with permission from the Royal Society of Chemistry.

of the noble metals gold and silver, with $E^0 > 0$ V, indicates that direct water-decomposition (according to the reactions in sect. 2.1) also occurs during ablation. Moreover, all seven tested metals produced H_2O_2 (Figure 5(d)) which indicates $OH^{\bullet}$ formation from water-decomposition. The anomalously high yield of H_2O_2 generated with platinum metal is a consequence of electrochemical oxygen-reduction by the platinum nanoparticles, which are catalytically active [83]. Overall, the molar ratio of total water byproducts to total ablated nanoparticles increases drastically for more easily oxidized metals (Figure 5(e)), which directly corresponds to the oxidized fractional composition of the ablated nanoparticles (Figure 5(f)). These results illustrate how the solvent-mediated redox reactions in LAL synthesis determine both the degree of nanoparticle product oxidation and the quantity of gaseous byproducts that are generated. High yields of gas byproducts in LAL will interrupt and slow nanoparticle synthesis, as microbubbles will impede the path of the laser [128]. Hence, understanding the chemical reactions that occur during LAL synthesis is important not only for better control of product composition, but also for optimizing reactor design to overcome the potentially detrimental effects of gaseous byproduct-formation.

Formerly, little was known about when metal oxidation

occurred; whether it was during the plasma phase, within the cavitation bubble, or after cavitation bubble collapse. The implementation of time-resolved spectroscopic measurements with resolution over the nano- through millisecond timescales has been critical to unraveling the dynamics of metal oxidation during LAL.

Time-resolved OES measurements have shown that transient aluminum atoms partially oxidize to AlO molecules [129,130] and titanium atoms oxidize to TiO molecules [131] within ~100 to 200 ns of ablation. These measurements indicate that some oxidation occurs during the plasma phase. Reich et al. [132] identified multiple timescales of zinc oxidation using time-resolved X-ray absorption fine structure spectroscopy (TR-XAFS) measurements of zinc metal ablated in water, using 1064 nm, 7 ns pulses (Figure 6). The TR-XAFS measurements obtained at three different time-delays (Figure 6(a)) show a high contribution of vapor-phase zinc atoms and $Zn(H_2O)_n$ clusters at a 12 μs delay, indicated by the magenta ‡. The remaining signal comes from zinc metal. Later, at a delay of 18 ms, the contribution of ZnO increases, represented by green ∗. The contributions of the reactive zinc species (zinc atoms in vapor phase and clusters) and ZnO, at different positions within the cavitation bubble, as a function of time-delay, are shown in Figure 6(b), (c). The reactive zinc species have high contributions at delays of <100 μs. Oxidized ZnO appears at delays of several milliseconds. The presence of a ~80%-90% metallic zinc, even at delays of ~30 ms, indicates that bulk oxidation of the ablated zinc metal is quite slow. This pace is consistent with a previous report, which states that quantitative oxidation of zinc colloids produced by LAL using nanosecond pulses in water occurs over the course of 10 min [133]. This slow bulk oxidation of initially formed ZnNPs must be driven by long-lived ROS such as H_2O_2 or dissolved O_2. In contrast, the low-energy XAFS peak assigned to vapor-phase zinc atoms gradually upshifts over ~100 μs, which the authors ascribe to the formation of $Zn(H_2O)_n$ or other clusters [132]. This result indicates that oxidation of vapor-phase zinc atoms takes place within the cavitation bubble or even earlier; consistent with earlier OES results [129-131]. Further time-resolved investigations of LAL with chemical-species detection are critical to advancing understanding of oxidation timescales for other metals or when using ultrashort laser pulses.

3.2 Metal reduction

Laser fragmentation and laser melting of metal-oxide powders in organic media are both popular methods for fully or partially reducing metal ions. For instance, plasmonic MNPs were created via LFL of CuO [134-136] and Ag_2O [137] powders in solvents like isopropyl alcohol and acetone. The metal ions were reduced using nanosecond pulses at wavelengths of either 1064 or 532 nm and ~1000 mJ cm^{-2} fluence. Moreover, LFL of CuO in isopropyl alcohol generated acetone as a byproduct, as detected by GC-MS [134]. Evidence that the alcohol medium was oxidized to acetone suggests that interaction with the laser plasma allowed it to chemically reduce CuO. In the low-fluence, LML regime (~50-200 mJ cm^{-2}), where no plasma is formed; powders like CuO [138, 139], NiO [140], Bi_2O_3 [141], Fe_3O_4 [142, 143], and Fe_2O_3 [144] can be partially or fully reduced in organic media like ethanol, acetone, and ethyl acetate. In the LML fluence regime, the degree of metal reduction increases proportionally with laser fluence [138-142, 144] and processing time [140, 143]. Suehara et al. [144] proposed that metal ion reduction was driven in part by thermal decomposition of the solvent. Computational modeling of ethanol decomposition indicated the presence of reducing species, including H_2, CH_4, and C_2H_4, all of which emerged within 100 ns of solvent heating to 3000 K. Their modeling also indicated that the reduction of Fe_3O_4 to FeO is thermodynamically favorable in the presence of C_2H_4 at temperatures above 800 K [144]. While these computational results provide intriguing potential insights into metal ion reduction mechanisms in LML, further studies exploring methods for the detection of solvent decomposition byproducts (for example, by GC-MS) in the LML regime are needed for a more complete understanding.

Although organic solvents are typically used when metal ion reduction is desired—as organic solvents tend to generate reducing species—metal ions in metal oxide powders can be partially reduced during LFL in water too, as illustrated by some examples in Figure 7. LFL of ZnO in water with 1064 or 532 nm nanosecond pulses reportedly introduces oxygen vacancies [145-147], indicating the partial reduction of Zn^{2+}. This partial reduction modifies both the color and luminescence of the LFL product, as shown in a photograph (Figure 7(a), left [145]) and in photoluminescence spectra (Figure 7(a), right [146]). LFL of CeO_2 powder in water with 1064 nm, 10 ns pulses substantially increased the Ce^{3+} content in the resultant ceria nanoparticles, from 7.5% up to 40% (Figure 7(b) [148]). Partial reduction of α-Fe_2O_3 powder to magnetic Fe_3O_4 nanoparticles was achieved in water by LFL with 532 nm, 6 ns pulses (Figure 7(c) [149]). LFL of anatase TiO_2 in water with 355 nm, 5 ns pulses reduced some Ti^{4+} ions to Ti^{3+}, and formed oxygen vacancies in the laser-generated black TiO_2 product (Figure 7(d) [150]). Similar results were obtained in a separate study [147].

The partial metal ion reduction observed in refs. [145-150] is most likely driven by the plasma electrons produced in LFL, as no other reducing species are generated during aqueous LAL. Direct observation of transient, reduced aluminum

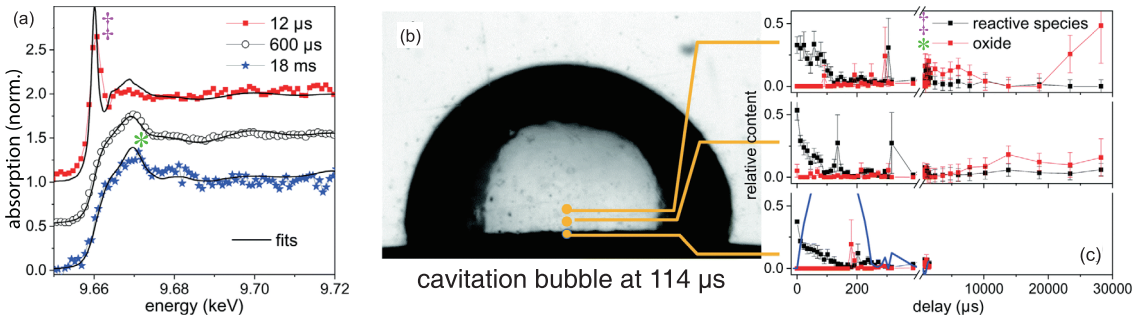

Figure 6 (Color online) TR-XAFS of ablated zinc recorded at different post-ablation time delays, with indicated peaks assigned to vapor-phase reactive zinc species (magenta ‡) and ZnO (green ∗) (a). Image of cavitation bubble at a delay of 114 μs, with indicated positions of TR-XAFS measurements (b). Relative contributions of reactive zinc species (black) and ZnO (red) as a function of time delay at each of the three indicated positions (c). Adapted from ref. [132], CC-BY-3.0.

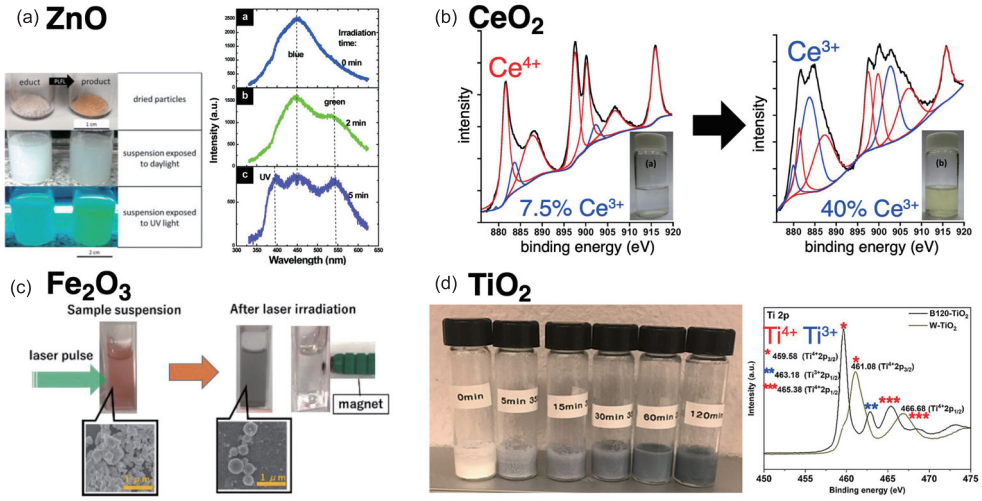

Figure 7 (Color online) Photographs (left) and photoluminescence spectra (right) of ZnO nanoparticles produced by LFL in water (a). XP spectra of ceria nanoparticles before (left) and after (right) LFL in water showing increased Ce^{3+} content (b). Photographs and SEM images of α-Fe_2O_3 powder before and after LFL showing conversion to Fe_3O_4 (c). Photographs (left) and XP spectra of TiO_2 powder before and after LFL, showing the generation of Ti^{3+} species (d). Adapted from ref. [145] (a), copyright 2015, with permission from Elsevier; ref. [146] (a), copyright 2011 American Chemical Society; ref. [148] (b), copyright 2014, with permission from Elsevier; ref. [149] (c), with permission from the Chemical Society of Japan, and ref. [150] (d), copyright 2019, with permission from Elsevier.

atoms supports this idea. Time-resolved OES taken during LAL of a Al_2O_3 target in water with 355 nm, 5 ns pulses indicates reduction via plasma electrons (Figure 8). Direct reduction of the Al^{3+} ions into neutral aluminum atoms was observed within 200 ns (Figure 8(a)), which is during the plasma phase [129]. Moreover, although partially oxidized AlO molecules are observed as early as 500 ns in Figure 8(a) [129], both the aluminum atoms and AlO molecules are present in the cavitation bubble over timescales as long as ~100 μs (Figure 8(b)) [130]. Subsequent computations with DFT and MP2 methods predicted the dynamics of aluminum atom oxidation to AlO, and the coalescence of initial hot aluminum, oxygen, and AlO species into larger clusters with Al_2O_3 composition as the temperature cooled from the initial plasma's ~4800 to 1500 K [151]. The computational results were consistent with the experimental production of <10 nm γ-Al_2O_3 nanoparticles [129]. These observations of long-lived aluminum atoms are compatible with the long-lived Zn metal species in ref. [132], further confirming the slow dynamics of bulk nanoparticle oxidation during LAL. Additional time-resolved measurements on other metal and oxide targets are needed before a more complete understanding of oxidation and reduction dynamics during LAL and LFL can be developed. Fuller understanding could enable greater control over the final nanoparticle compositions.

3.3 Incorporation of carbon into nanoparticles

Making MNPs encased in carbon shells, with metal carbide phases, or both, can be achieved by performing LAL or LFL on metal targets immersed in organic solvents, and in fact, this is a technique that has been in use for nearly two decades

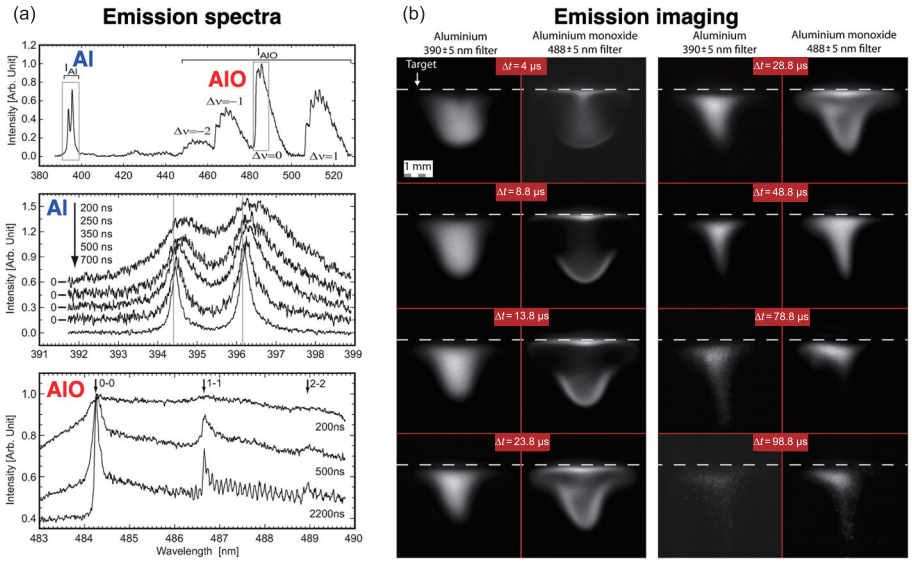

Figure 8 (Color online) OES of neutral aluminum atoms and AlO molecules at selected time-delays between 200 and 2200 ns (a) and images of the cavitation bubble showing aluminum and AlO species at delays between 4 and 100 µs (b). Adapted from ref. [129] (a), with permission from the Royal Society of Chemistry; and ref. [130] (b), copyright 2014, with permission from Elsevier.

[16-18, 20, 22]. The facile incorporation of carbon into MNP products is almost predictable considering the abundance of reactive radicals and stable molecules produced upon laser ablation of organic solvents previously discussed in sect. 2.2. Organic byproducts, including CO, CH_4, C_2H_2, C_2H_4, C_2H_6, C_3H_4, C_3H_6, C_3H_8, and C_4H_{10}; have been observed during LAL of a gold target in ethylene glycol [82]. Moreover, LFL of AuNPs in diethyl ether and various alcohols produces numerous volatile byproducts, including methanol, acetone, acetates, and aldehydes [52]. The presence of these species within the cavitation bubble during MNP growth allows for carbon species to be incorporated rapidly into the nanoparticles in the form of graphitic or amorphous carbon shells, or for certain metals, metal carbide phases.

Graphitic and amorphous carbon shells have been reported for MNPs produced through both LAL and LFL. These shells can form around many metals. Examples in the literature include gold [152-154], copper [121, 154], titanium [154-156], iron [154, 157-159], nickel [154, 160, 161], chromium [154, 162], tungsten [154, 163], molybdenum [154, 163-165], tantalum [163, 164], cobalt [166], hafnium [164], niobium [164], silver [167], and aluminum [168]; as well as the semiconductor silicon [152, 165, 169-172], and various metal alloys [121, 173, 174]. Regardless of the metal target, the structure of the carbon shell is determined by the solvent used and by the laser's pulse-duration. The highest degree of shell graphitization is consistently observed in toluene [153, 156-158, 162, 163]. Short pulses (of nanosecond duration) also form graphitic shells upon ablation of chloroform [152, 171], hexane [153, 160, 161], and acetone [121, 154, 163, 168]. Amorphous carbon shells have been reported to form in alcohols [153, 165]. Interestingly, nanosecond ablation of acetonitrile introduced nitrogen-doping to the graphitic carbon shell [161]. In contrast, ultrashort pulses of picosecond or femtosecond duration produce few-layer graphene shells in alcohols and acetone [158, 159, 173, 174].

Figure 9 highlights features of carbon shells and MNP phases obtained using nanosecond, picosecond, and femtosecond pulses in toluene, acetone, and ethanol for LAL of iron (Figure 9(a)-(c), (g)-(i)) and $Fe_{80}Ni_{20}$ alloy (Figure 9(d)-(f)) [154, 157, 158, 173]. The thickest carbon shells are clearly visible when toluene is the solvent, regardless of pulse duration (Figure 9(a), (d), (g)). Thinner shells are obtained in acetone (Figure 9(b), (e), (h)). This correlation between carbon shell thickness and relative carbon content of the solvent molecule, i.e., seven carbon atoms in toluene compared with three carbon atoms in acetone, indicates that the availability of carbon reactive-species in the plasma and cavitation bubble or both determines the shell thickness, independent of pulse duration. Meanwhile, thinner carbon shells are obtained using ultrashort pulses (Figure 9(d), (e), (g), (h)) relative to nanosecond pulses (Figure 9(a), (b)) in toluene and acetone. This result has been attributed to the faster cooling rate associated with shorter pulse durations, which arrests the growth of the carbon shells [158, 173], although ultrashort pulses can also form carbon byproducts [167, 170, 172, 175], as discussed further below. Ethanol makes for a particularly interesting case for LAL of iron: ref. [157] observed no carbon shell with nanosecond pulse durations (Figure 9(c)), but thin carbon shells are formed with pulses of picosecond (Fig-

ure 9(f)) and femtosecond (Figure 9(h)) durations, observed in refs. [173] and [158], respectively. This result indicates that ultrashort pulses more readily produce the reactive carbon species discussed in sect. 2.2, which suggests that the reported higher degree of solvent ionization for pico- as compared to nanosecond pulses [102] plays an important role in carbon shell formation.

In addition to the pulse duration and media, the target metal and ablation time both influence the carbon-shell structure and thickness. For instance, the facile growth of carbon shells from LAL of copper in acetone was attributed to copper's ability to catalyze C–C bond formation and graphene growth [121, 154]. Sufficiently long ablation times allow networks of carbon-encapsulated MNPs to form and amorphous carbon shells to graphitize around MNPs (Figure 10) [154]. Some carbon shells contain graphitic carbon "onions" surrounding an amorphous carbon layer (Figure 10(d)). This type of structure is credited to the re-irradiation of MNPs by subsequent laser pulses during the 30 min ablation period. The outer layers are most directly exposed to heating from the nanosecond laser and reach high temperatures sufficient for graphitization, as illustrated in Figure 10(g) [154]. Hence, longer ablation times are expected to result in a greater degree of graphitization regardless of the organic medium. It should be noted that in Figure 9 that the ablation time in ref. [154] (Figure 9(b)) was 30 min; in ref. [173] (Figure 9(d)-(f)) it was 20 min; and ablation time was not reported in the remaining references. The absence of any carbon shells on FeNPs synthesized with nanosecond lasers in ethanol in ref. [157] may be due to a shorter ablation time, because amorphous carbon coatings on FeNPs obtained in ethanol with nanosecond lasers have been observed in a different study [176].

The surface carbon-structures that form on SiNPs during LAL and LFL are influenced by the pulse duration and fluence of the laser, and the nature of the solvent media. For nanosecond pulses in toluene [152, 165, 177] and $CHCl_3$ [152, 171], graphitic carbon coatings will form with the use of high laser-fluence ($\geq$3 J cm^{-2}), but low laser-fluence ($\leq$0.8 J cm^{-2}) will just produce SiNPs that are surface-passivated with solvent molecules (1-octene, 1-octyne, dichloroethylene) [178-180]. Femtosecond pulses also produce surface-passivated SiNPs without carbon coatings when low laser-fluence is used [181-183]. Passivation of silicon surfaces with solvent molecules has been linked to a facile reaction between bare silicon atoms and unsaturated carbon-carbon double bonds in the solvent [178, 182]. It is a reaction that does not require solvent decomposition, and its mechanism is congruent with the preferential formation of passivated SiNPs under low laser-fluence conditions, wherein significant solvent decomposition is unlikely. Femtosecond-pulsed LAL with laser fluence in excess of 1 J cm^{-2}, on the other hand, forms networks of carbon-encapsulated SiNPs, caused by extensive chemical decomposition of the liquid and carbon-byproduct formation [169, 172].

Carbon-byproduct formation during SiNP synthesis with ultrashort pulses also affects the observed luminescence of the products. An extensive carbon matrix forms when silicon

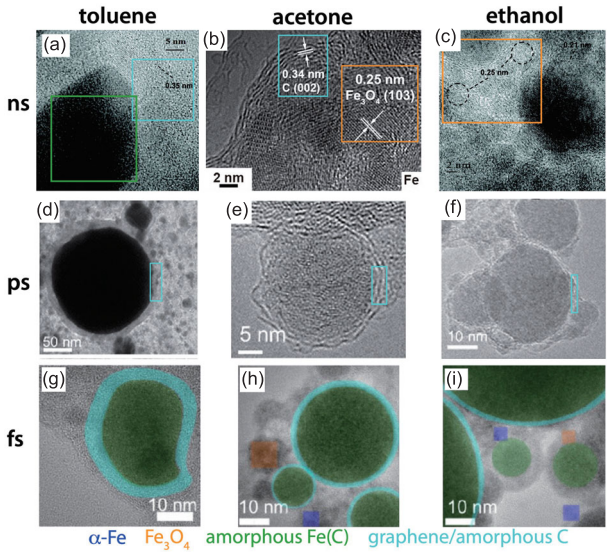

Figure 9 (Color online) High resolution TEM images of nanoparticles obtained from ablation of iron in toluene, acetone, and ethanol with nanosecond pulses (a)-(c); $Ni_{80}Fe_{20}$ with picosecond pulses (d)-(f); iron with femtosecond pulses (g)-(i) with iron and carbon components labeled by color according to the legend in the figure. Adapted from ref. [157] (a), (c), copyright 2011 American Chemical Society; ref. [154] (b), copyright 2019 American Chemical Society; ref. [173] (d)-(f), copyright 2019, with permission from Elsevier; and ref. [158] (g)-(i), copyright 2017 Wiley-VCH.

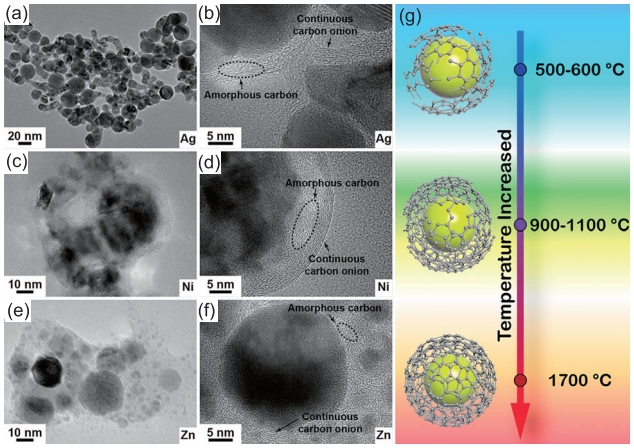

Figure 10 (Color online) TEM and high resolution TEM images of networks of encapsulated silver (a), (b), Ni-Ni_3C (c), (d), and Zn-ZnO (e), (f). Panel (g) shows a schematic illustration of carbon graphitization with increasing temperature. Reproduced from ref. [154], copyright 2019 American Chemical Society.

is ablated with 355 nm, 60 ps pulses in toluene (Figure 11(a)) [170], whereas 800 nm, 35 fs pulses that were stretched to 36 ps duration to ablate a 1-octene solution produced surface passivated SiNPs (Figure 11(b)) [175]. Both studies reported additional carbon byproducts from solvent decomposition, even in the absence of the silicon target, that exhibited blue photoluminescence, which is usually associated with passivated SiNPs [170, 175]. Intartaglia et al. [170] found that ablation of both pure toluene and a silicon target immersed in toluene produced identical photoluminescence spectra (Figure 11(a)), suggesting that the blue photoluminescence attributed to SiNPs was actually due to the carbon byproducts. A subsequent investigation by Dewan et al. [175] found that picosecond-ablated SiNPs in 1-octene exhibited the same photoluminescence features as irradiated isolated 1-octene (Figure 11(b), left). Ensuing separation of the SiNPs from the carbon byproduct by centrifugation showed that the SiNPs themselves produced photoluminescence primarily in the UV range (Figure 11(b), right). Carbon byproducts such as fullerenes have also been reported from ablation of silicon in toluene and $CHCl_3$ using high-fluence nanosecond pulses [165, 171, 177]. Further studies are needed to determine the extent to which carbon byproducts are generated through solvent decomposition other possible ablation conditions. However, the clear influence of these carbon byproducts on the SiNP photoluminescence spectra demonstrates the importance of monitoring these processes *in situ*, as these species have the potential to produce unwanted byproducts during LAL synthesis in organic solvents.

Beyond simple deposition of carbon onto the surfaces of MNPs, LAL in organic solvents can generate nanoparticles with metal carbide phases, including: SiC [165, 169, 171, 177, 184]; crystalline Fe_3C and amorphous Fe-C [157, 158, 185, 186]; TiC [154-156, 187]; Co_3C [166]; W_2C and WC [154, 165]; Cr_7C_3, Cr_3C_2, and Cr_3C_{2-x} [154, 162]; HfC [164, 188]; MoC and Mo_2C [154, 164, 189-191]; TaC and Ta_4C_3 [163, 164, 191]; NbC [154, 164]; Ni_3C [154]; ZrC [154]; VC [154]; and GdC_2 [192]. Metal carbide phases can also be deposited onto the surface of solid metal targets, as has been seen using titanium [193], tantalum [194], and tungsten metal in organic solution [194]. Although pure metal-carbide phases have been reported for some metals in certain solvents [154, 156, 162-164, 166, 190], mixtures of metal carbide with metal, or metal oxide phases, are more commonly obtained. For example, studies on the ablation of iron consistently report mixtures of Fe_3C with iron metal, various iron oxides, or both [157, 158, 185, 186].

The solvent can determine whether metal oxide phases form in conjunction with carbides, as in the case of chromium and titanium ablated with femtosecond pulses (Figure 12). Ablation of chromium in ethanol produced Cr_3O_4 nanoparticles along with Cr_7C_3 and Cr_3C_{2-x} carbides (Figure 12(a), top), but ablation in acetone or toluene produced only Cr_3C_{2-x} (Figure 12(a), middle-bottom) [162]. Ablating titanium in acetone produced some TiO_2 phase and TiC, both for nanoparticles (Figure 12(b)) [156] and the ablated titanium surface (Figure 12(c)) [193], but ablation in toluene or another hydrocarbon solvent produced only TiC.

In general, ablation in toluene and other hydrocarbons, as compared to solvents containing oxygen, is more favorable to the formation of pure metal carbide phases. This trend is apparently independent of pulse duration [156, 162, 163, 188, 193], although ablation in acetone with nanosecond pulses can also produce pure metal carbide phases [154, 163, 164, 166]. The removal of dissolved O_2 from the solvent and subsequent ablation under a N_2 atmosphere can also prevent metal-oxide formation [189]. Collectively, these studies illustrate the importance of oxygen removal, an unsurprising result considering the gratuitous production of ROS during ablation, even from trace quantities of dissolved O_2, and their consequent ability to oxidize metals [121]. Strategies for oxygen removal should inform future work on improving the purity of metal carbide phases during nanoparticle production via LAL and LFL. Moreover, the characters of the carbon shells formed on metal carbide nanoparticles are likely controllable through shrewd choice of solvent and

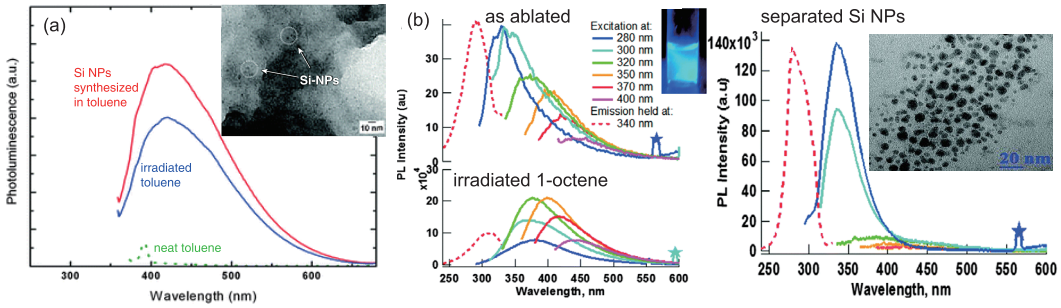

Figure 11 (Color online) Photoluminescence spectra with inset TEM images of SiNPs formed using picosecond pulses in toluene (a) and 1-octene (b) showing contributions from carbon byproducts. Adapted from ref. [170] (a), with permission from the Royal Society of Chemistry; and ref. [175] (b), with permission from the Royal Society of Chemistry.

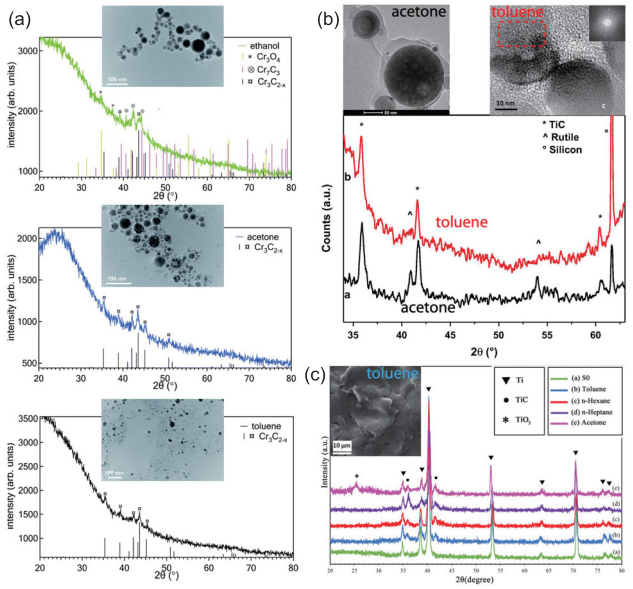

Figure 12 (Color online) XRD and TEM images of nanoparticles obtained from femtosecond ablation of chromium in ethanol (top), acetone (middle), and toluene (bottom) (a). XRD and TEM images of nanoparticles obtained from femtosecond ablation of titanium in acetone (black) and toluene (red) (b). XRD and SEM image of titanium surface from femtosecond ablation in various solvents (c). Adapted from ref. [162] (a), with permission from the Royal Society of Chemistry; ref. [156] (b) copyright 2017, with permission from Elsevier; and ref. [193] (c) copyright 2019, with permission from Elsevier.

pulse-duration, as suggested in Figure 9, along with consideration of carbon solubility in the target metal based on the phase diagram [154]. Further studies are required: it would be worthwhile to explore the effects of different pulse durations and solvents while monitoring the formation of carbon byproducts (cf. Figure 11) in addition to the product nanoparticle phases and carbon shell structures. Such examinations would shed light on the specific chemical mechanisms at work.

4 Laser reduction of metal precursors in liquid

Laser irradiation of solutions containing one or more metal precursors in the absence of a solid or colloidal target is referred to as LRL. This technique was developed in parallel to LAL as a route to surfactant-free metal nanoparticles. Where LAL and LFL use solid targets, in LRL the molecular precursors in solution and the solution itself are both the targets. As described in sect. 2, laser-induced decomposition of the liquid produces solvated electrons, hydrogen radicals, hydroxyl radicals, and many other reactive species depending on the liquid medium. The reactions of these species with metal precursors yield MNPs whose properties are highly dependent on both the laser's parameters and the composition of the target liquid. Because LRL has received limited attention in reviews on laser-synthesis, this section will systematically review LRL literature spanning nearly two decades and describe the current state of knowledge regarding the chemical reactions that lead to MNP formation. This section is divided into subsections focusing on noble metals (sect. 4.1), base metals (sect. 4.2), and alloys (sect. 4.3).

4.1 Noble metal nanoparticles

The majority of LRL studies focusing on noble-MNP synthesis use ultrashort pulses to process aqueous solutions and metal precursors. Femtosecond pulse durations are substantially shorter than the electronic-nuclear coupling timescales of the molecules in the liquid. Because of this timescale difference, the slow heat-transfer processes contribute energy only minimally. The major energetic contributor is the high concentrations of radical species generated in the plasma. High concentrations of both immediately-formed, fleeting free electrons (10^{18}-10^{22} cm^{-1}) [49], and longer-lived hydrated electrons (up to 0.1 M) [58], reduce metal ions; even in air-saturated solutions where O_2 acts as a scavenger [195]. The redox potentials of a solvated electron and a hydrogen radical, at −2.77 V_{SHE} and −2.10 V_{SHE}, respectively, are high enough to reduce most metal ions in aqueous solution [196]. Nakashima et al. [65] reported that about half of the solvated electrons produced in femtosecond-laser LDP contribute to the reduction of Eu^{3+} to Eu^{2+}, demonstrating the efficiency with which solvated electrons reduce metal ions. The formation of neutral metal atoms upon metal ion reduction results in nucleation, and subsequently, MNP growth. This section discusses LRL synthesis of Au- (sect. 4.1.1), Ag- (sect. 4.1.2), Pd- (sect. 4.1.3), and Pt- (sect. 4.1.4) NPs. Finally, noble-MNPs LRL synthesis will be summarized in sect. 4.1.5.

4.1.1 Gold nanoparticles

Synthesis of AuNPs has been the primary focus of LRL ever since the first femtosecond-LRL studies reported by Zhao et al. [197] and the Sato group [80]. The popularity of AuNPs is due to the inert nature of gold salts in aqueous solution, as well as their high reduction potentials. Since these original experiments, dozens of studies examining AuNP synthesis by LRL have been published [62-64, 70, 71, 74-77, 198-208].

The photochemical conversion of Au^{3+} ions to AuNPs follows a general reaction mechanism, which has been derived from radiolysis and UV irradiation experiments [209-212].

The process follows multiple steps,

$$Au^{3+} \xrightarrow{R^*} Au^{2+}, \tag{15}$$

$$Au^{2+} + Au^{2+} \longrightarrow Au^{3+} + Au^{1+}, \tag{16}$$

$$Au^{1+} \xrightarrow{R^*} Au^{0}, \tag{17}$$

$$nAu^{0} \longrightarrow Au_n. \tag{18}$$

Initially, Au^{3+} reacts with a reducing agent R^* to form Au^{2+} (eq. (15)). Unstable Au^{2+} quickly disproportionates to form Au^{+} and Au^{3+} (eq. (16)), after which Au^{+} is reduced to Au^{0} (eq. (17)). The Au^{0} atoms coalesce to form nuclei and grow from there into AuNPs (eq. (18)). Under high-intensity laser irradiation, there are two main mechanisms that can explain the reduction of aqueous $[AuCl_4]^-$ precursor. The first is direct homolysis of the Au-Cl bond by multiphoton absorption to form Au^{2+} and Au^{+} intermediates. The second is the chemical reduction of Au^{3+} ions by the hydrated electrons produced by water photolysis. Because the concentration of water molecules (55 M) far surpasses that of $[AuCl_4]^-$ molecules (~10^{-4}-10^{-3} M) in solution, hydrated electrons are assigned as the primary reducing agent in most LRL studies [62-64, 70, 74, 77, 202, 205]. However, observations so far cannot entirely rule out the contribution of direct, laser-induced homolysis of the Au-Cl bond. In one example, the formation of AuNPs from $[AuCl_4]^-$ irradiation with low-fluence, 532 nm, 8 ns pulses [71] was attributed to a small fraction of the $[AuCl_4]^-$ dissociating because of laser-induced heating, according to the mechanism in eq. (15) through eq. (18). Nevertheless, even in those experiments, the subsequent growth of the AuNPs did not proceed unless the light source wavelength was resonant with the AuNPs' surface plasmon resonance (SPR) peak, centered at $\lambda \sim 520$ nm [71].

The conversion of tetrachloroaurate salts ($HAuCl_4$ or $KAuCl_4$) into AuNPs during laser irradiation can be easily followed using a simple *in situ* UV-vis spectroscopy setup [63, 202]. Figure 13(a) shows representative UV-vis spectra tracing the conversion of $[AuCl_4]^-$ to AuNPs with 30 fs pulses [63]. Using these spectra, the growth of the AuNPs can be monitored, and completion of the reaction can be determined by when the growth of the SPR absorbance peak ceases. Figure 13(b), (c) illustrate this concept with SPR absorbance versus irradiation time plots.

The *in situ* monitoring of laser-induced $[AuCl_4]^-$ conversion to AuNPs has revealed the process's reaction kinetics. Multiple studies [63, 64, 71, 77, 205] have found that the AuNP growth kinetics in LRL follow the Finke-Watzky nucleation autocatalytic-growth rate law [213]; governed by a first-order nucleation rate constant (k_1), and a second-order autocatalytic growth rate (k_2),

$$-\frac{d[A]}{dt} = \frac{d[B]}{dt} = k_1[A] + k_2[A][B], \tag{19}$$

where [A] is the $[AuCl_4]^-$ concentration and [B] is the AuNP concentration. Integration of eq. (19) lets us model AuNP growth kinetics as a function of irradiation time, t, and the initial concentration of $[AuCl_4]^-$, [A(0)] [213]

$$[B(t)] = 1 - \frac{\frac{k_1}{k_2} + [A(0)]}{1 + \frac{k_1}{k_2[A(0)]} e^{(k_1 + k_2[A(0)])t}}. \tag{20}$$

Under certain experimental conditions, where the $[AuCl_4]^-$ reduction rate is slow, and AuNPs grow larger than ~10 nm, the Finke-Watzky model also imparts a time-dependent expression for the size of the growing nanoparticles [64, 71, 205].

$$[D(t)] = D_f \times \left(1 - \frac{\frac{k_1}{k_2} + [A(0)]}{1 + \frac{k_1}{k_2[A(0)]} e^{(k_1 + k_2[A(0)])t}}\right)^{\frac{1}{3}}, \tag{21}$$

where D_f denotes the final AuNP diameter. It should be noted that the kinetics of AuNP formation under acidic conditions had previously been fitted to eq. (20), with an added linear term [77]. However, those kinetics may be more accurately modeled by eq. (21), on account of the slow nucleation rate and the growth of larger (>20 nm) AuNPs.

Further insight into the roles of reactive species in the photochemical conversion of $[AuCl_4]^-$ to AuNPs was obtained by examining the dependence of the nucleation (k_1) and autocatalytic growth (k_2) rates on the peak laser-intensity [63, 71] and solution pH [77]. Meader et al. [63] extracted k_1 and k_2 in eq. (20) from UV-vis spectroscopy measurements conducted at a series of femtosecond laser pulse energies and durations (10-2400 μJ, 30-1500 fs) in a tight-focusing geometry, and observed that the value of k_1 exhibits a substantially stronger dependence on pulse energy, $k_1 \sim E^{1.6}$, than $k_2 \sim E^{0.6}$ (Figure 14(a)). Comparing nucleation rate-scaling to the computed scaling of optical breakdown plasma volume (i.e., the volume in which the calculated free-electron density exceeds the threshold density of 1.8×10^{20} cm^{-3}) found that both grow with laser intensity I as $\sim I^{3/2}$. The comparison therefore draws a linear correlation between the plasma volume and k_1 (Figure 14(b)). Autocatalytic growth rate values can be correlated with measured H_2O_2 formation-rates (Figure 14(c)) over a range of tight-focusing conditions and in LDP [50, 63, 71], with the same correlation $k_2 \sim [H_2O_2]^{0.6}$.

The results in Figure 14 demonstrate that the nucleation rate k_1 depends on the quantity of hydrated electrons generated in the laser plasma [63, 64, 71, 77, 205], which reduce $[AuCl_4]^-$ according to the reaction

$$[AuCl_4]^- + 3e^-_{aq} \longrightarrow Au(0) + 4Cl^-. \tag{22}$$

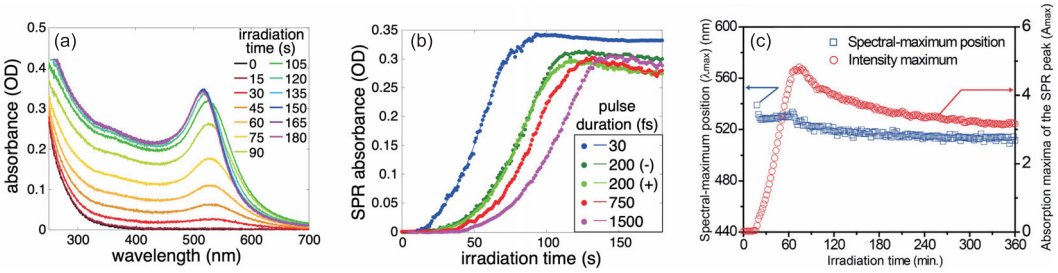

Figure 13 (Color online) UV-vis spectra recorded during irradiation of aqueous $[AuCl_4]^-$ using 2400 μJ pulses with 30 fs durations (a); time-dependent absorbance of the SPR feature upon irradiation with pulses of varying durations (b); peak wavelength (λ_{max}) and absorption maxima (A_{max}) in the spectra collected during laser irradiation (c). Adapted from ref. [63] (a), (b) copyright 2017, American Chemical Society; and ref. [202] (c), CC-BY 3.0.

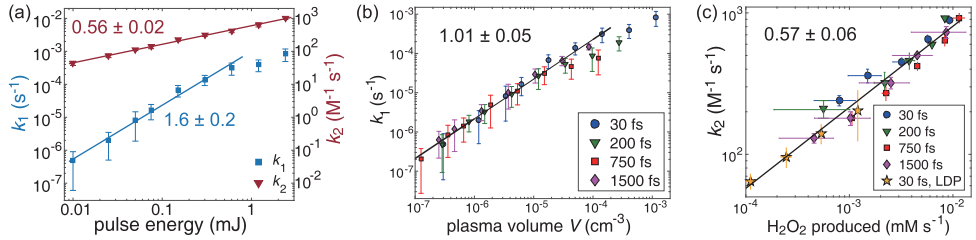

Figure 14 (Color online) Rate constants for 30 fs laser pulses (blue, k_1; red, k_2) as a function of pulse energy for tight-focusing geometry (a). Correlation between k_1 and calculated optical breakdown plasma volume for tight-focusing geometry (b). Correlation between k_2 and H_2O_2 production for tight-focusing geometry for different pulse energies and LDP geometry (c). Adapted from ref. [50] CC-BY-3.0.

The autocatalytic rate constant k_2 depends on the rate of H_2O_2 formation [63, 77], governed by the reaction [214]

$$[AuCl_4]^- + \frac{3}{2}H_2O_2 + Au_m \longrightarrow Au_{m+1} + \frac{3}{2}O_2 + 3HCl + Cl^-. \quad (23)$$

The autocatalytic reduction of gold with respect to AuNP growth by H_2O_2 can occur even after the laser has been turned off [74-76, 208].

Variation in laser parameters (focusing conditions, pulse duration, pulse energy, irradiation time) and chemical parameters (precursor concentration, solvent composition, the presence or absence of capping agents, solution pH) make it possible to control the size, shape, and stability of AuNPs synthesized by LRL [62-64, 70, 71, 74-77, 80, 198-202, 205-207]. In many cases, this control can be understood in terms of the effects these parameters have on k_1 and k_2, based on the photoreduction processes outlined in eqs. (22) and (23).

Multiple studies found that in aqueous media, higher laser pulse energy produces smaller AuNPs [63, 70, 71, 203, 205], although the opposite trend was observed in alcohol media [207]. As the laser pulse energy increases, the formation of smaller AuNPs suggests that a greater quantity of nuclei are formed relative to the fixed amount of $[AuCl_4]^-$ precursor in the solution [63, 70, 71, 205]. Increased availability of hydrated electrons, as is associated with high pulse energies, would accelerate $[AuCl_4]^-$ reduction according to eq. (22) and amplify nucleation. It should be noted that this trend of size-dependence on laser pulse energy is the opposite of what was observed in LAL of solid gold targets. In LAL, higher pulse energies typically favored the formation of larger nanoparticles [215-217].

Laser focusing-geometry substantially influences the nonlinear interactions between the laser beam and the media, as explored in sect. 2.1. Many studies opt for a tightly-focused geometry [63, 70, 74, 77, 80, 197, 200], which yields electron densities in the focal point that well exceed the optical breakdown threshold, and can reach up to $\sim 10^{22}$ cm^{-3} [63]. In contrast, use of loose-focusing or a collimated, unfocused beam yields an LDP environment. Electron densities of LDPs are on the order of $\sim 10^{-18}$ cm $^{-3}$ due to the extensive supercontinuum emission, which turns an 800 nm laser beam into a white-light filament [54]. LDP conditions seem well-suited for controlling the sizes of AuNPs through $[AuCl_4]^-$ reduction: autocatalytic growth (eq. (23)) would be limited because of low H_2O_2 production [64, 71, 218]. However, LDP conditions also limit e^-_{aq} production, which lowers the nucleation rate and forces AuNPs to stabilize through aggregative growth and agglomeration. Hence, tight-focusing typically results in significantly smaller AuNPs as compared to loose-focusing, for the same pulse energy and duration. The trend can be observed by comparing the TEM images and size distributions in Figure 15(a), (b) [63, 71].

Focusing conditions that use geometries with low numerical apertures still produce supercontinuum emission through self-focusing and filamentation, which can cause intensity

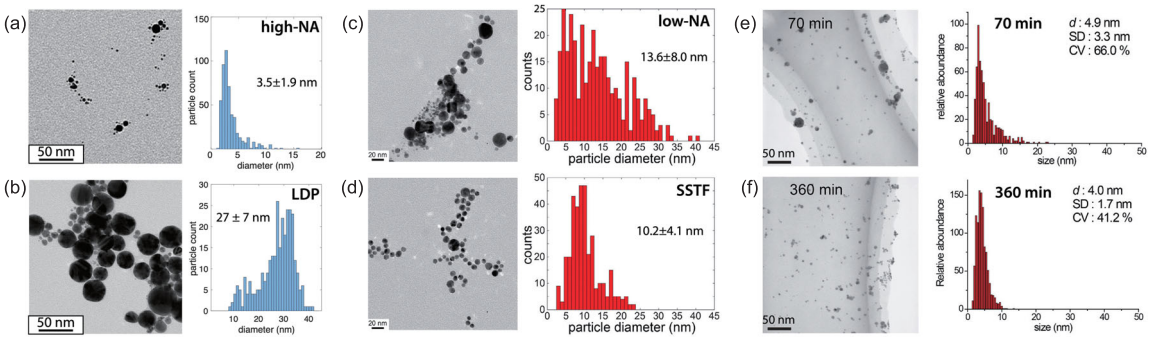

Figure 15 (Color online) Representative TEM images and AuNP size distributions synthesized with under the following conditions: (a) tightly focused high NA, 2.4 mJ, 30 fs; (b) loose focus LDP, 2.7 mJ, 30 fs; (c) tightly focused low NA, 35 fs; and (d) SSTF, 36 ps. Panels (e) and (f) show AuNPs prepared with different laser irradiation times. Adapted from ref. [63] (a), copyright 2017 American Chemical Society; ref. [71] (b), with permission from Royal Society of Chemistry; ref. [70] (c), (d), copyright 2014 American Chemical Society; ref. [202] (e), (f), CC-BY 3.0.

clamping [219]. The resulting reduction of the laser-intensity maxima decreases the number of reactive species formed. Both tight-focusing (by use of geometries with high numerical apertures), and simultaneous spatial and temporal focusing (SSTF), by which the frequency components of the laser pulse are spatially separated before focusing [220], can avoid excessive filamentation and therefore, intensity clamping. Moreover, loose-focusing geometries (using low numerical apertures) result in the formation of low kinetic-energy bubbles along the length of the focal region. These slow-circulating bubbles that cluster around the reaction locus both interfere with the focusing dynamics of subsequent laser pulses, and prevent the effective circulation of the solution [70]. In contrast, high numerical aperture geometry and SSTF result in an extensive optical breakdown, producing cavitation bubbles with high kinetic energy. These energetic bubbles disperse the Au(0) nuclei formed in the plasma out into the less turbulent regions of the solution, where the AuNPs can grow. Circulation generated in this manner eliminates the need for magnetic stir-bars [17,70,80,198,200,203]. As a result, loose-focusing options (Figure 15(c)) produce larger and more polydisperse AuNPs than tightly-focused geometries (Figure 15(a)) or SSTF (Figure 15(d)) [63,70].

Fragmentation of already-formed AuNPs, fabricated initially by LRL of aqueous $[AuCl_4]^-$, is commonly observed [70,71,80,202,204,207,208]. Irradiating pre-made AuNPs with tightly-focused 800 nm, 5.6 mJ, 100 fs pulses for 70 min (Figure 15(e)) results in larger AuNPs than are produced when the same starting material is irradiated for 360 min (Figure 15(f)) [202]. This fragmentation is also detectable through blue-shifting and intensity reduction of AuNP SPR seen through UV-vis spectroscopy (Figure 13(c)). However, fragmentation with 800 nm femtosecond pulses typically will not result in uniform AuNPs as shown in Figure 15(f). For that reason, it is often preferable to stop laser irradiation as soon as $[AuCl_4]^-$ reduction is complete [63,77]. In contrast, LFL of AuNPs produced by LAL (rather than LRL) can result in uniform sub-5 nm AuNPs when the fragmentation laser wavelength is in near resonance with the SPR frequency of the AuNPs (~520 nm) [125,221]. Hence, it appears that uniform fragmentation of AuNPs produced by LRL could be achieved with femtosecond laser sources, if their wavelength is around 520 nm. It is noteworthy that laser-induced fragmentation of AuNPs prepared by LRL is suppressed if the liquid media is a mixture of water and hexane. These conditions yield smaller AuNPs, whose diameters are independent of irradiation time, unlike AuNPs synthesized in water [208]. Okamoto et al. [208] proposed that the adsorption of hexane microdroplets onto AuNP surfaces acted like a capping agent, hindering particle growth and aggregation. This interference on the part of hexane results in smaller initial particles that interact weakly with subsequent laser pulses, limiting fragmentation.

Size-control with other capping agents, such as polyvinylpyrrolidone (PVP) [80], polyethylene glycol (PEG) [74], and biopolymers [199,203] is also well-established in LRL. Capping agents have also been used for nanoparticle synthesis in LAL [16,222] and in traditional chemical reduction [223-225]. Although capping agents do effectively control particle sizes, they are not ideal for certain applications. An alternate method for managing particle growth in LRL is through the addition of radical scavengers to the precursor solution. Hydrated electron scavengers like N_2O and O_2; and hydroxyl radical scavengers like alcohol, acetate, and ammonia; have long been shown to hinder the formation of unwanted species in radiolysis experiments [226]. They have since been used to control the reduction kinetics and, by extension, particle sizes in LRL synthesis of Au- and AgNPs [64,73,201,206,207,227].

Frias Batista et al. [206] added hydroxyl radical scavengers to LRL of gold salt solution. Specifically, isopropyl alcohol and sodium acetate were added, in separate experi-

ments, with the goal of limiting H_2O_2 formation during irradiation in a tight-focused geometry (Figure 16(a), (b)). When 10 mM isopropyl alcohol or sodium acetate were added, the AuNP growth was substantially slower than when LRL was conducted in water alone (Figure 16(a)). The rate constants extracted from fitting the results to eq. (19) (Figure 16(b)) indicated a steady decrease of k_2 values as scavenger concentrations increased and H_2O_2 consequently decreased [206]. The unexpected decrease of k_1 as isopropyl alcohol concentration increased was caused by isopropyl alcohol scavenging a portion of the hydrated electrons. Alcohols and solvated electrons react to form deprotonated alkoxides and hydrogen atoms [228]. Belmouaddine et al. [64] investigated the effect of adding the electron scavenger N_2O and isopropyl alcohol to aqueous $[AuCl_4]^-$ during LRL under LDP conditions. Deaerated water saturated with N_2 acted as the control that removed the electron scavenger O_2. The resulting AuNP growth kinetics were substantially faster when isopropyl alcohol was used than when N_2O was used (Figure 16(c)). The k_1 and k_2 rate constants extracted from fitting the results to eq. (21) (Figure 16(d)) indicated that k_1 is more than three orders of magnitude lower when N_2O is used, relative to isopropyl alcohol. The autocatalytic growth rate, k_2, is mostly unaffected. These results are consistent with the electron scavenging activity of N_2O, and the lower H_2O_2 formation rate under LDP conditions. The amplified k_1 rate seen with isopropyl alcohol in LDP conditions contrasts to the comparably lower rate of nucleation seen with isopropyl alcohol under tight-focusing conditions, illustrated in Figure 16(b). This was credited to the action of 2-hydroxy-2-propyl (ketyl) radicals formed via intermolecular hydrogen-

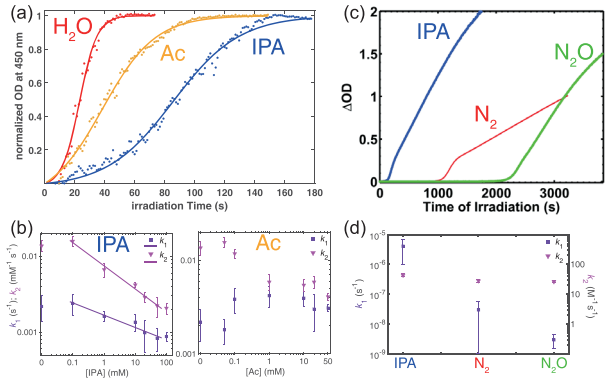

Figure 16 (Color online) AuNP growth (represented by optical density) versus irradiation time in the presence of isopropyl alcohol and sodium acetate (a), and with extracted k_1 and k_2 trends (b). AuNP growth kinetics (c) and extracted rate constants (d) for solutions in the presence of isopropyl alcohol and N_2O. Samples denoted as H_2O and N_2 act as controls, meaning no scavenger was added. Adapted from ref. [206] copyright 2019, American Chemical Society; ref. [64] with permission from the Royal Society of Chemistry.

abstraction by hydroxyl radicals in LDP. Ketyl radicals act as reducing agents to $[AuCl_4]^-$ [64,212]. The contrasting effect of isopropyl alcohol on k_1 in tight-focusing conditions likely results from the higher concentration of hydrated electrons generated, as previously discussed.

The substantial effects of scavengers on AuNP growth-kinetics seen in Figure 16 are reflected in the resulting AuNP sizes, shown in Figure 17. The diameters of AuNPs synthesized under LDP conditions in the presence of N_2 ((29 ± 17) nm) and N_2O ((54 ± 20) nm), were substantially larger and more polydisperse than those of the AuNPs synthesized in isopropyl alcohol ((28.5 ± 5.9) nm) (Figure 17(a)-(c)) [64]. These results are consistent with the prediction that slower nucleation in the presence of e^-_{aq} scavenger will produce large AuNPs, and faster nucleation in the presence of hydroxyl radical scavengers will produce small AuNPs. Under tight-focusing conditions, the substantially lower k_2 values achieved by suppressing H_2O_2-production resulted in Gaussian distributions of AuNP sizes, with mean diameters of 3.78 nm in isopropyl alcohol and 6.07 nm in sodium acetate. In contrast, a log-normal size distribution was obtained in water (Figure 17(d)-(f)) [206].

The pH of the precursor $[AuCl_4]^-$ solution also influences AuNP growth kinetics and final size distributions. Two major consequences of pH are the exchange of Cl^- for OH^-, which forms $[AuCl_x(OH)_{4-x}]^-$; and the variation in availability of water photolysis products [77]. Solution pH therefore extends surprising control over AuNP product-size, exerting a range from ~20 nm at pH 2.5 to ~5 nm at pH 5.4, without the need for surfactants [77]. Under highly acidic conditions (pH ≤ 2.5), the overall reduction rate of $[AuCl_4]^-$ is very slow because of the electron-scavenging activity of H_3O^+, which lowers the nucleation rate, k_1. H_3O^+ imparts a similar effect to that of N_2O, discussed previously [64]. Raising the pH to ~5.4 dramatically increases the overall reaction rate, and reduces AuNP sizes because nucleation rate is much higher. At extremely high pH, the deprotonation of H_2O_2 greatly increases k_2, resulting in very polydisperse AuNPs [77].

Electrolytes in solution can also affect the size-distributions of AuNPs produced by LRL. It has been observed in LAL experiments that small amounts of electrolytes can reduce particle sizes compared to those ablated in deionized water. This is attributed to the adsorption of ions onto AuNPs, and the partial oxidation of gold atoms on the surface of the nanoparticle [221, 222, 229]. LRL syntheses already benefit from small amounts of electrolytes in solution: metal precursors often take the form of salts, HCl and NaOH control the pH of the media and increase the solution's ionic strength. As with LAL syntheses [222, 229], excessive electrolyte concentrations in LRL result in AuNP agglomeration. Exceedingly high ionic strength could account for the rapid

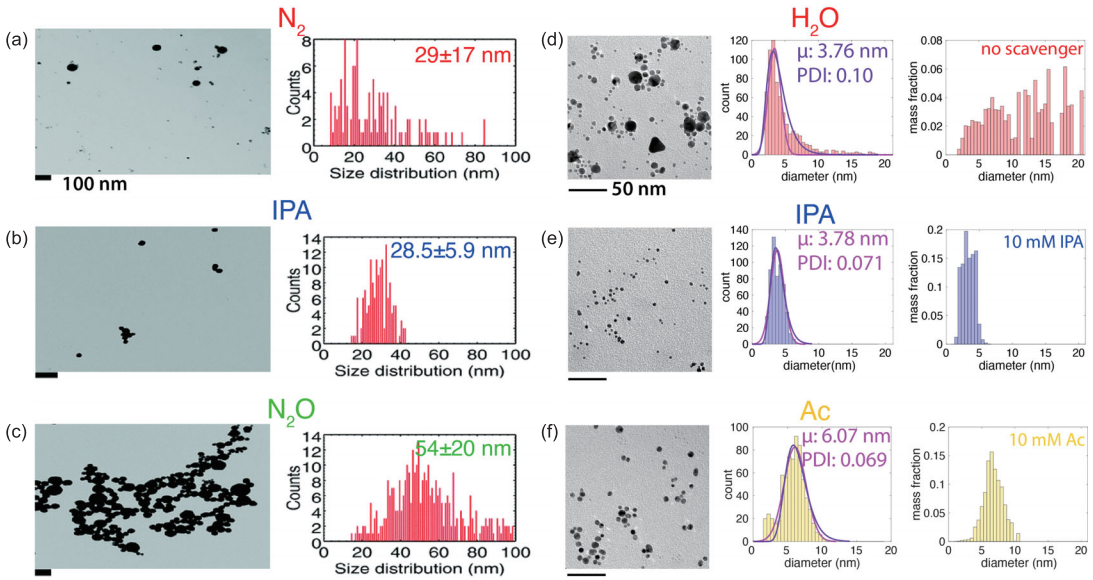

Figure 17 (Color online) Representative TEM images and size-distributions of AuNPs synthesized using: no scavenger (a), (d), isopropyl alcohol (b), (e), N_2O (c), and sodium acetate (f). Adapted from ref. [206] copyright 2019, American Chemical Society; ref. [64] with permission from the Royal Society of Chemistry.

agglomeration of AuNPs synthesized below pH 3, where large quantities of HCl were added [77]. Moreover, although the addition of KCl in modest concentrations (~1 mM) improved the size distribution of AuNPs at pH 6.8, any further increase in KCl concentration (above 10 mM) led to rapid nanoparticle agglomeration [206]. Finally, it should be noted that zeta potential measurements of gold colloids produced with LRL have negative values on the order of −20 to −50 mV [74,204,208]. These are similar to the zeta potential values obtained for AuNPs produced by LAL [221,222,229].

Controlling the solution's chemistry during LRL also makes it possible to produce anisotropic AuNPs [75,76,200], which are useful for biomedical applications because their SPR absorbance can be extended into the NIR region, where tissue absorbance is minimal. Lu et al. [200] synthesized spherical AuNPs, about 2.5 nm wide, by irradiating a solution for two hours; after which the AuNPs clustered into flower-like aggregates, facilitated by the ionic (2-hydroxyethyl) trimethylammonium glycinate liquid present in the sample. Tangeysh et al. [75, 76] capitalized on the H_2O_2-mediated autocatalytic growth of AuNPs to synthesize gold nanotriangles, without added surfactants. They started by synthesizing AuNPs seeds in equilibrium with unreacted $KAuCl_4$ by irradiating with shorts bursts (<1 min). Then, they slowly introduced H_2O_2 after laser irradiation had terminated, producing nanotriangles as large as ~125 nm. Notably, the synthesis route to anisotropic AuNPs through LRL is distinct from LAL in that it is relatively direct. Subsequent laser melting or fragmentation is required [230, 231] to obtain anisotropic AuNPs via LAL. For example, Poletti et al. [231] obtained "nanocorals" (string-like particles) by irradiating LAL-synthesized gold nanospheres dispersed in a 1:1 H_2O:ethanol mixture.

4.1.2 *Silver nanoparticles*

Hydrogen peroxide formed during LRL contributes to the autocatalytic growth of AuNPs. Silver is not so lucky: both H_2O_2 and $OH^\bullet$ back-oxidize Ag^0 to Ag^+ [17,218,232]. As a result, conversion of precursors like $AgNO_3$ and $AgClO_4$ to silver nanoparticles (AgNPs) is more difficult through LRL, especially without the assistance of stabilizers like sodium dodecyl sulfate [233] or excessive (>300 mM) concentrations of silver precursor [234]. To further complicate things, AgNPs formed by LAL on a solid silver target are easily back-oxidized in tight-focusing LFL conditions, because they produce plasmas with high electron densities and concentrations of $OH^\bullet$ [218]. Fortunately, AgNP synthesis by LRL is still possible through the use of radical scavengers, which eliminate oxidizing species like H_2O_2 and its precursor $OH^\bullet$ [73, 201, 227, 233, 235].

Both the Sato group [227] and Tibbetts group [73] observed that adding ammonia (NH_3) to aqueous $AgNO_3$ solutions as a radical scavenger enabled AgNP formation. In both studies, the AgNP shapes and sizes were dependent on the ratio of $AgNO_3$ to NH_3 in the precursor solution (Figure 18). At low $AgNO_3$:NH_3 ratios of 1:2.5 in ref. [73] and 1:17 in ref. [227] (Figure 18, left), large, amorphous plate-like or flake structures are generated. At the "optimal" ratios of 1:10 in ref. [73] and 1:52 in ref. [227] (Figure 18, middle),

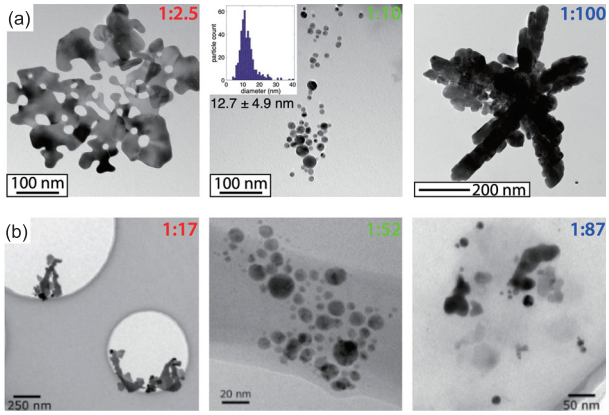

Figure 18 (Color online) TEM images of AgNPs synthesized with different $AgNO_3$:NH_3 ratios using $AgNO_3$ concentrations of 0.1 mM (a) and 0.254 mM (b). Adapted from ref. [73], CC-BY-3.0; ref. [227], CC-BY-3.0.

uniformly spherical AgNPs were produced. As the $AgNO_3$:NH_3 ratio further increased, large AgNP agglomerations were observed (Figure 18, right). The concentration of ammonia in the precursor solution gave rise to similar trends in both of these studies, even though ref. [227] added 0.1 wt% PVP as a capping agent and no stabilizers were used in ref. [73].

The successful generation of AgNPs with the aid of ammonia by LRL was attributed to ammonia's $OH^{\bullet}$ scavenging ability [73, 227] and its tendency to complex with Ag^+ ions to form $Ag(NH_3)^{2+}$ [73, 227, 236, 237]. The scavenging capacity of NH_3 was determined by measuring the amount of H_2O_2 produced after a fixed interval of laser irradiation. Meader et al. [73] found that high concentrations of NH_3 cut the yield of H_2O_2 by 80% or more relative to what was produced by irradiating pure water. Analysis of the kinetics of $AgNO_3$ conversion to AgNPs, measured using UV-vis spectroscopy [73], found accelerated growth kinetics at a low NH_3 concentration of 0.25 mM (a 1:2.5 $AgNO_3$:NH_3 ratio). The growth kinetics slowed as NH_3 concentration increased to 10 mM (a 1:100 $AgNO_3$:NH_3 ratio). This trend was attributed to the Ag^+ and NH_3 complexation equilibrium. At NH_3 concentrations below 1 mM, the solution pH (of 8.42) is lower than the pK_a of NH_4^+ (of 9.26), which disfavors Ag^+ complexation with ammonia to form $Ag(NH_3)_2^+$ [237]. The faster reduction kinetics may therefore result from the higher reduction potential of free Ag^+ as compared to the $Ag(NH_3)_2^+$ complex [236, 237]. At 1 mM NH_3 (the optimal 1:10 $AgNO_3$:NH_3 ratio), the solution pH rose to 9.47, at which a small amount of NH_4^+ was present and most Ag^+ was complexed into $Ag(NH_3)_2^+$. This complexation slows the reduction kinetics sufficiently, allowing spherical AgNPs to form. As the NH_3 concentration is further increased, a competing reaction mechanism takes place: the excess NH_3 in solution reacts with the $OH^{\bullet}$ radicals, forming peroxynitrate ($ONOO^-$), a strong oxidant. The presence of $ONOO^-$ further slows Ag^+ reduction, to produce large agglomerates of AgNPs. Nanoparticle formation is completely impeded at NH_3 concentrations above 20 mM [73]. Collectively, these results indicate that for the optimal reduction of Ag^+, it is imperative to balance the concentration of ammonia in the precursor solution. There must be enough to allow the formation of the $Ag(NH_3)_2^+$ complex, but not so much as to invite excess peroxynitrite.

Another hydroxyl radical scavenger used in LRL AgNP synthesis is isopropyl alcohol. Abid et al. [233] reported that an isopropyl alcohol concentration of 500 mM decreased the rate of AgNP formation in the presence of sodium dodecyl sulfate by a factor of about 25% when irradiating with 500 nm, 6 ns pulses. The authors hypothesized that isopropyl alcohol limits not only the concentration of hydroxyl radicals, but also that of hydrogen radicals, which assist in Ag^+ reduction [233]. The Tibbetts group found that adding isopropyl alcohol as a radical scavenger enables AgNP synthesis in focused, 800 nm, 30 fs pulses [235]. The well-defined, broad absorption peak around 400 nm, indicating the SPR of the AgNPs, emerges only when $AgClO_4$ is irradiated in a solution with an isopropyl alcohol concentration of 2.5 mM or higher [235]. Nanoparticle growth remained constant as isopropyl alcohol concentration increased beyond that.

4.1.3 Palladium nanoparticles

Palladium nanoparticles (PdNPs) have been produced by LRL without the need of any additives in aqueous [238, 239] and organic [240] solutions, although capping agents are often used [241-243]. A noteworthy impediment to controlling LRL-synthesized PdNP outcomes is that the precursors, potassium tetrachloropalladate (K_2PdCl_4) and palladium nitrate ($Pd(NO_3)_2$), tend to form aqua-complexes in aqueous solution. These complexes undergo hydrolysis and consequently form polymeric oxides [244]. Because the formation of these oxidized polymeric species can be delayed at low pH values [245, 246], Frias Batista et al. [239] acidified their palladium precursor solutions. They found that LRL of K_2PdCl_4 and $Pd(NO_3)_2$ precursors in the absence of acid yielded large, anisotropic PdNPs (nanoflowers from K_2PdCl_4 and nanopopcorn from $Pd(NO_3)_2$) with high polydispersity, presumably caused by oxidative degradation. The addition of acid in the form of HCl or HNO_3 had a stabilizing effect on the precursor solutions. Synthesis proceeded, culminating in ultra-small, spherical nanoparticles with mean diameters of 1.2 nm for $Pd(NO_3)_2$ in HNO_3, and 3.1 nm for K_2PdCl_4 in HCl. Larger, anisotropic nanoparticles also formed, apparently comprising aggregated ultra-small nanoparticles (Figure 19(a), (b)). These anisotropic PdNP nanostructures are

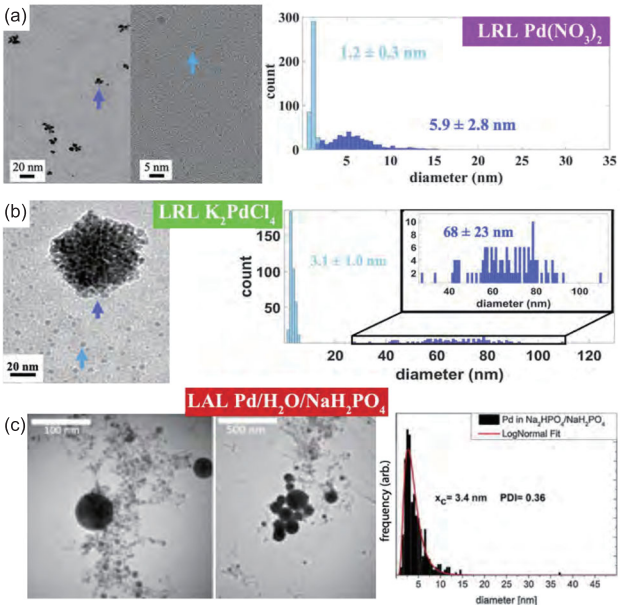

Figure 19 (Color online) TEM images of PdNPs synthesized through LRL with $Pd(NO_3)_2$ (a) and K_2PdCl_4 (b) precursors at pH < 3; and through picosecond-LAL of palladium in a sodium phosphate solution (c). Adapted with permission from ref. [239] copyright 2021, with permission from Elsevier; ref. [253] copyright 2015, with permission from Elsevier.

distinct from the PdNPs obtained by LAL in aqueous solution without capping agents [247-253]. For instance, Marzun et al. [253] produced ~3.4 nm PdNPs with a log-normal size distribution by ablating a palladium target with 1064 nm, 9.8 ps pulses, in μM concentrations of added phosphate. Several large (>100 nm) spherical PdNPs were also present (Figure 19(c)).

LRL in organic solvents has also been used to produce PdNPs [240, 243]. Saeki et al. [243] studied the reaction kinetics of $PdCl_4^{2-}$ in a water-ethanol mixture as it was irradiated with 266 nm, 8 ns pulses under low fluence (30-50 mJ cm^{-2}) wherein no plasma was formed. The reaction kinetics of PdNP formation, extracted from dispersive XAFS measurements, followed the Finke-Watzky two-step mechanism (cf. sect. 4.1.1 and eq. (20)). In the water-ethanol mixture, palladium nucleation is initiated by electron transfer from ethanol to the $PdCl_4^{2-}$ ion,

$$[PdCl_4]^{2-} + CH_3CH_2OH + nh\nu \xrightarrow{k_1} Pd(0) + CH_3CHO + 2H^+ + 4Cl^-, \quad (24)$$

which is followed by fast formation of $(Pd)_m$ nuclei. The nuclei increase in size through autocatalytic growth, via the reaction

$$Pd(0)_m + [PdCl_4]^{2-} + CH_3CH_2OH + nh\nu \xrightarrow{k_2} Pd(0)_{m+1} + CH_3CHO + 2H^+ + 4Cl^-. \quad (25)$$

Analysis of the dependence of k_1 and k_2 on laser fluence (F) found that $k_1 \sim F^{0.54\text{-}1.03}$, suggesting that the initial photoreduction described in eq. (24) is a one-photon process. However, k_2 exhibited a stronger dependence: $k_2 \sim F^{3.35\text{-}4.09}$; suggesting that the autocatalytic growth of the PdNPs (eq. (25)) is sustained by multiphoton processes. Gold also follows the Finke-Watzky model, yet the reduction of aqueous $KAuCl_4$ in sufficiently low-fluence nanosecond laser pulses to avoid plasma formation actually inverts the trend seen in palladium [71]. When gold metal is the target, k_1 has a much stronger dependence on fluence than does k_2 ($k_1 \sim F^{10}$ and $k_2 \sim F^1$) [71]. This difference could simply be a product of the difference in laser wavelength used by each research group (532 nm for gold in ref. [71] versus 266 nm for palladium in ref. [243]). Another difference was the absence of organic solvent in the experiments on gold, which might have acted as a reducing agent had it been present.

4.1.4 *Platinum nanoparticles*

Platinum nanoparticles (PtNPs) have been synthesized through LRL of aqueous K_2PtCl_6 salt; with [201, 241] and without [201, 238, 242] capping agents. Platinum nanoparticles were first achieved using 800 nm, 100 fs laser irradiation of aqueous K_2PtCl_6, both with and without additives (PVP and ammonia) [201]. The nanoparticles prepared without additives had an average particle size of 11.3 nm (Figure 20(a)), which was considerably larger than those that were synthesized in the presence of the capping agent PVP ((3.2 ± 1.4) nm). In contrast to PVP, irradiation of platinum in ammonia solution led to the formation of platinum aggregates (Figure 20(b)). The authors explained that ammonium hexachloroplatinate (VI), $(NH_4)_2PtCl_6$, the complex that forms in the presence of ammonia, decreases platinum's reduction potential. A similar phenomenon occurs with a silver (see sect. 4.1.2). A lowered reduction potential would slow nucleation, favoring particle growth and leading to aggregation. Moreover, the addition of PVP at a concentration of 0.01 wt% was insufficient to prevent the formation of platinum aggregates in ammonia solution [201]. Fan et al. [241] were able to synthesize anisotropic PtNPs using 800 nm, 100 fs pulses at a low intensity: 10^{14} W cm^{-2}. They concluded that by limiting platinum nucleation with a low-intensity beam, slow crystal growth along a certain crystal vector was encouraged. Propagating growth only along certain surfaces minimizes the surface free energy, yielding nanoparticles in the shape of stars (Figure 20(c)) rather than the spheres that would result from even isotropic growth in all directions. It is more difficult to exercise control over PtNP size and morphology with LAL than it is with LRL. Ablating solid platinum targets most often produces large, polydisperse PtNPs [254, 255], although the use of laser wave-

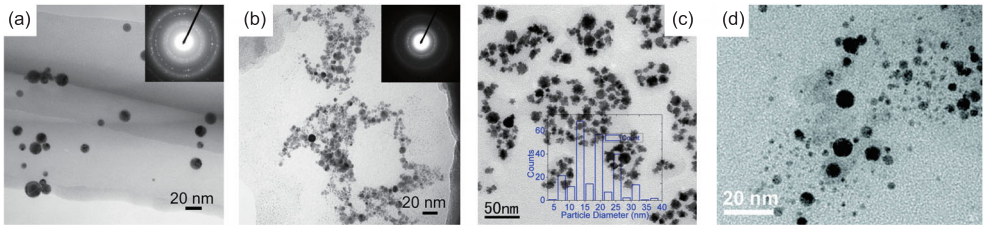

Figure 20 (Color online) Representative TEM images of PtNPs synthesized through LRL with 800 nm, 100 fs pulses in pure water with high intensity (a), in ammonia solution (b), in pure water with low intensity (c), and through LAL with 266 nm, 5 ns pulses (d). Adapted with permission from ref. [201] (a), (b), copyright 2012, with permission from Elsevier; ref. [241] (c), copyright 2013, with permission from Elsevier; and ref. [254] (d), copyright 2011 American Chemical Society.

lengths in the UV range can produce smaller PtNPs (Figure 20(d)) because that range is near the nanoparticle's extinction maximum [254]. This self-absorption-induced fragmentation is similar to that which occurs in AuNPs when they are irradiated with wavelengths that are resonant with their SPR feature [71, 125, 256].

4.1.5 Summary

Table 3 lists LRL syntheses of noble-MNPs, indicating for each the solution (pH, additives), capping agent, and laser irradiation conditions used. Reported size distributions and particle size ranges are shown where available. In addition to the Au-, Ag-, Pd-, and PtNPs discussed earlier, the table includes Rh- and IrNPs synthesized from chloride salts with LRL [238, 242, 257].

4.2 Base metal and oxide nanoparticles

Laser reduction in liquid is also used to synthesize nanoparticles comprising base metals and oxides. Iron is the most popular subject of this research. As with LAL (see sect. 3.3), one of the advantages of LRL is the ability to manufacture graphite-coated nanoparticles in ambient conditions, a task which would typically require temperatures exceeding 800°C. The majority of the studies covered in this section use unfocused, nanosecond pulses. It can be assumed that irradiation methods follow these parameters unless specified otherwise. All of the reaction parameters for the syntheses outlined in this section are summarized in Table 4.

Ye et al. [258] reported the first room-temperature synthesis of graphite-coated FeNPs in solution. They irradiated $Fe_3(CO)_{12}$ and triphenylphosphine, PPh_3, in deoxygenated hexanes (Figure 21(a)). Without PPh_3, or in an oxygenated solvent, no product formed. In the absence of PPh_3, no graphitic shells were found in deoxygenated toluene; a contrast to the LAL results in the literature described in sect. 3.3. The authors hypothesized that under intense laser irradiation, the precursor ($Fe_3(CO)_{12}$) dissociates into iron atoms and CO, after which the iron atoms coalesce into nanoparticles. Free phosphines are then adsorbed on the surface of the iron particles. With continued irradiation, the phenyl rings on PPh_3 undergo graphitization and form the graphite layers around the iron cores.

Park et al. [259] created carbon-encapsulated nanoparticles of iron, nickel, and cobalt by irradiating xylene solutions of ferrocene, nickelocene and cobaltocene respectively, with 355 nm laser pulses. Nanoparticles with diameters ranging from 10 to 500 nm were observed in all instances, with varying degrees of graphitization depending on size. For a nickel, bigger nanoparticles (>100 nm) had amorphous carbon shells, whereas smaller particles were encased in graphitic shells with low crystallinity (Figure 21(b)). Similar results were seen in iron. Contrastingly, CoNPs were encapsulated in thick graphitic shells with a higher degree of crystallinity relative to both Fe- and NiNPs, no matter their size (Figure 21(c)). Because low graphitization of the carbon shell is associated with lower solution temperature, the authors concluded that cobaltocene-xylene solutions must reach higher solution temperatures during laser irradiation. The UV-vis absorption spectra revealed a considerably higher absorption of 355 nm photons by cobaltocene-xylene solutions compared to the other solutions (Figure 21(d)). This higher absorption might have supplied both the energy and temperature necessary to produce the well-ordered graphitic layers seen in the CoNPs.

Hayasaki et al. [260] synthesized carbon coated Fe- and CoNPs from ferrocene and cobaltocene in sub- and supercritical benzene precursors at temperatures from 25°C to 290°C, using 266 nm UV laser irradiation. Amorphous shells were observed at temperatures below 200°C, while carbon "onions" emerged at higher temperatures. In addition to benzene, the authors also recognized the cyclopentadienyl (Cp) rings from the metallocenes as carbon sources on the basis of earlier results, gathered by ablating dry metallocene powders [261]. The decomposition energies for $Fe(Cp)_2 \rightarrow Fe + 2Cp$ at 6.80 eV and $Co(Cp)_2 \rightarrow Co + 2Cp$ at 5.64 eV [262, 263], and the energy required to remove one hydrogen

Table 3 Noble-MNPs synthesized by LRL. Acronyms: PVP is polyvinylpyrrolidone; PEG is polyethylene glycol; PVA is poly(vinyl)alcohol; IPA is isopropyl alcohol; citrate is trisodium citrate dihydrate; SDS is sodium dodecyl sulfate

Ref.	Precursor	Capping agent	Solution conditions	Laser	Size [range][a)]
[80]	1 wt% $HAuCl_4$	1 wt% PVP	H_2O	800 nm, 100 fs	3 ± 2[b)] [2-7]
[74]	0.5 mM $KAuCl_4$	0.125 mM PEG	H_2O, pH 4.4-4.7	800 nm, 36 ps	3.9 ± 0.7 [2-8]
[70]	0.1 mM KAuCl4	0.045 mM PEG	H_2O	800 nm, 36 ps	5.8 ± 1.1 [3-10]
[204]	0.25 mM $HAuCl_4$	–	H_2O, flow	800 nm, 100 fs	4.3 ± 2.0 [2-15]
[77]	0.1 mM $KAuCl_4$	–	H_2O, pH 5.4	800 nm, 36 ps	4.8 ± 1.9 [2-15]
[64]	1 mM $HAuCl_4$	0.2 M IPA	H_2O	800 nm, 35 fs	28.5 ± 5.9 [18-42]
[63]	0.1 mM $KAuCl_4$	–	H_2O, pH 5.4	800 nm, 30 ns	3.5 ± 1.9 [2-16]
[205]	0.75 mM $HAuCl_4$	0.1 M PVA	H_2O	800 nm, 35 fs	5.4 ± 1.7 [2-12]
[71]	0.1 mM $KAuCl_4$	–	H_2O, pH 5.4	532 nm, 8 ns	5.1 ± 1.0 [2-9]
	0.1 mM $KAuCl_4$	–	H_2O, pH 5.4	800 nm, 30 fs	14 ± 6 [3-30]
[208]	0.1 mM $HAuCl_4$	–	1:1, H_2O:*n*-hexane	800 nm, 40 fs	4.1 ± 0.8 [2-8]
[206]	0.1 mM $KAuCl_4$	–	H_2O, IPA, pH 6.7	800 nm, 30 fs	3.8 ± 0.9 [2-7]
[233]	0.833 mM $AgNO_3$	SDS	H_2O, IPA	500 nm, 6 ns	13.3 ± 2.6
[234]	300 mM $AgNO_3$	–	H_2O	800 nm, 100 fs	4.4 ± 2.61
	300 mM $AgNO_3$	0.01 wt% PVP	H_2O	800 nm, 100 fs	2.2 ± 0.89
[198]	1 mM $AgNO_3$	–	hexane	800 nm, 100 fs	5.52 ± 1.15
[227]	0.254 mM $AgNO_3$	0.01 wt% PVP	H_2O, NH_3	801 nm, 100 fs	10.3 ± 8.5
[73]	0.1 mM $AgNO_3$	–	H_2O, NH_3	800 nm, 30 fs	12.7 ± 4.9
[240]	3 mM $PdCl_2$	–	ethanol	800 nm, 120 fs	3.4 ± 2.0
[238]	0.25 mM $PdCl_2$	–	H_2O	800 nm, 100 fs	8.5 ± 3.3
[241]	0.2 mM $PdCl_2$	2 wt% PVP	ethanol	800 nm, 120 fs	8 [1-30]
[242]	0.25 mM $PdCl_2$	citrate	H_2O	800 nm, 100 fs	8.5 ± 2.1
[243]	15 mM Na_2PdCl_4	PVP	1:1, H_2O:ethanol	266 nm, 8 ns	[1-150][b)]
[239]	0.5 mM K_2PdCl_4	–	H_2O, HCl	800 nm, 30 fs	$3.1 \pm 1.0, 68 \pm 23$
	0.5 mM $Pd(NO_3)_2$	–	H_2O, HNO_3	800 nm, 30 fs	$1.2 \pm 0.3, 5.9 \pm 2.8$
[238]	0.25 mM $RhCl_3$	–	H_2O	800 nm, 100 fs	3.7 ± 2.5
[242]	0.25 mM $RhCl_3$	citrate	H_2O	800 nm, 100 fs	16.5 ± 6.5
[201]	0.254 mM H_2PtCl_6	–	H2O	800 nm, 100 fs	11.3 ± 4.3
	0.254 mM H_2PtCl_6	0.01 wt% PVP	H_2O	800 nm, 100 fs	3.2 ± 1.4
[241]	0.254 mM H_2PtCl_6	0.01 wt% PVP	H_2O	800 nm, 120 fs	13.5 [1-40]
[238]	0.25 mM H_2PtCl_6	–	H_2O	800 nm, 100 fs	14.3 ± 6.7
[242]	0.25 mM H_2PtCl_6	citrate	H_2O	800 nm, 100 fs	9.5 ± 2.3
[257]	0.25 mM H_2PtCl_6	–	H_2O	800 nm, 100 fs	< 20[c)]

a) Sizes reported in nanometers. b) Estimated from reported histogram. c) Estimated from TEM images.

atom from benzene, 4.90 eV [264], are all above the 4.66 eV of the 266 nm irradiating photon. Thus, the authors proposed that two-photon absorption resulted in the isolation of iron or cobalt atoms and Cp-rings. They further proposed that during the time between pulses, the iron and cobalt atoms cooled and coagulated to create nuclei, transferring surplus energy to the Cp-rings and benzene to produce the carbon-onion shells.

Moussa et al. [265] synthesized various Fe-Fe_2O_3 nanoparticles from $Fe(CO)_5$ using 532 nm nanosecond laser pulses in toluene, tetrahydrofuran, dimethyl sulfoxide, and acetonitrile. Graphitic shells were formed in toluene, whereas the nanoparticles were embedded in amorphous carbon matrices in the other three solvents. Similar results were obtained with a 355 nm laser. More than just the carbon structure, the solvent also determined the nanoparticles' crystallinity and phase. Crystalline α-FeNPs were obtained from toluene; mixtures of γ-Fe and Fe_2O_3 were obtained from both dimethyl sulfoxide and acetonitrile; and amorphous FeNPs were obtained from tetrahydrofuran. This solvent dependence on the part of both the nanoparticle phase and carbon-shell structure in LRL is similar to the behavior of iron in organic solvents during LAL, described in sect. 3.3. The authors noted that the bulk solution temperature increased to ~65°C-70°C in iron precursor solutions, regardless of solvent, after 5 min of irradiation with 532 nm pulses. Negligible temperature changes were seen when the pure solvents were irradiated, implying high photothermal effect connected to the photodecomposition of $Fe(CO)_5$.

Table 4 Transition metal nanoparticles produced by LRL. THF is tetrahydrofuran; DMSO is dimethyl sulfoxide, MeCN is acetonitrile, acac is acetylacetone

Ref.	Precursor	Solvent	Laser	Product	Size (nm)
[258]	1 $Fe_3(CO)_{12}$:20 PPh_3, 1 mM $Fe_3(CO)_{12}$	deoxygenated hexane	355 nm, 10 ns	bcc-Fe@C	[20-200][a]
[259]	2 mg/mL ferrocene	xylene	355 nm, 5 ns	Fe@C	[10-500][a]
	2 mg/mL nickelocene	xylene	355 nm, 5 ns	Ni@C	[10-200][a]
	2 mg/mL cobaltocene	xylene	355 nm, 5 ns	Co@C	[10-200][a]
[260]	3.52 mg/mL ferrocene	benzene	266 nm, 4.3 ns	Fe@C	7.5 ± 5.2
	3.52 mg/mL cobaltocene	benzene	266 nm, 4.3 ns	Co@C	7.2 ± 3.6
[265]	100 μL/10 mL $Fe(CO)_5$	MeCN, THF, DMSO	532 nm or 355 nm, 7 ns	Fe-Fe_2O_3	[5-25][a]
[265]	100 μL/10 mL $Fe(CO)_5$	toluene	532 nm or 355 nm, 7 ns	Fe-Fe_2O_3@C	[5-25][a]
[266]	10 mM ferrocene	hexane	355 nm, 8 ns	Fe, Fe_3O_4	47.2 ± 27.7
	10 mM ferrocene	hexane	800 nm, 40 fs	Fe, Fe_3O_4	33.3 ± 17.8
[267]	1 mM $Fe(acac)_3$	hexane	800 nm, 40 fs	Fe_3O_4	10.5 ± 3.5
	1 mM $Fe(acac)_3$	water	800 nm, 40 fs	Fe_3O_4	4.9 ± 1.9
[268]	10 mM ferrocene	hexane-water	800 nm, 40 fs	Fe-O	7[b]
[104]	0.9 mM copper acetate	MeCN	790 nm, 35 fs	Cu_2O	3.5 ± 0.7
[270]	0.8 mM $Cu(acac)_2$	IPA-methanol	800 nm, 30 fs	Cu	[3-120][a]

a) Estimated from TEM images. b) With a 50% coefficient of variation.

The Yatsuhashi group recently reported multiple LRL routes for bare FeNP synthesis in amorphous carbon-matrices using different laser parameters, precursors, and solvents [266-268]. In their initial publication [266], the authors irradiated 1 mM ferrocene-in-hexane solutions for 120 min, with a near-IR femtosecond laser (Figure 22(a)) and a UV nanosecond laser (Figure 22(b)), procuring bare FeNPs. Their findings contrasted with earlier LAL studies of iron [154, 157, 158], and LRL of ferrocene in benzene [269], in which FeNPs with carbon shells were produced. The mean size of the spherical nanoparticles was (33.3 ± 17.8) nm for the one made using the near-IR femtosecond laser, and (47.2 ± 27.7) nm for the ones made using the UV nanosecond laser. Most of the nanoparticles were iron oxide, due to the lack of carbon encapsulation and the presence of ambient dissolved oxygen during laser irradiation. The absence of carbon shells from hexanes after femtosecond laser irradiation was consistent with their previous study [107], wherein carbon products were generated from aromatic hydrocarbons but not from aliphatic hydrocarbons. The authors, therefore, reasoned that the amorphous carbon matrix surrounding these nanoparticles was derived from ferrocene Cp-rings. Because of the different mechanisms that occur in the nanosecond and femtosecond laser irradiations, the authors proposed limiting themselves femtosecond pulses for the sake of regulating nanoparticle size, and using precursors with readily-degradable ligands, instead of Cp-rings, to control carbon quantity.

In an ensuing article [267], the Yatsuhashi group replaced ferrocene with tris(acetylacetonato) iron(III) ($Fe(acac)_3$) in hexane solution, but otherwise used similar reaction parameters as ref. [266]. The only other change was the irradiation time of 25 min. Nanoparticle sizes were (12.9 ± 5.3) nm for the sample collected 10 min after the 25 min irradiation time (Figure 22(c)), whereas the mean nanoparticle size using ferrocene was ~25 nm. The authors also irradiated $Fe(acac)_3$ in water, producing iron oxide nanoparticles with a mean size of ~5 nm regardless of the irradiation time. Interestingly, no carbon agglomerates were observed for the immediately-collected hexane or water samples; but the hexane samples that were collected 10 min after irradiation was terminated showed less carbon formation than the samples irradiated in ferrocene (compare Figure 22(a), (c)). Because the nanoparticle sizes for $Fe(acac)_3$ in both water and hexane were smaller, the authors proposed that the acetylacetonate (acac) ligands protected the particles from aggregation with their strong coordination ability. They were further able to control the size of FeNPs by irradiating a solution of water and ferrocene-hexane with near-IR femtosecond laser pulses [268]. The nanoparticles collected from the water layer with 1 mM ferrocene had an average size of only 6 nm; and few particles were larger than 10 nm (Figure 22(d)). As the ferrocene was only dissolved in the hexane, the authors reasoned that microdroplets of hexane could be considered tiny reaction vessels dispersed in water. Consequently, the likelihood of primary particle agglomeration is reduced, causing smaller nanoparticle sizes.

Copper nanoparticles have also been produced with LRL. Tangeysh et al. [104] synthesized Cu_2O-polyacetonitrile nanocomposites by irradiating acetonitrile solutions containing a copper(II) acetate dimer with near-IR femtosecond laser pulses, under SSTF conditions (cf. sect. 4.1.1). Polymeric networks comprising 3 nm particles were found in samples that had been irradiated for up to 40 s (Figure 23(a)), but very

few nanoparticles were found in samples that were irradiated for as long as 60 s (Figure 23(b)). Copper precursors that do not form dimers did not yield nanoparticles. Copper(II) butyrate, another dimer-forming precursor, did yield a product comparable to that formed in copper(II) acetate, reinforcing the necessity of using a dimer-forming precursor to obtain any products. Using FTIR, Raman, and mass spectrometry, the authors determined that HCN generated during the reaction, and trace amounts of H_2O present in the solvent, play essential roles in the composition of the end product. Hydrogen cyanide generated during laser fragmentation of nitriles works as a reducing agent, converting Cu(II) to Cu(I), which is then hydrolyzed to Cu_2O in the presence of water. The samples irradiated for 40 s or less produced a higher ratio of water than HCN, making Cu_2O the dominant product. The samples irradiated for 60 s produced a higher HCN ratio, leading to the formation of amorphous CuCN polymer and hindering nanoparticle generation.

One challenge to LAL synthesis of CuNPs is avoiding copper oxidation [121, 126]. Nag et al. [270] recently reported the production of air-stable CuNPs by irradiating copper acetylacetonate ($Cu(acac)_2$) in an isopropanol-methanol solution with tightly-focused near-IR femtosecond laser pulses. The authors purged the precursor solution with nitrogen before laser irradiation to minimize the quantity of dissolved oxygen, which is a contributor to CuNP oxidation in LAL [121]. The resulting nanoparticles were embedded in a carbon matrix (Figure 23(c)). Data gathered by UV-vis absorbance and XRD measurements after the CuNPs were exposed to air for seven days showed that the initial, crystalline CuNPs had remained stable and unoxidized (Figure 23(d)). The authors ascribed this stability to the presence of carbon surrounding the nanoparticles. They hypothesized that this coating occurred as a result of C-C coupling between solvent fragments and ligands, generated during laser-irradiation on CuNP surfaces [270].

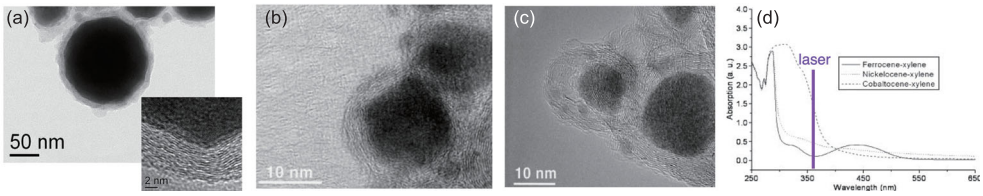

Figure 21 (Color online) TEM images of Fe@C nanoparticles from $Fe_3(CO)_{12}$ in PPh_3 and hexane (a); Co@C nanoparticles with a high degree of shell graphitization (b); Ni@C nanoparticles with a low degree of shell graphitization (c); and UV-vis absorbance showing higher absorption of 355 nm photons by cobaltocene-xylene solutions (d). Adapted from ref. [258] (a), copyright 2007 American Chemical Society; and ref. [259] (b)-(d), copyright 2008, with permission from Elsevier.

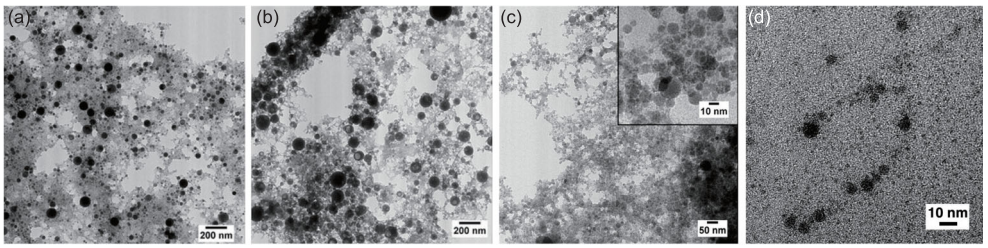

Figure 22 TEM images of Fe@C nanoparticles synthesized from ferrocene in hexane with femtosecond (a) and nanosecond (b) pulses; of $Fe(acac)_3$ in hexane with femtosecond pulses (c); and of ferrocene in a water-hexane mixture (d). Adapted from ref. [266] (a), (b), copyright 2018 Wiley-VCH; ref. [267] (c), with permission from the Chemical Society of Japan; and ref. [268] (d), copyright 2020 with permission from Elsevier.

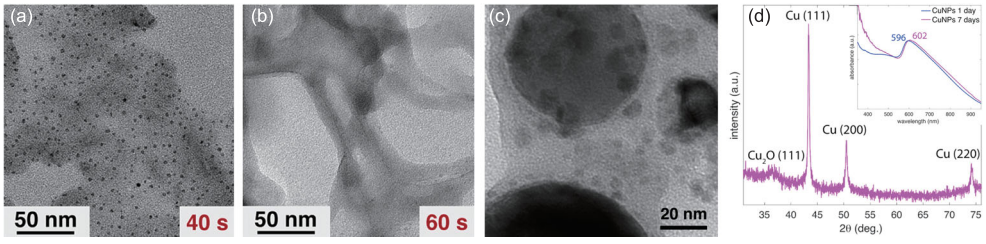

Figure 23 (Color online) TEM images of Cu_2O-polyacetonitrile composites (a) and CuCN polymer (b), synthesized from copper(II) acetate in acetonitrile. TEM image of Cu@C nanoparticles synthesized from $Cu(acac)_2$ in an isopropanol-methanol mixture (c), with XRD and UV-vis spectra (d). Adapted from ref. [104] (a), (b) copyright 2019, American Chemical Society; and ref. [270] (c), (d), CC-BY-3.0.

4.3 Alloy nanoparticles

Laser reaction in liquid has developed strategies for synthesizing solid-solution alloys from immiscible metals, with composition and size-tunability, over the last decade. Most of the reported syntheses involve irradiating aqueous noble metal solutions with tightly-focused near-IR femtosecond laser pulses (unless otherwise stated). These laser parameters produce high laser intensities that initiate the reaction chemistry described in sect. 2.1; reducing metal ions and initiating alloy nanoparticle synthesis. The mechanisms governing noble metal reduction and noble-MNP formation have been examined in sect. 4.1. As a special mention, we would like to acknowledge Takahiro Nakamura and Shunichi Sato's enormous contributions to the development of the LRL technique for alloy nanoparticle synthesis; 75% of the literature covered in this section comes from their group [198, 201, 242, 257, 271-278].

Herbani and colleagues have published many papers on the LRL technique as it applies to the production of Au-Ag solid-solution alloy nanoparticles. In 2010, they published the first homogenous Au-Ag alloys, with various compositions, that had been produced through LRL [271]. Aqueous solutions comprising 0.01 mM $HAuCl_4$ and $AgNO_3$ both were used as precursors, and PVP was used as a capping agent. Their product yields were very low, due to the low precursor concentration, which was a deliberate measure taken to avoid unwanted AgCl precipitates before laser irradiation. On the basis of an SPR peak in their UV-vis absorbance spectra which blue-shifted as the concentration of silver increased, and high resolution TEM analysis, they concluded that the Au-Ag alloy nanoparticles were homogeneous. Regardless of composition, the nanoparticle diameters were 2-3 nm, likely due to low precursor concentration which limited particle growth. For all solution compositions, the SPR peak blue-shifted as irradiation time increased. This indicated the reduction of gold ions first, followed by silver incorporation into the nanoparticles at later times. The authors postulated that Au^{3+} species are reduced to gold atoms first, due to their higher reduction potential, and Ag^+ is reduced second, onto the surfaces of the AuNPs. Although this process could be expected to culminate in core-shell formations, they proposed that steady irradiation allowed the silver atoms to diffuse into the gold-dominated nanoparticles; facilitated by the highly reactive environment. Notably, all the alloy nanoparticles had a substantially higher gold content compared to the initial precursor ratios: solutions with 25%, 50%, and 75% gold corresponded to nanoparticles with 67%, 74%, and 88% gold content, respectively.

To overcome the inefficiency of silver incorporation into Au-Ag alloy nanoparticles seen with LRL, Nguyen et al. [235] used isopropanol as a $OH^\bullet$ radical scavenger, with no additional capping agents. As mentioned in sect. 4.1.2, hydroxyl radicals back-oxidize Ag^0 to Ag^+, impeding AgNP production. Moreover, the recombination of $OH^\bullet$ into H_2O_2 initiates autocatalytic reduction of $AuCl_4^-$, promoting AuNP growth. For 0.1 mM metallic precursors and optimal isopropanol concentration of 20 mM, the final compositions of the Au-AgNPs, as measured by STEM-EDX mapping, matched the initial gold and silver precursor ratios to within ~15% (Figure 24(a)). This contrasts with the proportionally high gold content observed by Herbani et al. [271] in 2010. Nguyen et al. tracked the evolution of the SPR peaks *in situ*, for several Au:Ag ratios and isopropanol concentrations, to derive detailed reaction kinetics for Au-Ag alloy nanoparticle formation. By modeling the fractional silver composition as a function of laser-processing time, using Mie theory, they found that gold-rich compositions were present at early processing times, with silver content increasing at later times (Figure 24(b)). On the basis of this data, the authors proposed the following 4-step mechanism (Figure 24(c)): (1) the higher reduction potential of $AuCl_4^-$ compared to Ag^+ and the back-oxidation of Ag^0 by $OH^\cdot$ result in faster $AuCl_4^-$ reduction, leading to (2) nucleation of gold-rich nanoparticles; (3) autocatalytic AuNP growth dominates as H_2O_2 builds up in solution, leading to further increase in Au content; and (4) once the majority of the $AuCl_4^-$ has been reduced, Ag^+ is reduced and incorporated into Au-AgNPs. By adding isopropanol to temper steps (1) and subsequently (3), they were able to achieve alloy nanoparticles with more balanced Au:Ag ratios. As with ref. [271], LRL produced homogeneous alloy nanoparticles despite the similarly sequential reduction of gold and silver ions.

Herbani et al. [198] avoided the problem of silver back-oxidation by using hexane as a solvent, and dodecylamine as a capping agent, to produce Au-AgNPs. This was the first LRL publication on the production of alloys in organic

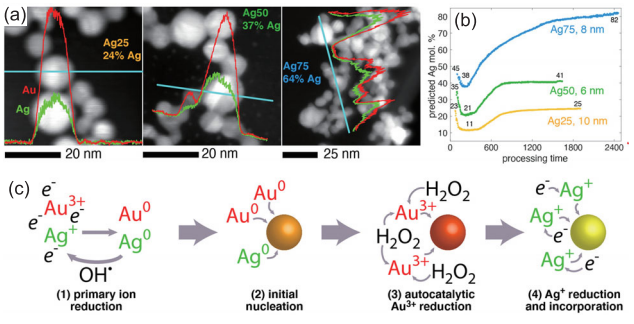

Figure 24 (Color online) STEM-EDX images and maps of Au-AgNPs (a); predicted fractional silver composition as a function of laser processing time (b); proposed alloying mechanism (c). Adapted from ref. [235], copyright 2021 American Chemical Society.

solvents. Aqueous solutions containing 1 mM $HAuCl_4$ and $AgNO_3$ were transferred into hexane using a phase-transfer technique with 96% efficiency for gold ions and 92% efficiency for silver ions. Hexane was chosen as a solvent because it has a similar refractive index to water, and is less degraded by high-intensity femtosecond laser irradiation than are aromatic solvents like toluene. Watching the SPR absorbances of monometallic gold and silver precursors as they changed with irradiation time revealed that silver reduces faster in hexane (Figure 25(a)), in contrast to water [235, 271]. The reducing species created during the breakdown of hexane (cf. sect. 2.2) reduce the metal ions to atoms with limited back-oxidation, which could explain why silver is reduced faster. Despite the differences in nucleation rates, only a single SPR peak was found across all compositions of the final, alloy product (Figure 25(b)). Homogeneous alloy production was confirmed with high resolution TEM lattice fringe analysis (Figure 25(c)), correlating with aqueous studies [235, 271]. Unlike in the water-synthesis trials [271], the average nanoparticle diameters in hexane increased from 2 to 5 nm as the concentration of gold increased.

Chau et al. [272] synthesized Pt-AuNPs in aqueous solutions using PVP as a capping agent. Synthesizing Pt-Au alloys is difficult because of the opposing reduction kinetics of platinum and gold, as well as the fact that gold atoms are much larger than platinum atoms, causing lattice strain that might encourage gold segregation. The authors ascribed the success of homogeneous Pt-Au alloy nanoparticle synthesis to the creation of a strong field generated by laser irradiation. The alloy nanoparticle sizes were ~60 nm without PVP, and ~15 nm with PVP. The authors used a similar method to manufacture Fe-Pt alloy, substituting the gold precursor for an iron precursor [279]. Nakamura et al. [273] also reported the production of Pt-Au alloy nanoparticles under reaction conditions comparable with ref. [272], but without capping agents, and with stronger pulse energy (5 mJ instead of 3 mJ). They reported a wide range of alloy compositions, whereas Chau et al. [272] only reported one. The most notable distinction between the two findings is that Nakamura's nanoparticles had a 4 nm diameter, compared to Chau's uncapped 60 nm particles. This disparity could be explained by increased fragmentation at the higher pulse energy.

Herbani et al. [201] reported the first synthesis of a ternary alloy achieved with LRL. They synthesized Au-Pt-Ag solid-solution alloys, without any phase segregation, by irradiating aqueous solutions of $HAuCl_4$, H_2PtCl_6 and $AgNO_3$ precursors with PVP as the capping agent and ammonia as the complexing agent. As explained in sect. 4.1.2, ammonia and silver ions generate a silver-ammonia complex, which promotes the production of AgNPs while simultaneously obstructing the creation of unwanted AgCl. In preliminary experiments, the addition of ammonia caused the nanoparticles to be aggregate, which is what inspired the addition of PVP as a capping agent. In the UV-vis absorbance spectra of the platinum-containing alloys, no SPR peaks were identified, confirming the acquisition of solid-solution alloys without phase-segregation [280]. Only a small peak at 464 nm was observed for the ternary alloy with low platinum concentration (10%). Nanoparticle diameters were comparable across alloy compositions, averaging ~5 nm. The alloy compositions were similar to their feed-ratios, suggesting that composition is tunable even for ternary alloys using the LRL method.

Sarker and co-workers have published several papers using the LRL approach to synthesize bimetallic and ternary alloys involving rhodium, platinum, and palladium. In 2013 they produced homogeneous Rh-Pd and Rh-Pt alloys in an aqueous medium without any capping agents [276]. For both Rh-Pd and Rh-Pt alloys, nanoparticle diameter decreased with the concentration of rhodium, which is consistent with previous results found through wet chemical synthesis [281]. Despite the differences in redox potentials between rhodium, palladium, and platinum, homogeneous alloys with no phase segregation were formed, which was attributed to the interdiffusion of elements following precursor reduction. Without capping agents, these nanoparticles were not stable for prolonged periods of time. The authors subsequently mixed all three metal precursors and synthesized composition-tunable, homogeneous, ternary Rh-Pt-Pd alloys under similar reaction conditions [277]. Again, nanoparticle diameter decreased

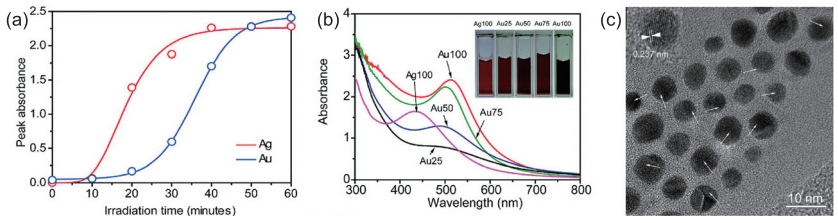

Figure 25 (Color online) Surface plasmon resonance absorbance as a function of irradiation time, for silver (red) and gold (blue) (a); final UV-vis spectra showing single SPR peaks (b); and high resolution TEM image of Au75 with uniform lattice fringes (c). Adapted from ref. [198], copyright 2011 American Chemical Society.

proportionally with rhodium present in the particle. The different compositions displayed varying stabilities, which the authors attributed to the alloys' zeta-potentials. The alloy with the highest rhodium content had the lowest zeta-potential and precipitated first, followed sequentially by the next largest rhodium proportion.

To increase the stability of these ternary alloys, the same authors employed both PVP and citrate as capping agents, examining the effects each induced in the alloy nanoparticles products [242, 278]. As expected, PVP produced smaller nanoparticles across all compositions. But, it produced platinum-rich alloys independently of precursor ratios. Citrate yielded larger nanoparticles, but the compositions paralleled the precursor ratios. The authors attributed these findings to citrate's comparably weaker capping ability. The standard reduction potentials of Pt^{2+}, Pd^{2+}, and Rh^{3+} (versus SHE) vary in the following order: $Pt^{2+} \rightarrow Pt^0$ (+1.20 V); $Pd^{2+} \rightarrow Pd^0$ (+0.915 V); $Rh^{3+} \rightarrow Rh^0$ (+0.8 V). Beyond being reduced by laser-produced transient species, Pt^{2+} will also be simultaneously reduced, at the expense of Pd^0 and Rh^0, through galvanic replacement (eq. (26) in sect. 5.2.3), decreasing the number of available rhodium and palladium atoms. Unreacted metallic ions can bind with PVP, allowing a replacement reaction to occur between the nanoparticles and these metallic ions. Furthermore, PVP impedes nuclei surfaces during the early stages of nanoparticle formation, preventing interactions with other atoms, resulting in platinum-rich alloys. Citrates, on the other hand, allow for metal-atom interdiffusion due to their weak capping effect, forming solid-solution alloys with elemental composition proportional to that of the precursors (Figure 26(a)). These synthesized particles were loaded onto alumina support and then heated to 1000°C to make the alloys heterogeneous, which accomplished enhanced catalytic activity for CO oxidation [242]. Nakamura and co-workers reported the production of Pd-Pt alloy nanoparticles [274] as well as a high-entropy alloy of rhodium, palladium, iridium, gold, and platinum in aqueous solution without capping agents [275] (Figure 26(b)).

In contrast to homogeneous alloy nanoparticles, Nishi et al. [257] synthesized Ir-Au core-shell nanoparticles (Figure 26(c)). The creation of this nanostructure was attributed to the excitation probabilities of $HAuCl_4$ and H_2IrCl_6 precursors using 800 nm femtosecond laser pulses. Direct, multiphoton photolysis of $AuCl_4^-$ has been proposed to contribute to nanoparticle production [77]. Multiphoton photolysis of $AuCl_4^-$ requires three photons, whereas $IrCl_6^{2-}$ requires only two; increasing the probability of iridium atoms being produced by direct multiphoton photolysis. The reactions between reactive water species like hydrated electrons and $IrCl_6^{2-}$ and $AuCl_4^-$ ions should occupy longer timescales. That projected time-lag would result in the creation of an iridium core (due to rapid photolysis), followed by the reduction of $AuCl_4^-$ and the remaining $IrCl_6^{2-}$ (due to the slower reactions of hydrated electrons) to create an iridium core and a gold-rich shell. This hypothesis not only helps to explain core-shell formation, but it also offers a plausible explanation for the larger nanoparticle sizes observed for Ir@Au alloys when compared to monometallic Ir- and AuNPs.

While the majority of LRL alloy syntheses involve noble metals, there have been some examples pairing non-noble metals with nanosecond laser pulses [282, 283]. Hayasaki et al. [260, 282] coupled the ferrocene and cobaltocene precursors to synthesize FeCo and $CoFe_2O_4$ alloys, expanding

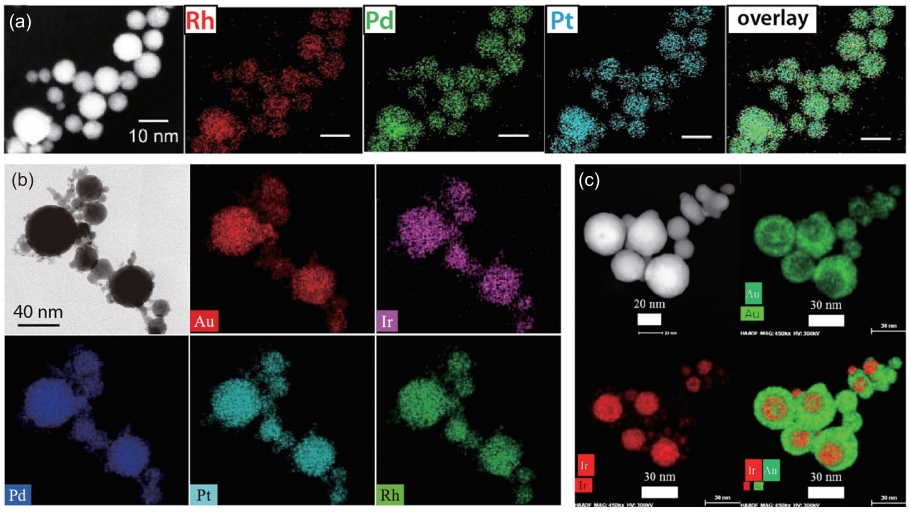

Figure 26 (Color online) STEM-EDX mapping of homogenous Pt-Pd-Rh alloy nanoparticles (a); homogenous Au-Pd-Pt-Ir-Rh alloy nanoparticles (b); and Ir-Au core-shell nanoparticles (c). Adapted from ref. [242] (a), CC-BY-3.0; ref. [275] (b), CC-BY-3.0; and ref. [257] (c), copyright 2018 with permission from Elsevier.

on their previously mentioned work (sect. 4.2) regarding the synthesis of Fe- and CoNPs from ferrocene and cobaltocene in benzene. The initial amorphous nanoparticles became crystalline after annealing, producing FeCo and $CoFe_2O_4$ nanoparticles covered with carbon layers. The production of $CoFe_2O_4$ was attributed to dissolved oxygen in the solvent. Torres-Mendieta et al. [283] synthesized Fe-Cu oxide alloy nanoparticles by irradiating metal chloride solutions in acetone, water, and ethylene glycol with focused, nanosecond pulsed laser irradiation. Peak laser intensities were above the breakdown thresholds for water and ethylene glycol, resulting in the formation of solvated electrons and hydrogen radicals. Acetone, on the other hand, undergoes 2-photon absorption, followed by hydrogen-abstraction from hydrated metal salts to produce the comparatively weaker reducing ketyl species [284, 285]. The distinct reducing species generated within each solvent were used to explain the eventual product compositions. Preferential CuO nanoparticle formation in acetone was credited to the reduction of copper salts by ketyl radicals, due to the significantly higher reduction potential of copper ions over iron ions (0.34 V versus −0.41 V_{SHE}). This was followed by the capping of copper species with acetone, preventing them from mixing with iron species. In the case of both water and ethylene glycol, strongly-reducing laser transients may co-reduce the metal ions. The subsequent coalescence of copper and iron atoms into particles and the tendency of both atoms to react with dissolved oxygen creates nanostructures comprising copper, iron, and oxygen; eventually leading to the formation of Fe-Cu oxides. Furthermore, although all three solvents predominantly created nanoparticles ~5 nm in size, samples synthesized in acetone had additional size distribution around 35 nm, and ethylene glycol samples produced size distributions around 35 and 75 nm.

5 Reactive laser ablation and fragmentation of solid or colloid targets in the presence of molecular precursors

We discussed in sect. 3 how LAL and LFL procedures are often inherently reactive because of metal oxidation, reduction, and carbon-incorporation into the nanoparticles produced. In this section, we will examine RLAL and RLFL, which still refer to the ablation and fragmentation of a solid or colloid target respectively, but with the inclusion of, often metal, precursors. Precursors are distinct from targets in the format: they are typically salts or complexes and exist in molecular or ionic form, whereas targets are solid or colloidal materials. The addition of metal precursors to LAL or LFL processes opens up additional reaction pathways to the reactive species generated in the laser-plasma, hence the addition of the term reactive. This section summarizes several studies that used RLAL or RLFL to create products like supported MNPs (sect. 5.1), multimetallic nanoparticles (sect. 5.2), structured nanomaterials (sect. 5.3), and metal nanostructures on solid surfaces (sect. 5.4). The reaction mechanisms leading to each of these products are discussed where available; although in many cases the formation pathways are unknown because of their complexity.

5.1 Supported metal nanoparticles

Both RLAL and RLFL are used to produce MNPs supported on metal or semiconductor oxides [286-294] and carbonaceous supports [72, 294-305]. Tabulated summaries of these and other syntheses are given in ref. [31]. Oxide supports are beneficial because of strong metal-support interactions at metal-oxide interfaces, which improve catalytic activity significantly [292, 294]. Carbon supports like graphene oxide (GO) are often used for MNP deposition in RLFL because they can be applied to nonlinear absorption [296, 297], photothermal conversion [298, 301], photovoltaics [299], and catalysis [72, 295, 300-305]. Please note that in this section, we will use the term "RLFL" to refer to laser-irradiation of any powdered support materials, so as to distinguish it from RLAL with solid targets. These powder supports are not, however, always fragmented during the synthesis.

Silica is an enticing support material for MNPs because it has high thermal stability [286, 287]. Saraeva et al. [286] reported that ablating a silica wafer submerged in aqueous solutions containing $HAuCl_4$ or $AgNO_3$ with 1040 nm nanosecond pulses produced spherical 10-30 nm Au- or AgONPs (depending on the precursor metal), and large ~100 nm silica particles decorated with either Au- or AgNPs (Figure 27(a), (b)). Because such a low intensity (10^9 W cm^{-2}) was used in their experiments, no Au- or AgNPs were produced without the silicon target. The authors concluded that laser interaction with the solid silicon was necessary to produce sufficient reactive species to reduce the metal ions. John and Tibbetts [287] ablated a silicon wafer in aqueous $KAuCl_4$ adjusted to pH 10 using 800 nm, 30 fs pulses, which also produced two products: isolated 7 nm AuNPs, and sub-3 nm AuNPs stabilized by an amorphous silica matrix (Figure 27(c), (d)). The formation of isolated AuNPs was attributed to $[AuCl_4]^-$ reduction, via the electron-mediated solution processes discussed in sect. 4.1. Smaller AuNPs in the silica matrix likely coalesced through reactions between the ejected silicon atoms and liquid droplets with remaining $[AuCl_4]^-$ and gold nuclei that had not yet grown large enough to isolate as stable AuNPs. The authors hypothesized that the smaller size of the supported AuNPs was due to either low concentra-

tions of gold around the surface of the silicon, or to the quenching of AuNP growth on account of their encapsulation within the silica matrix. Moreover, the smaller size of the supported AuNPs generated using femtosecond-RLAL was likely caused by faster cooling due to the ultrashort pulse duration, as discussed previously.

Lin et al. [288] produced Au-, Ag-, and PtNPs on TiO_2 and Fe_2O_3 supports through RLAL of titanium and iron targets immersed in $HAuCl_4$, $AgNO_3$, and Na_2PtCl_6 solutions, using 1064 nm millisecond laser pulses. Their experiment produced MNPs on thermally-stable anatase TiO_2 (Figure 28(a), (b)) and γ-Fe_2O_3 (Figure 28(c), (d)) support phases. Because of the extremely long pulse duration (1.2 ms) and low intensity (10^7 W cm^{-2}), no plasma formed. Instead, the solid target was heated to the liquid state, forming metal droplets that were further heated above the boiling point until they exploded: shattering into nanodroplets. Nanodroplets react with oxygen atoms to form oxide nanoparticles, and with metal atoms in a solution that aggregate into MNPs that deposit onto the oxide surfaces. Because the target is heated to such high temperatures, thermal decomposition of $[AuCl_4]^-$ and other precursors likely contributes to initial metal atom reduction, as was observed using nanosecond laser pulses in the absence of supports [71] (cf. sect. 4.1.1). Notably, titanium ablation in $AgNO_3$ solutions using femtosecond pulses produced AgNPs on titania support nanoparticles consisting of the partially reduced $TiO_{1.04}$ and Ti_2O_3 phases [289], instead of anatase TiO_2. This was attributed to the rapid quenching of oxidizing species by the ultrashort pulse duration.

Oxide-supported MNPs have also been produced by several groups through RLFL, with a favored oxide powder being TiO_2 [290-293]. Zeng et al. [290] synthesized Ag-TiO_2 nanocomposites from mixed $AgNO_3$ and TiO_2 nanoparticle solutions in water-ethanol mixtures, with added NH_3, using 800 nm femtosecond pulses. Because no AgNPs were observed in the absence of TiO_2 powder, the authors proposed that excitation of the TiO_2 electrons to the conduction band by the femtosecond laser pulses is what generated the electrons necessary to reduce the Ag^+ that was adsorbed onto the negatively-charged TiO_2 particles in the high-pH solution environment [290]. Mintcheva et al. [291] deposited 10 nm AuNPs on commercial, anatase TiO_2 with a two-step process. First, they did LFL of an initial powder using 1064 nm, 1 ms pulses; then, RLFL with the addition of an $NaAuCl_4$ solution, under the same conditions. The authors attributed AuNP deposition to Au^{3+} reduction on surface Ti^{3+} species, achieved with associated oxygen-vacancies acquired during the LFL step. Das et al. [292] synthesized TiO_2, ZrO_2, ZnO, and SiO_2 powders via gas-phase laser ablation, and followed each synthesis with RLFL in dissolved K_2PdCl_4 water-ethanol mixtures. They produced supported PdNPs for use as Suzuki cross-coupling catalysts. Gurbatov et al. [293] created amorphous TiO_2 nanospheres decorated with AuNPs by performing RLFL on commercially available TiO_2 nanopowder dispersed in aqueous $HAuCl_4$ with 532 nm nanosecond laser pulses (Figure 29(a), (b)). To explain the facile deposition of AuNPs onto TiO_2, and the associated melting of the initial TiO_2 powder, they modeled laser-induced heating of TiO_2 in both the absence and presence of an attached AuNP (Fig-

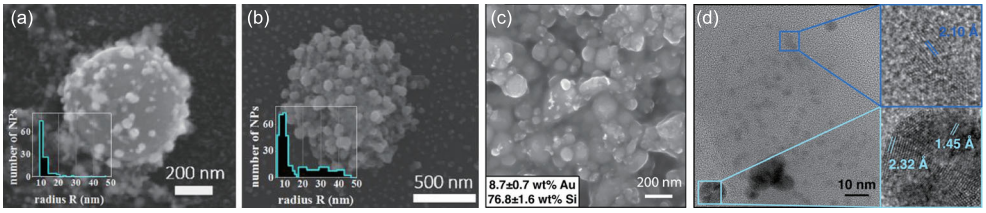

Figure 27 (Color online) SEM images of Au-SiO_2 (a), and Ag-SiO_2 nanocomposites (b); SEM image (c) and high resolution TEM with lattice spacings (d) for Au-SiO_2 nanocomposites. Adapted from ref. [286] (a), (b) copyright 2018, with permission from Elsevier; and ref. [287] (c), (d) copyright, 2019 with permission from Elsevier.

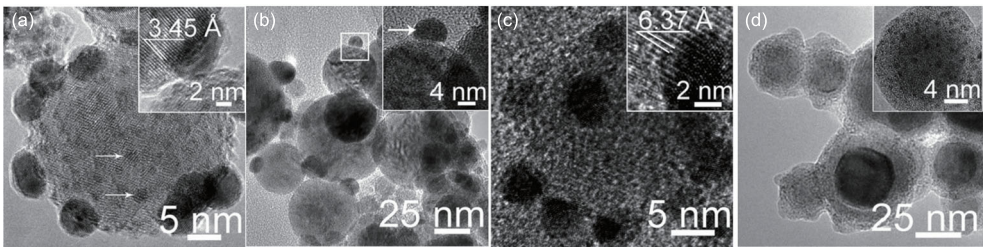

Figure 28 TEM images of AuNPs on TiO_2 (a), AgNPs on TiO_2 (b), AuNPs on Fe_2O_3 (c), and PtNPs on Fe_2O_3 (d). Adapted from ref. [288], with permission from the Royal Society of Chemistry.

ure 29(c)). The extensive photothermal heating induced by the attached AuNP due to its surface plasmon absorbance resulted in transient temperatures exceeding 1900 K; sufficient to melt the TiO_2 and induce the observed structural changes.

Metal nanoparticles can also be deposited onto carbonaceous supports using RLFL. Bobb et al. [294] synthesized porous, N-doped carbonaceous TiO_2 support by gas-phase laser ablation of the pre-synthesized metal organic framework (MOF) NH_2-MIL-125(Ti). They then introduced PdNPs through RLFL in a water-ethanol solution of K_2PdCl_4 with 532 nm nanosecond pulses. The Pd^{2+} reduction was accompanied by oxidative etching of the N-doped carbon spheres. Hollow structures were formed for the encapsulation of PdNPs, resulting in hierarchical meso- and microporous supported PdNPs (Figure 30(a)). Lv et al. [295] used a two-step process involving deposition of PdO onto carbon nanotubes via spontaneous hydrolysis of Na_2PdCl_4 on the carbon nanotube surfaces, followed by irradiation with

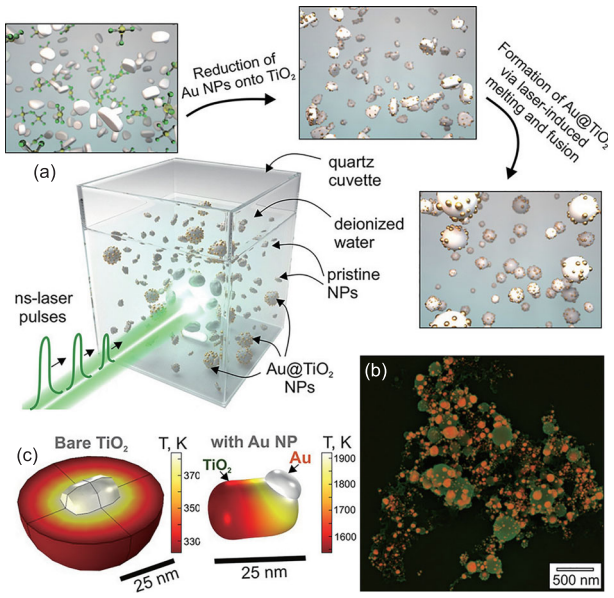

Figure 29 (Color online) Representation of Au-TiO_2 nanocomposite fabrication using nanosecond pulses (a); false-color SEM image of Au-TiO_2 (b); calculated temperature profile in the vicinity of a bare and a gold-decorated TiO_2 nanoparticle, upon irradiation with a single nanosecond laser pulse (c). Reproduced from ref. [293] copyright 2021, American Chemical Society.

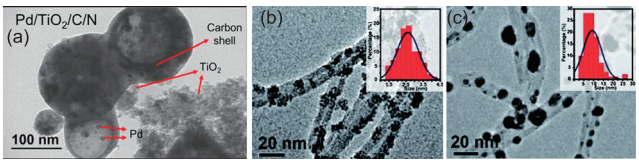

Figure 30 (Color online) TEM images of supported PdNPs encapsulated in N-doped carbonaceous TiO_2 (a), and Pd-PdO nanoparticles supported on carbon nanotubes after irradiation for 10 min (b) and 120 min (c). Adapted from ref. [294] (a) copyright 2019, American Chemical Society; and ref. [295] (b), (c) with permission from the Royal Society of Chemistry.

unfocused 355 nm nanosecond laser pulses to partially reduce the palladium. Irradiation for 10 min (Figure 30(b)) partially reduced the PdO and resulted in average particle size of ~2.5 nm, whereas longer irradiation, for 120 min (Figure 30(c)), fully reduced the PdO and produced larger ~10 nm PdNPs.

Graphene oxide is one of the most widely used supports in RLFL syntheses [72, 296-305]. Reaction parameters, including laser irradiation time [296, 298, 299], fluence [299, 304], pulse duration [72], metal precursor concentration [296, 299, 303], and additives or nonaqueous solvents [300, 302, 303], can control the properties of the resulting MNP-GO composite materials. Yu et al. [296] found that longer irradiation times with femtosecond pulses increased the fraction of $AgNO_3$ precursor deposited as AgNPs, and partially reduced oxygen functional groups on the GO (producing partially reduced graphene oxide, prGO). However, longer irradiation times resulted in excessive fragmentation of the GO, and larger AgNPs (Figure 31(a)-(c)). Bobb et al. [72] directly compared Au-prGO nanocomposites produced by RLFL of GO in aqueous $KAuCl_4$ using nano- and femtosecond laser pulses. A broad distribution of AuNPs centered at ~5 nm was observed when a nanosecond laser was used (Figure 31(d)). When a femtosecond laser was used, two distinct distributions centered around 3 and 10 nm were observed instead (Figure 31(e)). Anisotropic AuNPs can

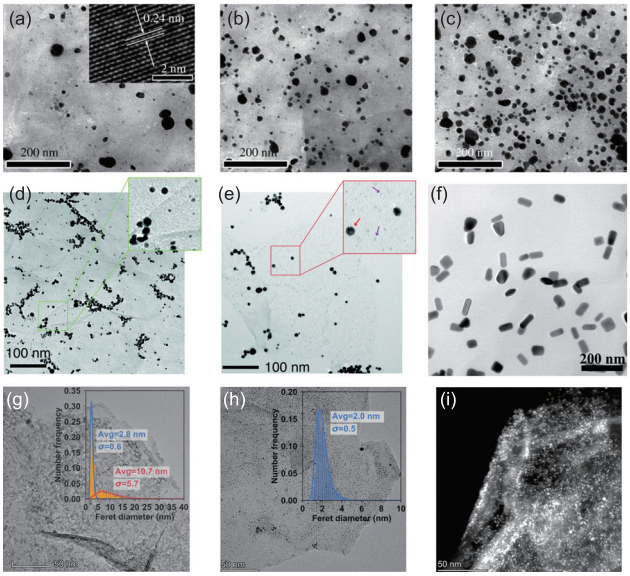

Figure 31 (Color online) TEM images of Ag-GO prepared by irradiation with nanosecond pulses for 10 min (a), 20 min (b), and 30 min (c); Au-GO synthesized with nanosecond (d) and femtosecond pulses (e); gold nanorods on GO (f); RuO_2-EGO (g) and Pt-EGO (h) along with STEM-HAADF image (i). Adapted from ref. [296] (a)-(c), CC-BY-3.0; ref. [72] (d)-(e) with permission from the Royal Society of Chemistry; ref. [298] (f) copyright 2019, with permission from Elsevier; and ref. [304] (g)-(i) copyright 2020 Wiley-VCH.

also be deposited by RLFL of GO in aqueous $HAuCl_4$, with added hexadecyl trimethyl ammonium bromide and $AgNO_3$ as growth-directing agents [298]. After 1 min of irradiation with 800 nm, 100 fs pulses to produce gold seeds, the solution was maintained at 30°C for 3 h to allow nanorods to grow on the GO (Figure 31(f)). Peng et al. [304,305] used electrochemically synthesized GO (EGO) to deposit sub-3 nm RuO_2 (Figure 31(g)) and platinum (Figure 31(h), (i)) by irradiating with 248 nm nanosecond pulses. Compared with the conventional chemical GO produced by Hummers' method, EGO has a lower oxygen content and a less disrupted honeycomb lattice structure, which facilitates reduction to graphene during laser irradiation. The same group deposited single platinum atoms onto graphene by freeze-drying and sublimating EGO infused with H_2PtCl_6 precursor before laser irradiation [305].

The facile deposition of MNPs onto GO via RLFL was attributed to photoexcitation of GO [72, 300, 301, 304]. Graphene oxide behaves as a semiconductor, with tunable bandgap values that vary depending on the frequency and type of oxygen functional groups [304]. Photoexcitation creates electron-hole pairs. The resulting electrons reduce adsorbed metal ions to form nuclei that then grow on the GO substrate [72, 300, 301, 304]. This action of GO has been invoked to explain the observed acceleration of $KAuCl_4$ reduction using both nanosecond and femtosecond lasers in the presence of GO, in contrast to slower LRL reduction of aqueous $KAuCl_4$ without GO [72]. Moreover, the addition of hole scavengers like ethanol, isopropanol, and PEG, further accelerates metal ion reduction onto GO by inhibiting electron-hole recombination [301,302,304]. In addition to depositing MNPs onto GO, the RLFL process results in the reduction of oxygen functional groups, partially or fully reducing GO [72,298,300-302]. This reduction of GO is attributed to photothermal effects when nanosecond pulses are used; as they have durations that are longer than the electron-lattice coupling timescales of picoseconds [72,302]. When femtosecond pulses are used, GO reduction can proceed from interaction with the reactive species generated in the plasma [72].

5.2 Multimetallic nanoparticles

Multimetallic nanoparticles are incredibly versatile, with myriad avenues for tailoring. Synthesis of these diverse nanoparticles has been achieved using both RLAL and RLFL, producing core-shell nanoparticles [306-315], doped metal and metal-oxide nanoparticles [316-319], bimetallic and trimetallic alloy nanoparticles [219,320-327], and metal sulfide semiconductors [328-331]. This section will discuss literature from each of these nanoparticle classes.

5.2.1 *Core-shell nanoparticles*

Ablation of a silicon wafer in solutions of noble metal precursors can produce a variety of metal-silica "core@shell" nanoparticles. Properties of the resulting nanoparticles will depend on the metal precursor concentration, the laser irradiation conditions, and whether the precursors are added to solution during or after the silicon is ablated (Figure 32) [306-310]. Direct RLAL in $HAuCl_4$ and $AgNO_3$ solutions with 355 nm nanosecond laser pulses produces ~10 nm $Ag@SiO_2$ or $Au\text{-}Ag@SiO_2$, with thin SiO_2 shells (Figure 32(a)) when the total precursor concentration is 0.125 mM [306]. Large (~100 nm) $SiO_2@Au$ nanoparticles, with various gold shell structures, are formed when the precursor concentration is 2.5 mM and a second 532 nm laser is loosely focused above the silicon–solution interface (Figure 32(b)) [307]. The distinctly larger nanoparticle sizes and inversion of the core and shell components when a high-concentration metal precursor and a second 532 nm laser are used, are likely due to the acceleration of silicon melting, induced by the addition of the second laser. Similar particle morphologies with metal nanoparticles blanketing the SiO_2 cores were produced using 1040 nm nanosecond pulses [286] (cf. sect. 5.1, Figure 27). Ablation of silicon in water or ethanol, followed by addition of metal precursors after irradiation is terminated, has produced $Au@SiO_2$ (Figure 32(c)) [308], $Ag@SiO_2$ (Figure 32(d)) [309], and $Au\text{-}Ag@SiO_2$ (Figure 32(e)) [310]; all with relatively thick SiO_2 shell structures. Ablated-silicon's ability to reduce metal precursors in solution, with no further laser irradiation, can be attributed to the higher oxidation-potential of nanostructured silicon as compared to bulk silicon ($Si \rightarrow Si^{4+} + 4e^-$, −0.84 V). This swings net-favorability to the redox processes, involving $AuCl_4^- + 3e^- \rightarrow Au^0 + 4Cl^-$ (+1.002 V) or $Ag^+ + e^- \rightarrow Ag^0$ (+0.800 V) coupled to silicon oxidation [308].

Additional core-shell noble-MNPs, with various oxide shells, have been produced with RLAL using 1064 nm nanosecond lasers [311-315]. Mostafa et al. [311,312] synthesized Au@ZnO (Figure 33(a)) and Au@CdO by RLAL of zinc and cadmium powders in aqueous $HAuCl_4$. The reduction of $HAuCl_4$ likely proceeds by the same plasma reactions discussed in sects. 2.1 and 4.1.1, in conjunction with the oxidation of ablated zinc and cadmium species, forming the oxide shell structures, paralleling the silicon redox reactions discussed before. Similar core-shell structures can form by RLAL of solid noble metal targets in solutions of oxide-shell precursors (Figure 33(b)-(l)). Sheykhifard et al. [313] ablated a gold target in acidic solutions with varying concentrations of $PdCl_2$. Low $PdCl_2$ concentrations manifested Au@PdO nanoparticles (Figure 33(b)), whereas high $PdCl_2$ concentrations produced thicker $PdCl_2$ shells and net-

works of Au/$PdCl_2$ core-shell structures (Figures 33(c), (d)). Bao et al. [314, 315] generated a trove of metal@oxide nanoparticles by ablating various metal targets in aqueous solutions of the metal oxide precursor: $SnCl_4$ to produce Au@SnO_2 (Figure 33(e)); $TiCl_4$ to produce Au@TiO_2 (Figure 33(f)), Pt@TiO_2 (Figure 33(j)), and Pd@TiO_2 (Figure 33(k)); $Zn(NO_3)_2$ to produce Au@ZnO (Figure 33(g)); $FeCl_3$ to produce Au@Fe_2O_3 (Figure 33(h)); $KAlSO_4$ to produce Au@Al_2O_3 (Figure 33(i)); and $Cu(OAc)_2$ to produce Au@CuO (Figure 33(j)). The authors attributed oxide-shell formation to hydrolysis of the precursor salt. Hydrolysis was followed by electrostatic attraction of the resulting metal hydroxides to the surfaces of the MNPs that emerged from the ablated surface, to produce hydroxide shells. Finally, dehydration yielded the oxide shells [315]. Interestingly, the complementary strategies of ablating zinc in $HAuCl_4$, and ablating gold in $Zn(NO_3)_2$, produced similar Au@ZnO nanoparticles (compare Figure 33(a), (g)), despite the different mechanisms involved.

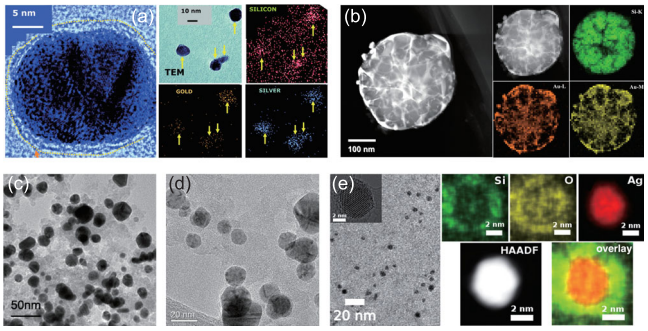

Figure 32 (Color online) Metal-silica core-shell nanoparticles: Au-Ag@SiO_2 (a), and SiO_2@Au (b) synthesized by RLAL of silicon in metal precursor solution; Au@SiO_2 (c), Ag@SiO_2 (d), and Au-Ag@SiO_2 (e) synthesized by LAL of silicon in water and the subsequent addition of metal precursor. Adapted from ref. [306] (a) copyright 2010, American Chemical Society; ref. [307] (b) copyright 2015, American Chemical Society; ref. [308] (c) copyright 2009, American Chemical Society; ref. [309] (d) copyright 2015, Springer Nature; and ref. [310] (e) copyright 2017, American Chemical Society.

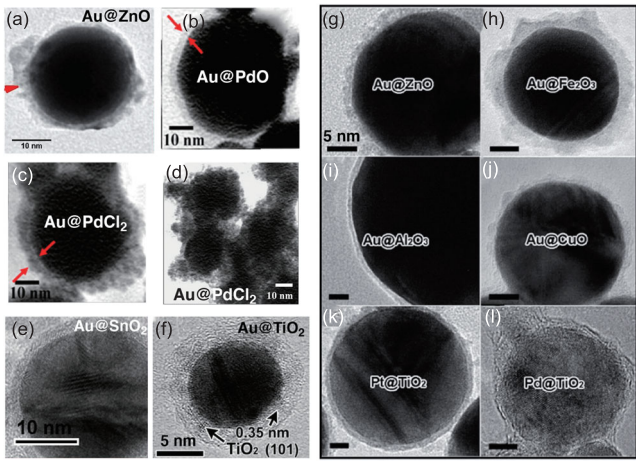

Figure 33 (Color online) Metal-oxide core-shell nanoparticles from RLAL: Au@ZnO (a), Au@PdO (b), Au@$PdCl_2$ ((c), (d)), Au@SnO_2 (e), Au@TiO_2 (f), Au@ZnO (g), Au@Fe_2O_3 (h), Au@Al_2O_3 (i), Au@CuO (j), Pt@TiO_2 (k), and Pd@TiO_2 (l). Adapted from ref. [311] (a) copyright 2020, with permission from Elsevier; ref. [313] (b)-(d) copyright 2015, American Chemical Society; ref. [314] (e) copyright 2017, with permission from Elseiver; and ref. [315] (f)-(l) copyright 2017, American Chemical Society.

5.2.2 *Nanoparticle doping*

RLAL of metal or oxide targets in metal precursor solutions at low concentrations ($\leq$ 1 mM) has been used to dope metal atoms into nanoparticles. Chemin et al. [316] ablated a Gd_2O_3 target in 0.01-1 mM aqueous solutions of $EuCl_3$, and produced 1 atom% Eu-doped Gd_2O_3 with strong photoluminescence in the visible region. The Du group [317-319] synthesized a series of MNPs with single-atom doped sites for electrocatalysis applications. Ablating a ruthenium target in acidic solutions of $HAuCl_4$ generated single-gold-atom-doped RuNPs (Figure 34) [317]. The presence of exclusively isolated gold atoms in the ruthenium lattice for a 0.2 mM $HAuCl_4$ concentration was confirmed with HAADF-STEM imaging, showing the brighter gold atoms in red circles (Figure 34(c)) and Fourier-transformed EXAFS measurements showing the presence of Au-Ru and Ru-Ru bonds, but not Au-Au bonds (Figure 34(d), (e)). The authors found that isolated gold atoms were only formed when the $HAuCl_4$ concentration was 0.2 mM or lower, with an associated upper-limit of 15.35 atom% gold-doping. They obtained similar results when ablating ruthenium in dilute, aqueous solutions of $NiCl_2$: isolated, oxidized nickel atoms were present when the $NiCl_2$ concentration was 0.2 mM or lower, with a nickel content of 0.29 atom%. Discrete NiO phases were formed at higher $NiCl_2$ concentrations [318]. The same authors found

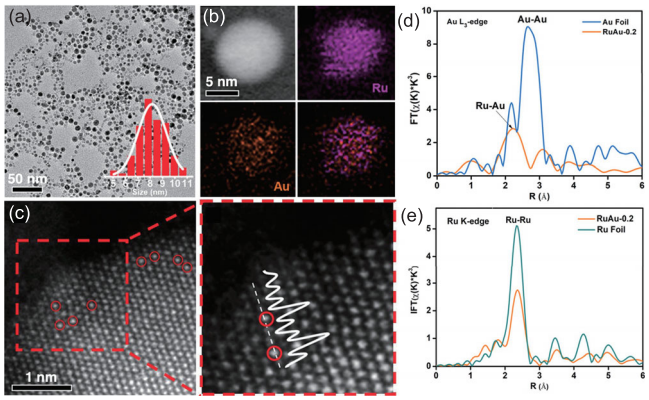

Figure 34 (Color online) Single gold-atom doped RuNPs (a) with STEM-EDX elemental mapping (b), HAADF-STEM imaging (c), and Fourier-transformed EXAFS spectra of the gold (d) and ruthenium (e) regions. Adapted from ref. [317] copyright 2019, Wiley-VCH.

that ablating iridium in $AgNO_3$ solutions, with concentrations up to 1 mM, produced single silver atoms in the ruthenium lattice, with 6.5 atom% silver, whereas higher $AgNO_3$ concentrations formed Ag-Ir alloys [319]. Collectively, these studies demonstrate that limiting the concentration of metal precursors in the solution can effectively dope single, isolated atoms into MNPs consisting of mostly the ablated metal target.

5.2.3 *Composite and alloy nanoparticles*

Conducting RLAL in more concentrated precursor solutions has been known to produce metal alloy phases ever since Poondi et al. [320] and Liu et al. [219] reported the alloying of immiscible nickel and silver in the early 2000s, by performing RLAL of nickel in $AgNO_3$ solution. Between then and now, many groups have synthesized alloy nanoparticles using RLAL [321-327]. Some control over the compositions of alloy nanoparticles has even been achieved, by varying the laser parameters and solution reaction conditions [325, 327].

Yoon et al. [321] ablated gold and silver targets in aqueous 1 mM Na_2PdCl_4, with both nano- and femtosecond laser pulses. Flower-like, heterogeneous Au-Pd and Ag-Pd nanostructures, comprising aggregates of smaller nanoparticles were produced in both cases. Smaller structures formed under nanosecond pulses (Figure 35(a)) than femtosecond pulses (Figure 35(b)). Despite similar particle morphologies, the compositions of the two sets of Au-Pd and Ag-Pd nanoflowers were drastically different: nanosecond pulses produced 2:1 Au:Pd and 1:1 Ag:Pd weight ratios; but femtosecond pulses produced 1:4 Au:Pd and 1:5 Ag:Pd weight ratios [321]. This elevated incorporation of palladium into the Au-Pd and Ag-Pd structures caused by the femtosecond laser pulses is likely due to the greater contribution of the laser-induced chemical reactions discussed in sects. 2.1 and 4.1, which reduce Pd^{2+}. Notably, the flower-like aggregates of ~5 nm nanoparticles resemble the PdNPs that the Tibbetts group synthesized by LRL (cf. Figure 19(a), (b)), suggesting that Pd^{2+} reduction under both femto- and nanosecond laser irradiation preferentially forms anisotropic structures of agglomerated PdNPs.

In contrast to the heterogeneous Au-Pd and Ag-Pd structures discussed above, many RLAL syntheses produce bimetallic or trimetallic particles with uniform elemental distributions. Park et al. [322] ablated a palladium target in aqueous 1 mM $CuCl_2$, creating spherical Pd-Cu nanoparticles with uniform elemental distribution. Separate palladium and copper domains within individual nanoparticles were only observed with high resolution TEM lattice-fringe analysis (Figure 35(c)). Yu et al. [323] synthesized Pd-Ni nanoparticles using a two-step process. First, a nickel target was ablated in methanol. Then, the resulting solution of NiNPs in $PdCl_2$ was irradiated with low-fluence, 532 nm nanosecond pulses in an ultrasonic bath. The resulting Pd-Ni nanospheres exhibited homogeneous distribution of palladium and nickel atoms (Figure 35(d)), along with alloyed Pd-Ni phase identified by XRD. Mostafa et al. [324] synthesized Au-Ag alloy nanoparticles by ablating a silver target in aqueous $HAuCl_4$, and generating a uniform Au-Ag alloy composition, identified by XRD. The alloyed particles exhibited a single SPR peak in the absorbance spectrum. The achievement of homogeneous, Au-Ag alloy nanoparticles via RLAL matches the results from both LRL of mixed gold and silver precursor solutions (cf. sect. 4.3), and LFL of solutions containing LAL-synthesized Au- and AgNPs [218]. Creating uniform Au-Ag alloy nanoparticles across all of these laser-synthesis techniques is possible because of the facile alloying of gold and silver as a pair, which can be credited to their similar lattice parameters.

To control the compositions of bimetallic and trimetallic alloy nanoparticles with RLAL, the Mukherjee group [325-327] conducted extensive investigations in which they varied parameters such as laser fluence, irradiation time, solution pH, and the concentration of metal precursors in solution. In their first study [325], they ablated a cobalt target in solutions of K_2PtCl_4, adding HCl or KOH to control the pH, and produced homogeneous Pt-Co alloy nanoparticles (Figure 36(a)). The Pt:Co ratio and degree of alloying in the final Pt-Co products were tailorable through solution pH and K_2PtCl_4 concentration (Figure 36(b)). The authors proposed that the Pt^{2+} ions were primarily reduced through the galvanic replacement reaction,

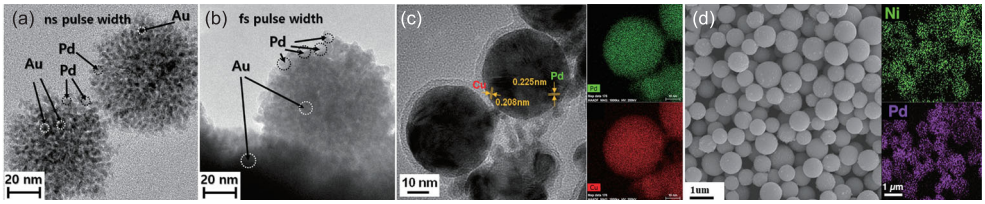

Figure 35 (Color online) Bimetallic nanoparticles synthesized by RLAL: Au-Pd nanostructures synthesized using nanosecond (a) and femtosecond (b) laser pulses; Pd-Cu nanoparticles (c); Pd-Ni nanoparticles (d). Adapted from ref. [321] (a), (b), CC-BY-3.0; ref. [322] (c) copyright 2017, with permission from Elsevier; and ref. [323] (d) copyright 2021, with permission from Elsevier.

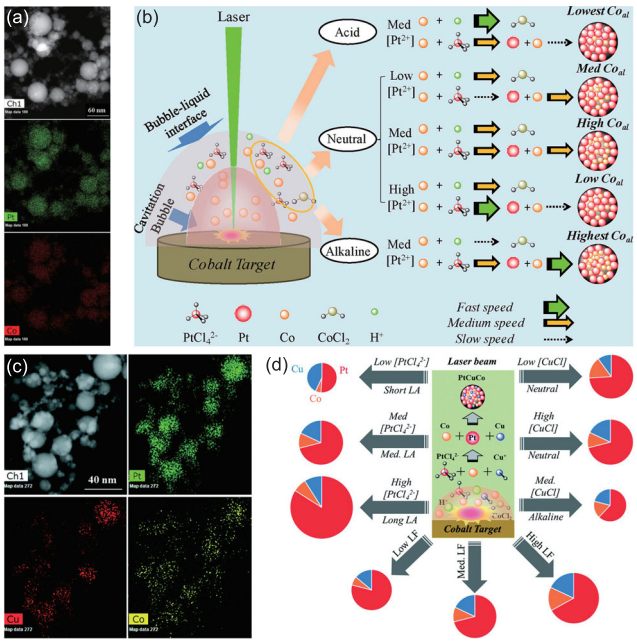

Figure 36 (Color online) STEM-EDX mapping ((a), (c)) and diagrams of reaction parameters ((b), (d)) for synthesis of Pt-Co ((a), (b)) and Pt-Co-Cu ((c), (d)) alloy nanoparticles. Adapted from ref. [325] (a), (b) copyright 2016, with permission from Elsevier; and ref. [327] (c), (d) with permission from the Royal Society of Chemistry.

$$Pt^{2+} + Co \longrightarrow Pt + Co^{2+} \tag{26}$$

due to the high reduction potential of platinum relative to cobalt [325]. Plasma electrons likely also contribute to Pt^{2+} reduction, as discussed in sect. 2.1. The observed dependence of the Pt-Co composition on K_2PtCl_4 concentration and pH indicates that both the galvanic replacement reaction, eq. (26), and plasma electrons affect the final product outcome. Under acidic conditions, ablated cobalt was rapidly oxidized to Co^{2+} via the reaction

$$Co + 2H^+ \longrightarrow Co^{2+} + H_2, \tag{27}$$

which leaves very few metallic cobalt species available for galvanic replacement (eq. (26)). The resultant high platinum content, with little alloying, is consistent with the proposed rapid cobalt-oxidation by eq. (27) and suggests that platinum is mostly reduced by electrons from the plasma in these conditions. At neutral pH, the K_2PtCl_4 concentration determines the relative rates of reactions (26) and (27), with to the most efficient alloying at moderate K_2PtCl_4 concentrations. When the rate of reaction (26) is limited by platinum availability, neutral cobalt species are allowed to alloy with reduced platinum species to form a balanced ratio. Under basic conditions, reaction (27) is suppressed, giving the highest observed degree of Pt-Co alloying.

The Mukherjee group applied these mechanistic insights and controlled both the sizes and compositions of ternary Pt-Co-Cu alloys (Figure 36(c)) by ablating cobalt in mixed K_2PtCl_4 and CuCl solutions [327]. As illustrated in Figure 36(d), the ablation time and fluence controlled the nanoparticle sizes (reflected in the size of the pie charts), whereas the solution pH and concentrations of K_2PtCl_4 and CuCl controlled the relative content of each constituent element. The authors also produced homogeneous Pt-Co-Mn and Pt-Ru-Ni alloy nanoparticles by ablating manganese in K_2PtCl_4-$CoCl_2$ solution, and nickel in K_2PtCl_4-$RuCl_2$ solution, respectively. They concluded that galvanic replacement reactions such as shown in eq. (26) constitute a general route to alloy nanoparticles synthesis, provided that the metals and salts are chosen such that the solid target has the lowest reduction potential. That way, its ablated atoms can reduce the metal ions in solution.

5.2.4 *Metal sulfide semiconductors*

In addition to homogeneous metal alloys, RLAL has recently been used to produce homogeneous metal sulfide semiconductor nanoparticles [328-331]. Interestingly, both the ablation of a sulfur target in a metal ion solution, and the ablation of metals in sulfur precursor liquid dimethyl sulfoxide (DMSO), will produce metal sulfide phases. Darwish et al. [328, 329] produced CdS nanoparticles by ablating a sulfur target in aqueous $CdCl_2$. Mostafa et al. [330] ablated cadmium, tin, and copper in DMSO, to produce CdS, SnS, and CuS nanoparticles. The particles did contain small amounts of carbon as a result of DMSO decomposition in the laser plasma. Naik et al. [331] synthesized pure wurtzite ZnS-phase nanospheres by ablating zinc in DMSO. In a subsequent RLFL step, they irradiated the ZnS product in methanol solutions containing $HAuCl_4$ with low-fluence, 532 nm nanosecond laser pulses, and deposited AuNPs onto the ZnS nanosphere supports. These composites were ultimately deposited on multiwall carbon nanotubes, and used for selective electrochemical detection of 4-nitrophenol, an organic pollutant.

5.3 Structured nanomaterials

RLAL has been used to produce structured nanomaterials; the result of reactions between ablated target materials and metal precursors in solution. Structured nanomaterials include complex minerals [332], polyoxometalates [333-335], sheet-like minerals [336-341], and MOFs [342-345]. To form these complex, structured materials, it is critical to control the chemical environment of the liquid medium. For instance, the particular counterion partnered with the copper or zinc salt precursor added to aqueous solution during ablation of copper or zinc solids, will determine the mineral produced

[332]. Ablating copper in aqueous $CuCl_2$ produced paratacamite ($Cu_2Cl(OH)_3$), whereas ablating copper in aqueous $Cu(NO_3)_2$ and NH_4OH produced rouaite ($Cu_2(NO_3)(OH)_3$) [332].

The use of an external electric field applied to metal electrodes used a metal ion source—in what is termed electrochemically assisted LAL (ECLAL) [333-335]—has been used to produce diverse bimetallic polyoxometalate structures, or "POMs". Ablation of a molybdenum target between copper electrodes in deionized water with 532, 10 ns pulses produced lindgrenite ($Cu_3(OH)_2(MoO_4)_2$) nanorods (Figure 37(a)) [333]. The self-assembly of lindgrenite structures was attributed to the electrochemical dissolution of copper metal in the electrode to release $Cu(OH)_2$ in solution, which reacted with ablated MoO_3 or MoO_4^{2-} and produced $Cu_3(OH)_2(MoO_4)_2$ [333]. A similar reaction mechanism was proposed for the formation of plate- and rod-like zinc molybdenum oxide hydrate ($Zn_5Mo_2O_{11}{\cdot}5H_2O$) structures (Figure 37(b)) [334], involving the electrochemical formation of $Zn(OH)_2$, which reacted with molybdenum species. Multiple copper vanadate phases were formed from the ablation of a vanadium target with copper electrodes, where particle morphology depended strongly on the applied electric field [335]. At 40 V, flower-like structures composed of nanoflakes were formed (Figure 37(c)). Increasing the field strength to 80 V resulted in agglomerates of these flower structures (Figure 37(d)), and a further increase to 120 V generated large, block-like particles (Figure 37(e)). The authors attributed this trend to faster particle growth as the electric field increased [335], which is also in accordance with the elevated availability of copper species in solution. Moreover, as the concentration of copper species in solution rises, the resulting structures become increasingly isotropic. This trend

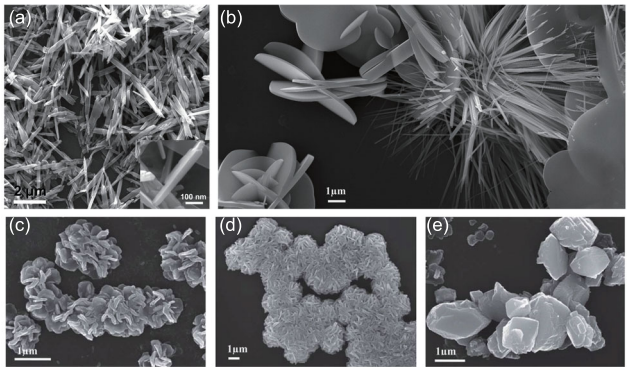

Figure 37 Polyoxometalate nanostructures synthesized by ECLAL: $Cu_2(OH)_2(MoO_4)_2$ nanorods (a); $Zn_5Mo_2O_{11}{\cdot}5H_2O$ plates and rods (b); copper vanadate structures synthesized with electric fields at 40 V (c), 80 V (d), and 120 V (e). Adapted from ref. [333] (a) copyright 2011, American Chemical Society; ref. [334] (b) copyright 2012, American Chemical Society; and ref. [335] (c)-(e) with permission from Royal Society of Chemistry.

is consistent with observations of the nanostructures deposited onto silicon surfaces during RLAL processes (cf. sect. 5.4), suggesting similar particle growth mechanisms.

Various sheet-like nanominerals have also been synthesized by RLAL. Zhang et al. [336] synthesized Mn-doped $Ni(OH)_2$ nanosheets via ablation of a manganese target in aqueous $NiCl_2$ solution with 1064 nm, 10 ns pulses. The resulting 3 nm thick nanosheets occasionally self-assembled into flower-like structures (Figure 38(a)). The Müller group [337,338] synthesized Ni-Fe layered double-hydroxide structures, $[Ni_{1-x}Fe_x(OH)_2](NO_3)_y(OH)_{x-y}{\cdot}nH_2O$, via ablation of powdered nickel in a solution of $Fe(NO_3)_3$, and powdered iron in a solution of $Ni(NO_3)_2$. The addition of nitrate salts of Ti^{4+} and La^{3+} enabled the generation of Ti- and La-doped materials, respectively [337]. Later, Lee et al. [339] synthesized [Ni-Fe] layered double-hydroxides by ablating a solid nickel target in $FeCl_3$ solution (Figure 38(b)). These layered double hydroxide materials were used as water-oxidation catalysts [337, 338] and for photocatalytic H_2 generation [339]. John and Tibbetts [340, 341] synthesized Cu- and Ni-phyllosilicate nanostructures by ablating silicon wafers in basic solutions of $Cu(NO_3)_2$ and $Ni(NO_3)_2$, respectively. The Cu-phyllosilicate (Figure 38(c)) and Ni-phyllosilicate (Figure 38(d)) exhibited the distinct structural features characteristic of phyllosilicate materials [340, 341].

To elucidate the reaction mechanisms leading to phyllosilicate formation during RLAL, John and Tibbetts analyzed dissolved anions that remained in solution after RLAL [341]. Having previously determined that RLAL only produced copper and nickel phyllosilicates under basic conditions (solution pH > 8) [340, 341], they characterized the dissolved anions produced by ablating a silicon wafer in water and $Ni(NO_3)_2$ solution at initial solution pH of ~6 and ~11, using electrospray mass spectrometry (Figure 39). When silicon was ablated in water at pH 5.9, the solution pH changed very little, and the metasilicate ion ($SiO_2(OH)^-$) was observed in the mass spectrum. When KOH was added to the water to raise the pH to 11.7, silicon wafer ablation resulted in a pH-drop of two units, to pH 9.7, and silicic acid ($SiO(OH)_3^-$) was observed in the mass spectrum. In the presence of $Ni(NO_3)_2$, ablation at pH 5.9 again produced little pH change, and the soluble Ni-O-Si monomer $[(H_2O)_5NiOSi(H_2O)_2O]^-$ was detected in the mass spectrum. In contrast, ablation at pH 10.6 dropped the solution pH to 8.6, and no nickel-containing species were detected in the mass spectrum. These results indicated that the silicic acid formed by ablation of the silicon wafer in basic solution is what initiates the formation of phyllosilicate structures; it consumes all available nickel species in solution [341].

Reactive-LAL has also successfully produced MOF structures by reacting ablated metal species with precursor

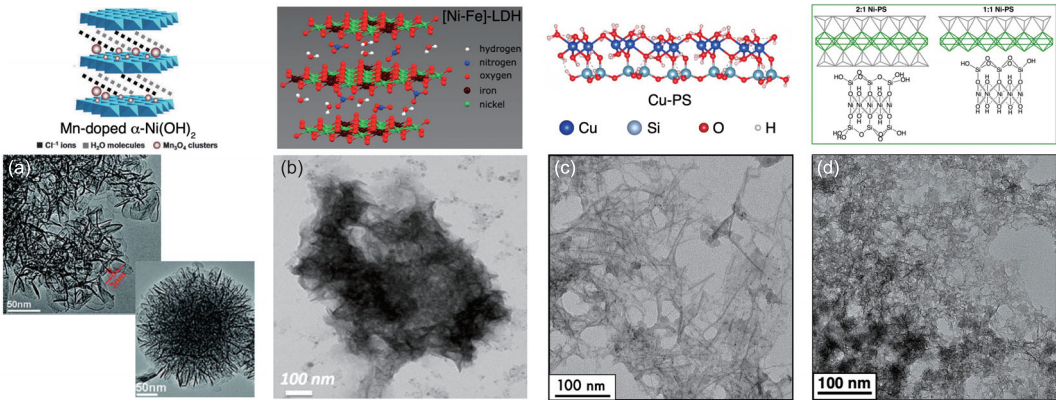

Figure 38 (Color online) Minerals from RLAL: Mn-doped $Ni(OH)_2$ nanosheets (a), NiFe layered double hydroxides (b), Cu-phyllosilicate (c), and Ni-phyllosilicate (d). Adapted from ref. [336] (a) with permission from the Royal Society of Chemistry; ref. [339] (b), copyright 2018 American Chemical Society; ref. [337] (b), copyright 2014 American Chemical Society; ref. [340] (c) copyright 2020, with permission from Elsevier; and ref. [341] (d), copyright 2020 American Chemical Society.

molecules in solution [342-345]. The Mukherjee group [342, 343] synthesized zeolitic imidazolate framework-67 (ZIF-67) structures by ablating solid cobalt targets in basic aqueous solutions containing the organic linker 2-methylimidazole with a 1064 nm Nd:YAG laser. Maintaining the ablated solution at 65°C for 12 h resulted in the growth of ZIF-67 crystals, whose sizes were controlled by varying the ablation time and the concentration of the organic linker in the precursor solution (Figure 40(a)). Low 2-methylimidazole concentration with long ablation time produced the largest cubic ZIF-67 crystals, whereas high 2-methylimidazole concentration with short ablation time produced the smallest crystals. The authors proposed that oxidation of initially-produced CoNPs by the dissolved oxygen present in solution releases Co^{2+} ions that coordinate with the organic linker in solution. Subsequent deprotonation of the cobalt-coordinated 2-methylimidazole produces ZIF-67 monomers, which spontaneously polymerize to create the ZIF-67 crystals (Figure 40(b)). The same group subsequently embedded PtNPs into the ZIF-67 structures by performing ablation in solutions containing both K_2PtCl_4 and 2-methylimidazole, which were subsequently pyrolyzed to yield active oxygen-reduction electrocatalysts [343]. Additional MOFs synthesized by RLAL include a bismuth MOF (Bi-BTC) synthesized by ablation of a bismuth target in methanol-dimethylformamide solutions of the bridging ligand benzene-1,3,5-tricarboxylic acid [344] and zinc MOF-5, synthesized by ablating a zinc target in dimethylformamide solutions of the same acid [345].

5.4 Metal nanostructures deposited on surfaces

In addition to the myriad RLAL-synthesized nanostructures discussed in this section already, RLAL also allows the deposition of metal nanostructures onto solid targets. For instance, Cu_2O and copper structures are deposited onto glass and sapphire when the target is ablated in a basic aqueous solution of $CuSO_4$, with 1064 nm nanosecond pulses [346-348]. In these studies, copper deposition onto the

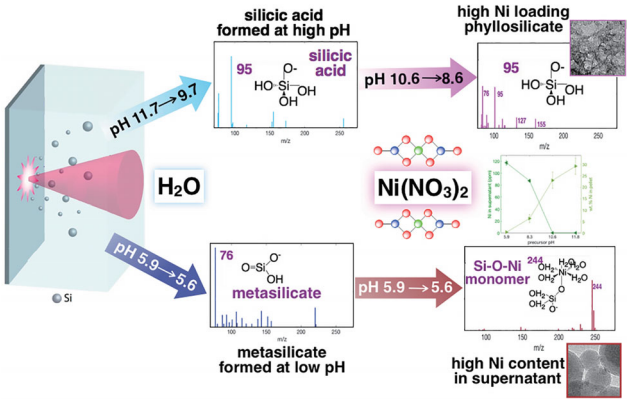

Figure 39 (Color online) Mass spectra of dissolved anions after ablation of a silicon wafer in water and aqueous $Ni(NO_3)_2$, at acidic and basic pH, to explain the formation of nickel phyllosilicates. Reproduced from ref. [341], copyright 2020 American Chemical Society.

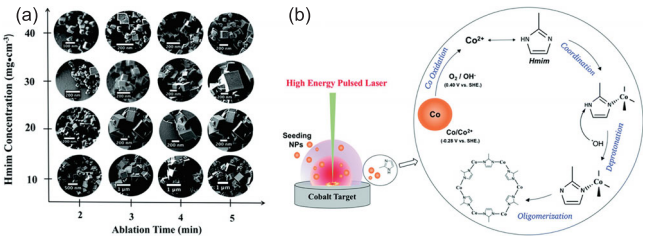

Figure 40 (Color online) SEM images of MOF ZIF-67 synthesized by RLAL with different linker concentrations and ablation times (a). Proposed mechanism of ZIF-67 formation during RLAL (b). Adapted from ref. [342] with permission from Royal Society of Chemistry.

substrate is a result of laser-induced heating, which decomposes $CuSO_4$ to produce CuO, which is then reduced to Cu_2O by SO_2 gas, another product of $CuSO_4$ decomposition [347]. Gold nanoparticles can be directly written onto glass [349] and TiO_2 [350] surfaces by ablation with femtosecond laser pulses in aqueous solutions of $HAuCl_4$. Continuous-wave lasers at UV wavelengths can also deposit Au-Ag [351, 352] and Ag-Pt [353, 354] nanostructures onto glass, quartz, sapphire, and silicon, when organic polynuclear metal (Au, Ag, Pt) complexes are used as metal precursors. Direct absorption of UV photons by the organic polynuclear metal complexes decomposes them and reduces the metals [351-354].

As well as depositing metal nanostructures on dielectric substrates, 800 nm, 30-120 fs pulses can also simultaneously write nanostructures onto silicon substrates while depositing metals onto those structures [355-362]. Ultrashort pulsed-laser processing has been used for decades to write laser-induced periodic surface structures (LIPSS) onto solid metal or semiconductor surfaces [363]. Ablating these targets in liquid instead of air has the benefit of forming of LIPSS with spatial periods significantly shorter than the laser wavelength, which are termed "high spatial-frequency LIPSS" (HSFL). The primary use of RLAL has been to deposit silver nanostructures onto silicon LIPSS to make SERS substrates [355-359]. Deposition of gold [360, 361] and copper [362] have also been reported. These metal nanostructures can be deposited in a single step by RLAL of a pristine silicon wafer in metal precursor solution [359, 361, 362]. Many studies use two-step strategies in which the silicon wafer is first ablated in water, and then ablated again with time-delayed pairs of femtosecond pulses in metal precursor solution to increase the amount of metal deposited [355-358, 360]. Figure 41 shows representative examples of deposited gold [360], silver [359], and copper [362] nanostructures on silicon LIPSS.

Li et al. [360] deposited gold nanostructures in a two-step process. First, the silicon wafer was ablated in water to generate LIPSS. Then, it was immersed in a solution of 0.05 M $HAuCl_4$ with potassium sodium tartrate ($NaKC_4H_4O_6$) added as an additional reducing agent, and ablated with pulse pairs. The authors found that at constant pulse energy, the sample's scan speed determined the morphology of the deposited gold nanostructures. Fast scanning (160 μm/s) made plate-like gold structures (Figure 41(a)), whereas slow scanning (20 μm/s) culminated in agglomerated spherical gold structures (Figure 41(b)). Slower scanning speeds allow more laser energy to absorb over a given area. With more pulses able to interact, initially-deposited gold structures can be fragmented by subsequent laser pulses [360].

Ran et al. [359] found that the morphology and sizes of the silver nanostructures deposited onto silicon depended on both the $AgNO_3$ precursor concentration and pulse energy. A 0.4 μJ pulse energy and an 0.5 M $AgNO_3$ concentration culminated in large, block-like silver crystals (Figure 41(c)). A lower $AgNO_3$ concentration of 0.05 M at the same pulse energy produced thin silver plates (Figure 41(d)). When the pulse energy was increased to 0.54 μJ, a 0.05 M $AgNO_3$ concentration decreased the density of silver plates (Figure 41(e)). Increasing the pulse energy to 0.76 μJ resulted in the deposition of smaller silver particles, with low particle-density on the surface (Figure 41(f)). The formation of silver blocks in high $AgNO_3$ concentrations was attributed to the availability of silver, allowing isotropic growth along all surface facets of the initially-deposited silver nuclei. In contrast, particle growth in low silver concentrations proceeded preferentially along the (110) surface facet of the nuclei because of its higher surface energy, producing plate structures [359]. The lower density and smaller size of silver nanostructures obtained at high laser-fluence can be credited to faster plasma expansion; it removes reduced Ag^0 atoms from the vicinity

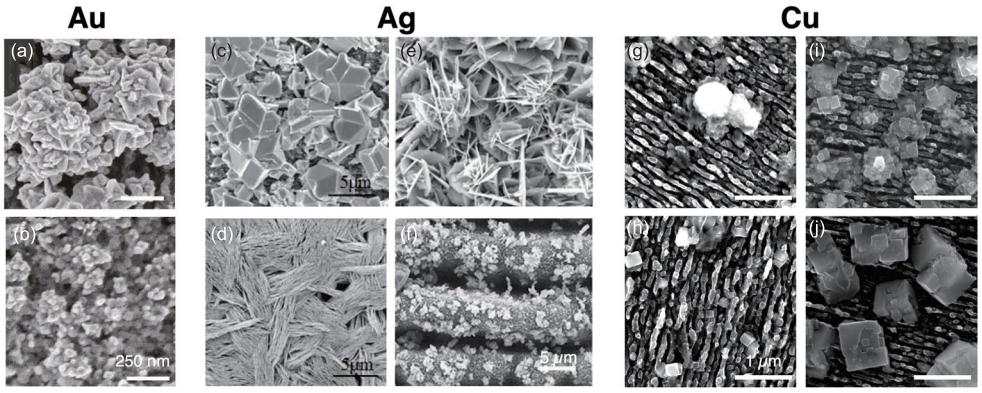

Figure 41 SEM images of gold (a), (b), silver (c)-(f), and copper (g)-(j) nanostructures deposited on silicon via RLAL at different sample translation speeds, laser fluences, and precursor concentrations, as indicated in the text. Adapted from ref. [360] (a), (b), CC-BY-3.0; ref. [359] (c)-(f), copyright 2019 Wiley-VCH; and ref. [362] (g)-(j), copyright 2021 American Chemical Society.

of the silicon surface, inhibiting silver deposition [359].

Broadhead et al. [362] found that the morphology of deposited copper nanostructures depended on the $Cu(NO_3)_2$ precursor concentration, and particle size depended on the sample scan speed. Copper was deposited as quasi-spherical particles at 4 mM $Cu(NO_3)_2$ (Figure 41(g)). Lowering the precursor concentration to 1 mM resulted in the deposition of cubic nanostructures (Figure 41(h), (j)). Slowing the scanning speed from 200 μm/s (Figure 41(h)) to 100 μm/s (Figure 41(i)) increased the size of the cubic particles, and caused some agglomeration. Further reduction in the scan speed to 50 μm/s (Figure 41(j)) produced substantially larger cubic structures, and increased copper deposition on the surfaces to 11.7 wt% from 4.6 wt% at 200 μm/s. The production of larger and more well-ordered copper structures with reduced scanning speed is connected to prolonged laser-pulse exposure; a slower sweep allows more copper to be reduced and deposited [362]. This is a reversal of the pattern exhibited by gold (Figure 41(a), (b)), for which increased laser exposure was thought to partially decompose deposited structures [360]. The nanostructure's morphological dependence on precursor concentration was attributed to the preferential growth along the high-energy, (111) surface facet of copper; indicating a similar growth mechanism as observed for silver (Figure 41(c)-(f)) [359].

Beyond the well-established role that plasma electrons play in metal ion reduction, enabling their deposition onto silicon LIPSS [359-362], other physical and chemical mechanisms come into play. As demonstrated by varying the laser pulse energy [359], excessively fast plasma expansion and cavitation-bubble diffusion will both transport reduced metal species away from the substrate, inhibiting their deposition onto the surface of the target. Variation of chemical parameters like solution pH [361,362] and auxiliary reducing agents such as $NaKC_4H_4O_6$ [360] enabled control over the quantity of metal deposited. Low solution pH (<5) inhibited deposition of both gold and copper because of the shortened lifetimes of e^-_{aq} in the presence of H_3O^+; discussed in sect. 2.1 [361,362]. High solution pH (>8) also resulted in low gold and copper deposition due to unwanted side-reactions in solution: $KAuCl_4$ reduced too quickly to be efficiently deposited onto the silicon surfaces [361], and $Cu(NO_3)_2$ reacted with silicon species to produce copper phyllosilicate (cf. sect. 5.3) which prevented copper deposition. Consequently, neutral pH ~7 optimized metal deposition. The addition of $NaKC_4H_4O_6$ assisted with $HAuCl_4$ reduction by acting as a $OH^\bullet$ scavenger and allowing the formation of the $KNaC_4H_3O_6^\bullet$ radical, which is capable of reducing Au^{3+} [360]. With the help of this scavenger, deposition of gold nanostructures can proceed at lower laser fluence to avoid damaging the silicon substrate.

Post-irradiation chemical reactions also contribute to metal deposition onto LIPSS. The continued growth of silver nanostructures for up to ten hours after laser irradiation is terminated [359] indicates that some long-lived reducing species are formed. In another instance, both gold and copper were successfully deposited onto silicon LIPSS by ablating the silicon in water and then transferring it to a precursor solution (of either $KAuCl_4$ or $Cu(NO_3)_2$) and allowing it to sit for 45 min without further irradiation—albeit with only ~50% the efficiency of the standard RLAL procedure [361,362]. These results are consistent with previous work [308-310] (cf. sect. 5.2, Figure 32) which demonstrate metal ion reduction by ablated SiNPs. The ability of nanostructured silicon to reduce metal ions in solution also explains the success of two-step RLAL approaches [355-358,360]. The first step, producing silicon LIPSS, results in active silicon surfaces that more readily reduce metal ions in the second step, increasing the quantity of metal deposited.

6 Outlook and future directions

Reactive laser-synthesis techniques have generated a variety of nanomaterials over the past decade, as examined in this review, and their myriad applications continue to inspire researchers. Reactive laser-synthesis has a lot to offer as a route to complex nanomaterial synthesis, an avenue that is not accessible by established LAL, LFL, and LML methods. For instance, structured materials such as polyoxometalates [333-335], layered double-hydroxides [337,338], phyllosilicates [340,341], and MOFs [342,343] can only be formed by chemical reactions between both ablated species and precursors, within the environment of a cavitation bubble or in the bulk solution. The success of RLAL in producing these materials suggests that additional 2D and 3D material structures, with potential applications in the development of technology such as perovskites and MXenes, is possible with strategic procedural design. Due to the highly non-equilibrium reaction environments produced, novel material structures, yet undiscovered, may be accessible through reactive laser-synthesis.

The primary challenge to obtaining tailored control over complex material properties like structures, sizes, compositions, and material phases; is insufficient understanding of the chemical reaction mechanisms that govern nanomaterial assembly. The current state of knowledge for reactive laser-synthesis mechanisms mirrors that for LAL a decade ago, before extensive investigations into the physical mechanisms of laser ablation. Those investigations eventually revealed the dynamics of cavitation bubbles [38-40] and nanoparticle growth [41-43] and elucidated the cause-and-effect relation-

ships between the mechanisms and eventual product characteristics. There are therefore plenty of opportunities to further our knowledge of the chemical mechanisms in reactive laser-synthesis using targeted experimental and theoretical investigations. Importantly, these types of mechanistic investigations will also hone the tailoring of reaction conditions in LAL, LFL, and LML studies, described in sect. 3.

To date, *in situ* studies of reaction kinetics [63,64,202,243] and systematic variations of reaction parameters [325-327] have both revealed key reaction mechanisms governing nanomaterial formation in reactive laser-synthesis. Additional studies applying these types of methods to other reactive systems are necessary to move forward. Moreover, time-resolved techniques used in LAL studies, including OES [101, 127, 129-131] and XAFS [132], that measure chemical species on nanosecond-microsecond timescales should be applied to reactive laser-synthesis. For LRL syntheses where no solids are involved, transient absorption measurements may identify species on timescales as short as 100 fs. Transient absorption has already been used to determine the lifetimes of hydrated electrons [58, 67] and organic radicals [86-89] in solution. Collectively, these time-resolved techniques would identify specific transient chemical species present in the plasma and cavitation bubble, before they assemble into the final nanomaterial products. Coupled to *ex situ* mass spectrometry measurements of reaction byproducts [52, 82-84, 134, 341], the identification of transient species would make it possible to complete the picture of the reaction pathways involved. Finally, incorporating chemical reactivity into the established, atomistic models of LAL on picosecond-nanosecond timescales [34-37] would fill in experimental gaps in our comprehension of the early stages of the chemical reactions between ablated atoms and species in solution.

Rapid advancement in laser technology over the past two decades has empowered the evolution of LAL and related techniques; elevating them from merely promising bare-nanoparticle synthesis routes to well-established methods for nanoparticle production at an industrial scale [31]. Reactive techniques like LRL, RLAL, and RLFL represent a new frontier in laser nanomaterials synthesis, with countless opportunities to discover new types of nanomaterials and develop environmentally-friendly paths to scalable synthesis.

1 C. Wei, Z. Zhang, D. Cheng, Z. Sun, M. Zhu, and L. Li, Int. J. Extrem. Manuf. **3**, 012003 (2021).
2 D. Loterie, P. Delrot, and C. Moser, Nat. Commun. **11**, 852 (2020).
3 T. Hupfeld, S. Salamon, J. Landers, A. Sommereyns, C. Doñate-Buendía, J. Schmidt, H. Wende, M. Schmidt, S. Barcikowski, and B. Gökce, J. Mater. Chem. C **8**, 12204 (2020).
4 L. Jonušauskas, D. Gailevičius, S. Rekštytė, T. Baldacchini, S. Juodkazis, and M. Malinauskas, Opt. Express **27**, 15205 (2019).
5 Q. Ge, Z. Li, Z. Wang, K. Kowsari, W. Zhang, X. He, J. Zhou, and N. X. Fang, Int. J. Extrem. Manuf. **2**, 022004 (2020).
6 A. Awad, F. Fina, A. Goyanes, S. Gaisford, and A. W. Basit, Int. J. Pharm. **586**, 119594 (2020).
7 A. Y. Zhizhchenko, P. Tonkaev, D. Gets, A. Larin, D. Zuev, S. Starikov, E. V. Pustovalov, A. M. Zakharenko, S. A. Kulinich, S. Juodkazis, A. A. Kuchmizhak, and S. V. Makarov, Small **16**, 2000410 (2020).
8 P. Mueller, M. M. Zieger, B. Richter, A. S. Quick, J. Fischer, J. B. Mueller, L. Zhou, G. U. Nienhaus, M. Bastmeyer, C. Barner-Kowollik, and M. Wegener, ACS Nano **11**, 6396 (2017).
9 Y. Huang, R. Field, Q. Chen, Y. Peng, M. S. Walczak, H. Zhao, G. Zhu, Z. Liu, and L. Li, Commun. Chem. **2**, 138 (2019).
10 F. Sima, H. Kawano, M. Hirano, A. Miyawaki, K. Obata, D. Serien, and K. Sugioka, Adv. Mater. Technol. **5**, 2000484 (2020).
11 P. N. Bernal, P. Delrot, D. Loterie, Y. Li, J. Malda, C. Moser, and R. Levato, Adv. Mater. **31**, 1904209 (2019).
12 S. Barcikowski, J. Walter, A. Hahn, J. Koch, H. Haloui, T. Herrmann, and A. Gatti, J. Laser Micro Nanoeng. **4**, 159 (2009).
13 P. Anastas, and N. Eghbali, Chem. Soc. Rev. **39**, 301 (2010).
14 V. Amendola, and M. Meneghetti, Phys. Chem. Chem. Phys. **15**, 3027 (2013).
15 P. Liu, H. Cui, C. X. Wang, and G. W. Yang, Phys. Chem. Chem. Phys. **12**, 3942 (2010).
16 H. Zeng, X. W. Du, S. C. Singh, S. A. Kulinich, S. Yang, J. He, and W. Cai, Adv. Funct. Mater. **22**, 1333 (2012).
17 D. Tan, S. Zhou, J. Qiu, and N. Khusro, J. Photochem. Photobiol. C-Photochem. Rev. **17**, 50 (2013).
18 S. Barcikowski, and G. Compagnini, Phys. Chem. Chem. Phys. **15**, 3022 (2013).
19 J. Xiao, P. Liu, C. X. Wang, and G. W. Yang, Prog. Mater. Sci. **87**, 140 (2017).
20 D. Zhang, B. Gökce, and S. Barcikowski, Chem. Rev. **117**, 3990 (2017).
21 D. S. Zhang, J. Liu, and C. H. Liang, Sci. China-Phys. Mech. Astron. **60**, 074201 (2017).
22 D. Zhang, J. Liu, P. Li, Z. Tian, and C. Liang, ChemNanoMat **3**, 512 (2017).
23 J. Zhang, M. Chaker, and D. Ma, J. Colloid Interface Sci. **489**, 138 (2017).
24 S. Reichenberger, G. Marzun, M. Muhler, and S. Barcikowski, ChemCatChem **11**, 4489 (2019).
25 A. Kanitz, M. R. Kalus, E. L. Gurevich, A. Ostendorf, S. Barcikowski, and D. Amans, Plasma Sources Sci. Technol. **28**, 103001 (2019).
26 E. Fazio, B. Gökce, A. De Giacomo, M. Meneghetti, G. Compagnini, M. Tommasini, F. Waag, A. Lucotti, C. G. Zanchi, P. M. Ossi, M. Dell'Aglio, L. D'Urso, M. Condorelli, V. Scardaci, F. Biscaglia, L. Litti, M. Gobbo, G. Gallo, M. Santoro, S. Trusso, and F. Neri, Nanomaterials **10**, 2317 (2020).
27 V. Amendola, D. Amans, Y. Ishikawa, N. Koshizaki, S. Scirè, G. Compagnini, S. Reichenberger, and S. Barcikowski, Chem. Eur. J. **26**, 9206 (2020).
28 S. X. Liang, L. C. Zhang, S. Reichenberger, and S. Barcikowski, Phys. Chem. Chem. Phys. **23**, 11121 (2021).
29 N. G. Semaltianos, and G. Karczewski, ACS Appl. Nano Mater. **4**, 6407 (2021).
30 R. C. Forsythe, C. P. Cox, M. K. Wilsey, and A. M. Müller, Chem. Rev. **121**, 7568 (2021).
31 D. Zhang, Z. Li, and K. Sugioka, J. Phys. Photonics **3**, 042002 (2021).
32 D. Werner, and S. Hashimoto, J. Phys. Chem. C **115**, 5063 (2011).
33 P. Boyer, and M. Meunier, J. Phys. Chem. C **116**, 8014 (2012).
34 C. Y. Shih, C. Wu, M. V. Shugaev, and L. V. Zhigilei, J. Colloid Interface Sci. **489**, 3 (2017).
35 C. Y. Shih, R. Streubel, J. Heberle, A. Letzel, M. V. Shugaev, C. Wu, M. Schmidt, B. Gökce, S. Barcikowski, and L. V. Zhigilei, Nanoscale **10**, 6900 (2018).
36 C. Y. Shih, M. V. Shugaev, C. Wu, and L. V. Zhigilei, Phys. Chem.

Chem. Phys. **22**, 7077 (2020).
37 C. Y. Shih, C. Chen, C. Rehbock, A. Tymoczko, U. Wiedwald, M. Kamp, U. Schuermann, L. Kienle, S. Barcikowski, and L. V. Zhigilei, J. Phys. Chem. C **125**, 2132 (2021).
38 A. De Giacomo, M. Dell'Aglio, A. Santagata, R. Gaudiuso, O. De Pascale, P. Wagener, G. C. Messina, G. Compagnini, and S. Barcikowski, Phys. Chem. Chem. Phys. **15**, 3083 (2013).
39 M. Dell'Aglio, R. Gaudiuso, O. De Pascale, and A. De Giacomo, Appl. Surf. Sci. **348**, 4 (2015).
40 S. Kohsakowski, B. Gökce, R. Tanabe, P. Wagener, A. Plech, Y. Ito, and S. Barcikowski, Phys. Chem. Chem. Phys. **18**, 16585 (2016).
41 P. Wagener, S. Ibrahimkutty, A. Menzel, A. Plech, and S. Barcikowski, Phys. Chem. Chem. Phys. **15**, 3068 (2013).
42 A. Letzel, B. Gökce, P. Wagener, S. Ibrahimkutty, A. Menzel, A. Plech, and S. Barcikowski, J. Phys. Chem. C **121**, 5356 (2017).
43 K. Ando, and T. Nakajima, Nanoscale **12**, 9640 (2020).
44 P. J. Bruggeman, M. J. Kushner, B. R. Locke, J. G. E. Gardeniers, W. G. Graham, D. B. Graves, R. C. H. M. Hofman-Caris, D. Maric, J. P. Reid, E. Ceriani, D. Fernandez Rivas, J. E. Foster, S. C. Garrick, Y. Gorbanev, S. Hamaguchi, F. Iza, H. Jablonowski, E. Klimova, J. Kolb, F. Krcma, P. Lukes, Z. Machala, I. Marinov, D. Mariotti, S. Mededovic Thagard, D. Minakata, E. C. Neyts, J. Pawlat, Z. L. Petrovic, R. Pflieger, S. Reuter, D. C. Schram, S. Schröter, M. Shiraiwa, B. Tarabová, P. A. Tsai, J. R. R. Verlet, T. von Woedtke, K. R. Wilson, K. Yasui, and G. Zvereva, Plasma Sources Sci. Technol. **25**, 053002 (2016).
45 B. Rethfeld, D. S. Ivanov, M. E. Garcia, and S. I. Anisimov, J. Phys. D-Appl. Phys. **50**, 193001 (2017).
46 A. Vogel, K. Nahen, D. Theisen, and J. Noack, IEEE J. Sel. Top. Quantum Electron. **2**, 847 (1996).
47 J. Noack, and A. Vogel, IEEE J. Quantum Electron. **35**, 1156 (1999).
48 A. Vogel, J. Noack, K. Nahen, D. Theisen, S. Busch, U. Parlitz, D. X. Hammer, G. D. Noojin, B. A. Rockwell, and R. Birngruber, Appl. Phys. B **68**, 271 (1999).
49 A. Vogel, J. Noack, G. Hüttman, and G. Paltauf, Appl. Phys. B **81**, 1015 (2005).
50 M. G. John, V. K. Meader, and K. M. Tibbetts, in *Au nanoparticle synthesis via femtosecond laser-induced photochemical reduction of [AuCl$_4$]$^-$: Photochemistry and Photophysics—Fundamentals to Applications*, edited by S. Saha, and S. Mondal, chapter 8 (IntechOpen, London, 2018).
51 N. Linz, S. Freidank, X. X. Liang, and A. Vogel, Phys. Rev. B **94**, 024113 (2016).
52 A. V. Simakin, M. E. Astashev, I. V. Baimler, O. V. Uvarov, V. V. Voronov, M. V. Vedunova, M. A. Sevost'yanov, K. N. Belosludtsev, and S. V. Gudkov, J. Phys. Chem. B **123**, 1869 (2019).
53 I. V. Baimler, A. V. Simakin, O. V. Uvarov, M. Y. Volkov, and S. V. Gudkov, Phys. Wave Phen. **28**, 107 (2020).
54 A. Couairon, and A. Mysyrowicz, Phys. Rep. **441**, 47 (2007).
55 J. A. LaVerne, Radiat. Res. **153**, 196 (2000).
56 B. R. Locke, and S. M. Thagard, Plasma Chem. Plasma Process **32**, 875 (2012).
57 J. Ma, S. A. Denisov, A. Adhikary, and M. Mostafavi, Int. J. Mol. Sci. **20**, 4963 (2019).
58 S. Pommeret, F. Gobert, M. Mostafavi, I. Lampre, and J. C. Mialocq, J. Phys. Chem. A **105**, 11400 (2001).
59 D. N. Nikogosyan, A. A. Oraevsky, and V. I. Rupasov, Chem. Phys. **77**, 131 (1983).
60 E. Janata, and R. H. Schuler, J. Phys. Chem. **86**, 2078 (1982).
61 R. O. Rahn, Photochem. Photobiol. **66**, 450 (1997).
62 N. Nakashima, K. Yamanaka, M. Saeki, H. Ohba, S. Taniguchi, and T. Yatsuhashi, J. Photochem. Photobiol. A-Chem. **319-320**, 70 (2016).
63 V. K. Meader, M. G. John, C. J. Rodrigues, and K. M. Tibbetts, J. Phys. Chem. A **121**, 6742 (2017).
64 H. Belmouaddine, M. Shi, P. L. Karsenti, R. Meesat, L. Sanche, and D. Houde, Phys. Chem. Chem. Phys. **19**, 7897 (2017).
65 N. Nakashima, T. Yatsuhashi, K. Sakota, I. Iwakura, S. Hashimoto, K. Yokoyama, and S. Matsuda, Chem. Phys. Lett. **752**, 137570 (2020).
66 Z. H. Loh, G. Doumy, C. Arnold, L. Kjellsson, S. H. Southworth, A. Al Haddad, Y. Kumagai, M. F. Tu, P. J. Ho, A. M. March, R. D. Schaller, M. S. Bin Mohd Yusof, T. Debnath, M. Simon, R. Welsch, L. Inhester, K. Khalili, K. Nanda, A. I. Krylov, S. Moeller, G. Coslovich, J. Koralek, M. P. Minitti, W. F. Schlotter, J. E. Rubensson, R. Santra, and L. Young, Science **367**, 179 (2020).
67 R. A. Crowell, and D. M. Bartels, J. Phys. Chem. **100**, 17940 (1996).
68 S. L. Chin, and S. Lagacé, Appl. Opt. **35**, 907 (1996).
69 H. Kierzkowska-Pawlak, J. Tyczkowski, A. Jarota, and H. Abramczyk, Appl. Energy **247**, 24 (2019).
70 J. H. Odhner, K. Moore Tibbetts, B. Tangeysh, B. B. Wayland, and R. J. Levis, J. Phys. Chem. C **118**, 23986 (2014).
71 C. J. Rodrigues, J. A. Bobb, M. G. John, S. P. Fisenko, M. S. El-Shall, and K. M. Tibbetts, Phys. Chem. Chem. Phys. **20**, 28465 (2018).
72 J. A. Bobb, C. J. Rodrigues, M. S. El-Shall, and K. M. Tibbetts, Phys. Chem. Chem. Phys. **22**, 18294 (2020).
73 V. K. Meader, M. G. John, L. M. Frias Batista, S. Ahsan, and K. M. Tibbetts, Molecules **23**, 532 (2018).
74 B. Tangeysh, K. M. Tibbetts, J. H. Odhner, B. B. Wayland, and R. J. Levis, J. Phys. Chem. C **117**, 18719 (2013).
75 B. Tangeysh, K. M. Tibbetts, J. H. Odhner, B. B. Wayland, and R. J. Levis, Nano Lett. **15**, 3377 (2015).
76 B. Tangeysh, K. M. Tibbetts, J. H. Odhner, B. B. Wayland, and R. J. Levis, Langmuir **33**, 243 (2017).
77 K. M. Tibbetts, B. Tangeysh, J. H. Odhner, and R. J. Levis, J. Phys. Chem. A **120**, 3562 (2016).
78 J. A. LaVerne, and S. M. Pimblott, J. Phys. Chem. A **104**, 9820 (2000).
79 G. Maatz, A. Heisterkamp, H. Lubatschowski, S. Barcikowski, C. Fallnich, H. Welling, and W. Ertmer, J. Opt. A-Pure Appl. Opt. **2**, 59 (2000).
80 T. Nakamura, Y. Mochidzuki, and S. Sato, J. Mater. Res. **23**, 968 (2008).
81 E. V. Barmina, A. V. Simakin, and G. A. Shafeev, Chem. Phys. Lett. **678**, 192 (2017), arXiv: 1701.03367.
82 M. R. Kalus, N. Bärsch, R. Streubel, E. Gökce, S. Barcikowski, and B. Gökce, Phys. Chem. Chem. Phys. **19**, 7112 (2017).
83 M. R. Kalus, R. Lanyumba, N. Lorenzo-Parodi, M. A. Jochmann, K. Kerpen, U. Hagemann, T. C. Schmidt, S. Barcikowski, and B. Gökce, Phys. Chem. Chem. Phys. **21**, 18636 (2019).
84 L. Escobar-Alarcón, J. L. Iturbe-García, F. González-Zavala, D. A. Solis-Casados, R. Pérez-Hernández, and E. Haro-Poniatowski, Appl. Surf. Sci. **478**, 189 (2019).
85 J. H. Baxendale, and P. Wardman, Nature **230**, 449 (1971).
86 T. Zhang, Y. J. Lee, T. W. Kee, and P. F. Barbara, Chem. Phys. Lett. **403**, 257 (2005).
87 A. T. Healy, D. F. Underwood, S. Lipsky, and D. A. Blank, J. Chem. Phys. **123**, 051105 (2005).
88 A. T. Healy, S. Lipsky, and D. A. Blank, J. Chem. Phys. **127**, 214508 (2007).
89 A. T. Healy, S. Lipsky, and D. A. Blank, J. Chem. Phys. **129**, 234512 (2008).
90 T. Toigawa, M. Gohdo, K. Norizawa, T. Kondoh, K. Kan, J. Yang, and Y. Yoshida, Radiat. Phys. Chem. **123**, 73 (2016).
91 A. Saeki, N. Yamamoto, Y. Yoshida, and T. Kozawa, J. Phys. Chem. A **115**, 10166 (2011).
92 A. Saeki, T. Kozawa, Y. Yoshida, and S. Tagawa, J. Phys. Chem. A **108**, 1475 (2004).
93 I. A. Shkrob, M. C. Sauer, and A. D. Trifunac, J. Phys. Chem. **100**, 7237 (1996).
94 I. A. Shkrob, M. C. Sauer, and A. D. Trifunac, Stud. Phys. Theoret. Chemistry **87**, 175 (2001).
95 D. W. Werst, and A. D. Trifunac, J. Phys. Chem. **92**, 1093 (1988).
96 I. A. Shkrob, and M. C. Sauer, J. Phys. Chem. A **106**, 9120 (2002).
97 K. Hatanaka, T. Itoh, T. Asahi, N. Ichinose, S. Kawanishi, T. Sasuga, H. Fukumura, and H. Masuhara, J. Phys. Chem. A **103**, 11257 (1999).
98 K. Hatanaka, T. Itoh, T. Asahi, N. Ichinose, S. Kawanishi, T. Sasuga,

H. Fukumura, and H. Masuhara, Chem. Phys. Lett. **300**, 727 (1999).
99 K. Hatanaka, Y. Tsuboi, H. Fukumura, and H. Masuhara, J. Phys. Chem. B **106**, 3049 (2002).
100 K. Toyota, S. Nakashima, and T. Okada, Chem. Phys. Lett. **323**, 323 (2000).
101 D. Amans, M. Diouf, J. Lam, G. Ledoux, and C. Dujardin, J. Colloid Interface Sci. **489**, 114 (2017).
102 K. Toyota, T. Tanaka, S. Nishiwaki, S. Nakashima, and T. Okada, J. Photochem. Photobiol. A-Chem. **141**, 9 (2001).
103 A. Hu, J. Sanderson, A. A. Zaidi, C. Wang, T. Zhang, Y. Zhou, and W. W. Duley, Carbon **46**, 1823 (2008).
104 B. Tangeysh, J. H. Odhner, Y. Wang, B. B. Wayland, and R. J. Levis, J. Phys. Chem. A **123**, 6430 (2019).
105 T. Yatsuhashi, N. Uchida, and K. Nishikawa, Chem. Lett. **41**, 722 (2012).
106 S. L. Kuzmin, M. J. Wesolowski, and W. W. Duley, Appl. Opt. **52**, 8169 (2013).
107 T. Hamaguchi, T. Okamoto, K. Mitamura, K. Matsukawa, and T. Yatsuhashi, Bull. Chem. Soc. Jpn. **88**, 251 (2015).
108 A. A. Zaidi, A. Hu, D. E. Henneke, and W. W. Duley, Chem. Phys. Lett. **723**, 151 (2019).
109 Y. Sato, T. Kodama, H. Shiromaru, J. H. Sanderson, T. Fujino, Y. Wada, T. Wakabayashi, and Y. Achiba, Carbon **48**, 1673 (2010).
110 A. A. Zaidi, A. Hu, M. J. Wesolowski, X. Fu, J. H. Sanderson, Y. Zhou, and W. W. Duley, Carbon **48**, 2517 (2010).
111 M. J. Wesolowski, S. Kuzmin, B. Moores, B. Wales, R. Karimi, A. A. Zaidi, Z. Leonenko, J. H. Sanderson, and W. W. Duley, Carbon **49**, 625 (2011).
112 A. Ramadhan, M. Wesolowski, T. Wakabayashi, H. Shiromaru, T. Fujino, T. Kodama, W. Duley, and J. Sanderson, Carbon **118**, 680 (2017).
113 A. Haque, R. A. Al-Balushi, I. J. Al-Busaidi, M. S. Khan, and P. R. Raithby, Chem. Rev. **118**, 8474 (2018).
114 T. Nakamura, Y. Mochidzuki, and S. Sato, in *Synthesis of monodispersed DLC nanoparticles in intense optical field by femtosecond laser ablation of liquid benzene: 2007 Conference on Lasers and Electro-Optics (CLEO)* (Baltimore, 2007).
115 H. Yu, X. Li, X. Zeng, and Y. Lu, Chem. Commun. **52**, 819 (2016).
116 Z. Zhu, S. Wang, Y. Chang, D. Yu, and Y. Jiang, Carbon **105**, 416 (2016).
117 A. A. Astafiev, A. M. Shakhov, A. S. Kritchenkov, V. N. Khrustalev, D. V. Shepel, V. A. Nadtochenko, and A. G. Tskhovrebov, Dyes Pigm **188**, 109176 (2021).
118 T. Okamoto, K. Mitamura, T. Hamaguchi, K. Matsukawa, and T. Yatsuhashi, ChemPhysChem **18**, 1007 (2017).
119 T. Okamoto, E. Miyasaka, K. Mitamura, K. Matsukawa, and T. Yatsuhashi, J. Photochem. Photobiol. A-Chem. **344**, 178 (2017).
120 S. B. Ogale, P. P. Patil, D. M. Phase, Y. V. Bhandarkar, S. K. Kulkarni, S. Kulkarni, S. V. Ghaisas, S. M. Kanetkar, V. G. Bhide, and S. Guha, Phys. Rev. B **36**, 8237 (1987).
121 G. Marzun, H. Bönnemann, C. Lehmann, B. Spliethoff, C. Weidenthaler, and S. Barcikowski, ChemPhysChem **18**, 1175 (2017).
122 R. D. Sun, and T. Tsuji, Appl. Surf. Sci. **348**, 38 (2015).
123 A. R. Ziefuß, I. Haxhiaj, S. Müller, M. Gharib, O. Gridina, C. Rehbock, I. Chakraborty, B. Peng, M. Muhler, W. J. Parak, S. Barcikowski, and S. Reichenberger, J. Phys. Chem. C **124**, 20981 (2020).
124 S. Scaramuzza, S. Agnoli, and V. Amendola, Phys. Chem. Chem. Phys. **17**, 28076 (2015).
125 M. Lau, I. Haxhiaj, P. Wagener, R. Intartaglia, F. Brandi, J. Nakamura, and S. Barcikowski, Chem. Phys. Lett. **610-611**, 256 (2014).
126 D. A. Goncharova, T. S. Kharlamova, I. N. Lapin, and V. A. Svetlichnyi, J. Phys. Chem. C **123**, 21731 (2019).
127 B. Kumar, and R. K. Thareja, Phys. Plasmas **19**, 033516 (2012).
128 R. Streubel, S. Barcikowski, and B. Gökce, Opt. Lett. **41**, 1486 (2016).
129 J. Lam, D. Amans, F. Chaput, M. Diouf, G. Ledoux, N. Mary, K. Masenelli-Varlot, V. Motto-Ros, and C. Dujardin, Phys. Chem. Chem. Phys. **16**, 963 (2014).
130 J. Lam, V. Motto-Ros, D. Misiak, C. Dujardin, G. Ledoux, and D. Amans, Spectrochim. Acta Part B-Atomic Spectr. **101**, 86 (2014).
131 A. De Giacomo, M. Dell'Aglio, A. Casavola, G. Colonna, O. De Pascale, and M. Capitelli, Anal. Bioanal. Chem. **385**, 303 (2006).
132 S. Reich, J. Göttlicher, A. Ziefuss, R. Streubel, A. Letzel, A. Menzel, O. Mathon, S. Pascarelli, T. Baumbach, M. Zuber, B. Gökce, S. Barcikowski, and A. Plech, Nanoscale **12**, 14011 (2020).
133 P. Camarda, L. Vaccaro, F. Messina, and M. Cannas, Appl. Phys. Lett. **107**, 013103 (2015).
134 M. S. Yeh, Y. S. Yang, Y. P. Lee, H. F. Lee, Y. H. Yeh, and C. S. Yeh, J. Phys. Chem. B **103**, 6851 (1999).
135 M. Kawasaki, J. Phys. Chem. C **115**, 5165 (2011).
136 C. A. Schaumberg, M. Wollgarten, and K. Rademann, J. Phys. Chem. A **118**, 8329 (2014).
137 M. Kawasaki, and N. Nishimura, J. Phys. Chem. C **112**, 15647 (2008).
138 H. Wang, A. Pyatenko, K. Kawaguchi, X. Li, Z. Swiatkowska-Warkocka, and N. Koshizaki, Angew. Chem. Int. Ed. **49**, 6361 (2010).
139 H. Wang, K. Kawaguchi, A. Pyatenko, X. Li, Z. Swiatkowska-Warkocka, Y. Katou, and N. Koshizaki, Chem. Eur. J. **18**, 163 (2012).
140 Z. Swiatkowska-Warkocka, A. Pyatenko, Y. Shimizu, M. Perzanowski, A. Zarzycki, B. R. Jany, and M. Marszalek, Nanomaterials **8**, 790 (2018).
141 D. D'Angelo, S. Filice, M. Miritello, C. Bongiorno, E. Fazio, F. Neri, G. Compagnini, and S. Scalese, Phys. Chem. Chem. Phys. **20**, 10292 (2018).
142 Z. Swiatkowska-Warkocka, K. Kawaguchi, H. Wang, Y. Katou, and N. Koshizaki, Nanoscale Res. Lett. **6**, 226 (2011).
143 Y. Ishikawa, N. Koshizaki, and S. Sakaki, J. Phys. Chem. C **123**, 24934 (2019).
144 K. Suehara, R. Takai, Y. Ishikawa, N. Koshizaki, K. Omura, H. Nagata, and Y. Yamauchi, ChemPhysChem **22**, 675 (2021).
145 M. Lau, and S. Barcikowski, Appl. Surf. Sci. **348**, 22 (2015).
146 H. Zeng, S. Yang, and W. Cai, J. Phys. Chem. C **115**, 5038 (2011).
147 M. Lau, S. Reichenberger, I. Haxhiaj, S. Barcikowski, and A. M. Müller, ACS Appl. Energy Mater. **1**, 5366 (2018).
148 Y. Takeda, and F. Mafuné, Chem. Phys. Lett. **599**, 110 (2014).
149 R. Kihara, A. Shigetaka, T. Isshiki, H. Wada, S. Yamamuro, and T. Asahi, Chem. Lett. **49**, 413 (2020).
150 A. Balati, S. Tek, K. Nash, and H. Shipley, J. Colloid Interface Sci. **541**, 234 (2019).
151 J. Lam, D. Amans, C. Dujardin, G. Ledoux, and A. R. Allouche, J. Phys. Chem. A **119**, 8944 (2015), arXiv: 1707.08434.
152 R. García-Calzada, M. Rodio, K. Bagga, R. Intartaglia, P. Bianchini, V. S. Chirvony, and J. P. Martínez-Pastor, RSC Adv. **5**, 50604 (2015).
153 S. H. Lee, H. J. Jung, S. J. Lee, J. Theerthagiri, T. H. Kim, and M. Y. Choi, Appl. Surf. Sci. **506**, 145006 (2020).
154 D. Zhang, C. Zhang, J. Liu, Q. Chen, X. Zhu, and C. Liang, ACS Appl. Nano Mater. **2**, 28 (2019).
155 J. S. Golightly, and A. W. Castleman, J. Phys. Chem. B **110**, 19979 (2006).
156 A. De Bonis, A. Santagata, A. Galasso, A. Laurita, and R. Teghil, J. Colloid Interface Sci. **489**, 76 (2017).
157 V. Amendola, P. Riello, and M. Meneghetti, J. Phys. Chem. C **115**, 5140 (2011).
158 A. Kanitz, J. S. Hoppius, M. Del Mar Sanz, M. Maicas, A. Ostendorf, and E. L. Gurevich, ChemPhysChem **18**, 1155 (2017).
159 D. Zhang, W. Choi, Y. Oshima, U. Wiedwald, S. H. Cho, H. P. Lin, Y. K. Li, Y. Ito, and K. Sugioka, Nanomaterials **8**, 631 (2018).
160 H. J. Jung, and M. Y. Choi, J. Phys. Chem. C **118**, 14647 (2014).
161 H. J. Jung, and M. Y. Choi, Appl. Surf. Sci. **457**, 1050 (2018).
162 N. G. Semaltianos, E. Hendry, H. Chang, and M. L. Wears, RSC Adv. **4**, 50406 (2014).
163 M. Curcio, A. De Bonis, A. Santagata, A. Galasso, and R. Teghil, Opt. Laser Tech. **138**, 106916 (2021).
164 H. Zhang, J. Liu, Z. Tian, Y. Ye, Y. Cai, C. Liang, and K. Terabe, Carbon **100**, 590 (2016).
165 S. Yang, W. Cai, H. Zhang, H. Zeng, and Y. Lei, J. Phys. Chem. C

115, 7279 (2011).
166 H. Zhang, C. Liang, J. Liu, Z. Tian, and G. Shao, Carbon **55**, 108 (2013).
167 D. Zhang, W. Choi, J. Jakobi, M. R. Kalus, S. Barcikowski, S. H. Cho, and K. Sugioka, Nanomaterials **8**, 529 (2018).
168 S. A. Davari, J. L. Gottfried, C. Liu, E. L. Ribeiro, G. Duscher, and D. Mukherjee, Appl. Surf. Sci. **473**, 156 (2019).
169 P. G. Kuzmin, G. A. Shafeev, V. V. Bukin, S. V. Garnov, C. Farcau, R. Carles, B. Warot-Fontrose, V. Guieu, and G. Viau, J. Phys. Chem. C **114**, 15266 (2010).
170 R. Intartaglia, K. Bagga, A. Genovese, A. Athanassiou, R. Cingolani, A. Diaspro, and F. Brandi, Phys. Chem. Chem. Phys. **14**, 15406 (2012).
171 K. Abderrafi, R. García-Calzada, J. F. Sanchez-Royo, V. S. Chirvony, S. Agouram, R. Abargues, R. Ibáñez, and J. P. Martínez-Pastor, J. Phys. D-Appl. Phys. **46**, 135301 (2013).
172 D. Zhang, and K. Sugioka, Opto-Electron. Adv. **2**, 19000201 (2019).
173 F. Davodi, E. Mühlhausen, D. Settipani, E. L. Rautama, A. P. Honkanen, S. Huotari, G. Marzun, P. Taskinen, and T. Kallio, J. Colloid Interface Sci. **556**, 180 (2019).
174 N. Lasemi, C. Rentenberger, R. Pospichal, A. S. Cherevan, M. Pfaffeneder-Kmen, G. Liedl, and D. Eder, Appl. Phys. A **125**, 544 (2019).
175 S. Dewan, J. H. Odhner, K. M. Tibbetts, S. Afsari, R. J. Levis, and E. Borguet, J. Mater. Chem. C **4**, 6894 (2016).
176 R. Lahoz, A. Naghilou, W. Kautek, and O. Bomati-Miguel, Appl. Surf. Sci. **511**, 145438 (2020).
177 S. Yang, H. Zeng, H. Zhao, H. Zhang, and W. Cai, J. Mater. Chem. **21**, 4432 (2011).
178 N. Shirahata, M. R. Linford, S. Furumi, L. Pei, Y. Sakka, R. J. Gates, and M. C. Asplund, Chem. Commun. **45**, 4684 (2009).
179 Y. Xin, T. Kitasako, M. Maeda, and K. Saitow, Chem. Phys. Lett. **674**, 90 (2017).
180 Z. Yuan, T. Nakamura, S. Adachi, and K. Matsuishi, Nanoscale **9**, 1193 (2017).
181 D. Tan, Z. Ma, B. Xu, Y. Dai, G. Ma, M. He, Z. Jin, and J. Qiu, Phys. Chem. Chem. Phys. **13**, 20255 (2011).
182 H. L. Hao, W. S. Wu, Y. Zhang, L. K. Wu, and W. Z. Shen, Nanotechnology **27**, 325702 (2016).
183 J. Wang, Y. Zhang, H. Hao, and W. Shen, Nanotechnology **30**, 015705 (2019).
184 S. Yang, W. Cai, H. Zeng, and X. Xu, J. Mater. Chem. **19**, 7119 (2009).
185 L. Franzel, M. F. Bertino, Z. J. Huba, and E. E. Carpenter, Appl. Surf. Sci. **261**, 332 (2012).
186 O. Havelka, M. Cvek, M. Urbánek, D. Łukowiec, D. Jašíková, M. Kotek, M. Černík, V. Amendola, and R. Torres-Mendieta, Nanomaterials **11**, 1538 (2021).
187 S. I. Dolgaev, A. V. Simakin, V. V. Voronov, G. A. Shafeev, and F. Bozon-Verduraz, Appl. Surf. Sci. **186**, 546 (2002).
188 N. G. Semaltianos, J. M. Friedt, R. Chassagnon, V. Moutarlier, V. Blondeau-Patissier, G. Combe, M. Assoul, and G. Monteil, J. Appl. Phys. **119**, 204903 (2016).
189 M. Madrigal-Camacho, A. R. Vilchis-Nestor, M. Camacho-López, and M. A. Camacho-López, Diamond Relat. Mater. **82**, 63 (2018).
190 X. Zhang, D. Zhang, D. Tan, Y. Xian, X. Liu, and J. Qiu, Chem. Mater. **32**, 10025 (2020).
191 A. De Bonis, M. Curcio, A. Santagata, A. Galasso, and R. Teghil, Nanomaterials **10**, 145 (2020).
192 N. V. Tarasenko, A. V. Butsen, and A. A. Nevar, Appl. Phys. A **93**, 837 (2008).
193 B. Feizi Mohazzab, B. Jaleh, O. Kakuee, and A. Fattah-alhosseini, Appl. Surf. Sci. **478**, 623 (2019).
194 D. Zhang, B. Ranjan, T. Tanaka, and K. Sugioka, ACS Appl. Nano Mater. **3**, 1855 (2020).
195 M. C. Gonzalez, and A. M. Braun, Res. Chem. Intermed. **21**, 837 (1995).
196 Standard Reduction Potentials by Value (2021), online accessed 2021-09-08, https://chem.libretexts.org/@go/page/2190.
197 C. Zhao, S. Qu, J. Qiu, and C. Zhu, J. Mater. Res. **18**, 1710 (2003).
198 Y. Herbani, T. Nakamura, and S. Sato, J. Phys. Chem. C **115**, 21592 (2011).
199 P. H. D. Ferreira, M. G. Vivas, L. De Boni, D. S. dos Santos, D. T. Balogh, L. Misoguti, and C. R. Mendonca, Opt. Express **20**, 518 (2012).
200 W. E. Lu, M. L. Zheng, W. Q. Chen, Z. S. Zhao, and X. M. Duan, Phys. Chem. Chem. Phys. **14**, 11930 (2012).
201 Y. Herbani, T. Nakamura, and S. Sato, J. Colloid Interface Sci. **375**, 78 (2012).
202 T. Nakamura, Y. Herbani, D. Ursescu, R. Banici, R. V. Dabu, and S. Sato, AIP Adv. **3**, 082101 (2013).
203 R. A. de Matos, T. da Silva Cordeiro, R. E. Samad, N. D. Vieira, and L. C. Courrol, Appl. Phys. A **109**, 737 (2012).
204 Muttaqin, T. Nakamura, and S. Sato, Appl. Phys. A **120**, 881 (2015).
205 H. Belmouaddine, M. Shi, L. Sanche, and D. Houde, Phys. Chem. Chem. Phys. **20**, 23403 (2018).
206 L. M. Frias Batista, V. K. Meader, K. Romero, K. Kunzler, F. Kabir, A. Bullock, and K. M. Tibbetts, J. Phys. Chem. B **123**, 7204 (2019).
207 T. Uwada, S. F. Wang, T. H. Liu, and H. Masuhara, J. Photochem. Photobiol. A-Chem. **346**, 177 (2017).
208 T. Okamoto, T. Nakamura, K. Sakota, and T. Yatsuhashi, Langmuir **35**, 12123 (2019).
209 K. Kurihara, J. Kizling, P. Stenius, and J. H. Fendler, J. Am. Chem. Soc. **105**, 2574 (1983).
210 S. Eustis, H. Y. Hsu, and M. A. El-Sayed, J. Phys. Chem. B **109**, 4811 (2005).
211 G. R. Dey, A. K. El Omar, J. A. Jacob, M. Mostafavi, and J. Belloni, J. Phys. Chem. A **115**, 383 (2011).
212 M. Harada, and S. Kizaki, Cryst. Growth Des. **16**, 1200 (2016).
213 M. A. Watzky, and R. G. Finke, J. Am. Chem. Soc. **119**, 10382 (1997).
214 M. Zayats, R. Baron, I. Popov, and I. Willner, Nano Lett. **5**, 21 (2005).
215 S. Besner, A. V. Kabashin, F. M. Winnik, and M. Meunier, Appl. Phys. A **93**, 955 (2008).
216 M. Kalyva, G. Bertoni, A. Milionis, R. Cingolani, and A. Athanassiou, Microsc. Res. Tech. **73**, 937 (2010).
217 N. Mirghassemzadeh, M. Ghamkhari, and D. Dorranian, Soft Nanosci. Lett. **03**, 101 (2013).
218 S. Besner, and M. Meunier, J. Phys. Chem. C **114**, 10403 (2010).
219 Q. X. Liu, C. X. Wang, W. Zhang, and G. W. Wang, Chem. Phys. Lett. **382**, 1 (2003).
220 D. Oron, and Y. Silberberg, Opt. Express **13**, 9903 (2005).
221 A. R. Ziefuß, S. Barcikowski, and C. Rehbock, Langmuir **35**, 6630 (2019).
222 C. Rehbock, V. Merk, L. Gamrad, R. Streubel, and S. Barcikowski, Phys. Chem. Chem. Phys. **15**, 3057 (2013).
223 S. Berciaud, L. Cognet, P. Tamarat, and B. Lounis, Nano Lett. **5**, 515 (2005), arXiv: 0704.3814.
224 K. B. Male, J. Li, C. C. Bun, S. C. Ng, and J. H. T. Luong, J. Phys. Chem. C **112**, 443 (2008).
225 J. Piella, N. G. Bastús, and V. Puntes, Chem. Mater. **28**, 1066 (2016).
226 J. A. LaVerne, and S. M. Pimblott, J. Phys. Chem. **95**, 3196 (1991).
227 Y. Herbani, T. Nakamura, and S. Sato, J. Phys.-Conf. Ser. **817**, 012048 (2017).
228 J. H. Baxendale, and P. Wardman, J. Chem. Soc. Faraday Trans. 1 **69**, 584 (1973).
229 J. P. Sylvestre, S. Poulin, A. V. Kabashin, E. Sacher, M. Meunier, and J. H. T. Luong, J. Phys. Chem. B **108**, 16864 (2004).
230 S. J. Kim, and D. J. Jang, Appl. Phys. Lett. **86**, 033112 (2005).
231 A. Poletti, G. Fracasso, G. Conti, R. Pilot, and V. Amendola, Nanoscale **7**, 13702 (2015).
232 D. He, S. Garg, and T. D. Waite, Langmuir **28**, 10266 (2012).
233 J. P. Abid, A. W. Wark, P. F. Brevet, and H. H. Girault, Chem. Commun. **38**, 792 (2002).
234 T. Nakamura, H. Magara, Y. Herbani, and S. Sato, Appl. Phys. A **104**, 1021 (2011).
235 C. M. Nguyen, L. M. Frias Batista, M. G. John, C. J. Rodrigues, and

K. M. Tibbetts, J. Phys. Chem. B **125**, 907 (2021).
236 I. Texier, S. Rémita, P. Archirel, and M. Mostafavi, J. Phys. Chem. **100**, 12472 (1996).
237 D. V. Goia, J. Mater. Chem. **14**, 451 (2004).
238 M. S. I. Sarker, T. Nakamura, Y. Herbani, and S. Sato, Appl. Phys. A **110**, 145 (2012).
239 L. M. Frias Batista, K. Kunzler, M. G. John, B. Clark, A. Bullock, J. Ferri, B. F. Gupton, and K. M. Tibbetts, Appl. Surf. Sci. **557**, 149811 (2021).
240 G. Fan, S. Qu, Q. Wang, C. Zhao, L. Zhang, and Z. Li, J. Appl. Phys. **109**, 023102 (2011).
241 G. Fan, S. Ren, S. Qu, Z. Guo, Q. Wang, Y. Wang, and R. Gao, Opt. Commun. **295**, 219 (2013).
242 M. S. I. Sarker, T. Nakamura, S. Kameoka, Y. Hayasaka, S. Yin, and S. Sato, RSC Adv. **9**, 38882 (2019).
243 M. Saeki, D. Matsumura, T. Yomogida, T. Taguchi, T. Tsuji, H. Saitoh, and H. Ohba, J. Phys. Chem. C **123**, 817 (2019).
244 S. Y. Troitskii, A. L. Chuvilin, D. I. Kochubei, B. N. Novgorodov, V. N. Kolomiichuk, and V. A. Likholobov, Russ. Chem. Bull. **44**, 1822 (1995).
245 F. Kettemann, M. Wuithschick, G. Caputo, R. Kraehnert, N. Pinna, K. Rademann, and J. Polte, CrystEngComm **17**, 1865 (2015).
246 L. A. Koroleva, N. D. Shikina, P. G. Kolodina, A. V. Zotov, B. R. Tagirov, Y. V. Shvarov, V. A. Volchenkova, and Y. K. Shazzo, Geochem. Int. **50**, 853 (2012).
247 S. Z. Mortazavi, P. Parvin, A. Reyhani, A. N. Golikand, and S. Mirershadi, J. Phys. Chem. C **115**, 5049 (2011).
248 M. Boutinguiza, M. Meixus, J. del Val, A. Riveiro, R. Comesaña, F. Lusquiños, and J. Pou, Phys. Procedia **83**, 36 (2016).
249 G. Cristoforetti, E. Pitzalis, R. Spiniello, R. Ishak, and M. Muniz-Miranda, J. Phys. Chem. C **115**, 5073 (2011).
250 M. P. Navas, and R. K. Soni, Appl. Surf. Sci. **390**, 718 (2016).
251 M. Boutinguiza, R. Comesaña, F. Lusquiños, A. Riveiro, J. del Val, and J. Pou, Appl. Surf. Sci. **302**, 19 (2014).
252 A. De Bonis, R. D'Orsi, M. Funicello, P. Lupattelli, A. Santagata, R. Teghil, and L. Chiummiento, Catal. Commun. **100**, 164 (2017).
253 G. Marzun, J. Nakamura, X. Zhang, S. Barcikowski, and P. Wagener, Appl. Surf. Sci. **348**, 75 (2015).
254 M. Cueto, M. Sanz, M. Oujja, F. Gámez, B. Martínez-Haya, and M. Castillejo, J. Phys. Chem. C **115**, 22217 (2011).
255 S. Kohsakowski, R. Streubel, I. Radev, V. Peinecke, S. Barcikowski, G. Marzun, and S. Reichenberger, Appl. Surf. Sci. **467-468**, 486 (2019).
256 A. R. Ziefuß, S. Reichenberger, C. Rehbock, I. Chakraborty, M. Gharib, W. J. Parak, and S. Barcikowski, J. Phys. Chem. C **122**, 22125 (2018).
257 T. Nishi, Y. Hayasaka, T. Nakamura, T. Morikawa, and S. Sato, Appl. Surf. Sci. **457**, 1044 (2018).
258 E. Ye, B. Liu, and W. Y. Fan, Chem. Mater. **19**, 3845 (2007).
259 J. B. Park, S. H. Jeong, M. S. Jeong, J. Y. Kim, and B. K. Cho, Carbon **46**, 1369 (2008).
260 Y. Hayasaki, T. Fukuda, T. Hasumura, and T. Maekawa, Adv. Nat. Sci-Nanosci. Nanotechnol. **3**, 035010 (2012).
261 S. H. Huh, and A. Nakajima, J. Appl. Phys. **99**, 064302 (2006).
262 C. Famiglietti, and E. J. Baerends, Chem. Phys. **62**, 407 (1981).
263 U. Ray, H. Q. Hou, Z. Zhang, W. Schwarz, and M. Vernon, J. Chem. Phys. **90**, 4248 (1989).
264 S. J. Blanksby, and G. B. Ellison, Acc. Chem. Res. **36**, 255 (2003).
265 S. Moussa, G. Atkinson, and M. S. El-Shall, J. Nanopart. Res. **15**, 1470 (2013).
266 T. Okamoto, T. Nakamura, R. Kihara, T. Asahi, K. Sakota, and T. Yatsuhashi, ChemPhysChem **19**, 2480 (2018).
267 T. Okamoto, T. Nakamura, Y. O. Tahara, M. Miyata, K. Sakota, and T. Yatsuhashi, Chem. Lett. **49**, 75 (2020).
268 Y. Horikawa, T. Okamoto, T. Nakamura, Y. O. Tahara, M. Miyata, S. Ikeda, K. Sakota, and T. Yatsuhashi, Chem. Phys. Lett. **750**, 137504 (2020).
269 M. J. Wesolowski, S. Kuzmin, B. Wales, J. H. Sanderson, and W. W. Duley, J. Mater. Sci. **48**, 6212 (2013).
270 A. Nag, L. M. Frias Batista, and K. M. Tibbetts, Nanomaterials **11**, 814 (2021).
271 Y. Herbani, T. Nakamura, and S. Sato, J. Nanomater. **2010**, 1 (2010).
272 J. L. H. Chau, C. Y. Chen, M. C. Yang, K. L. Lin, S. Sato, T. Nakamura, C. C. Yang, and C. W. Cheng, Mater. Lett. **65**, 804 (2011).
273 T. Nakamura, Y. Herbani, and S. Sato, J. Nanopart. Res. **14**, 785 (2012).
274 T. Nakamura, and S. Sato, J. Nanosci. Nanotechnol. **15**, 426 (2015).
275 T. Nakamura, Y. Yamazaki, and S. Sato, KONA Powder Part. J. 2022002 (2022).
276 M. S. I. Sarker, T. Nakamura, Y. Herbani, and S. Sato, Appl. Phys. A **110**, 145 (2013).
277 M. S. I. Sarker, T. Nakamura, and S. Sato, J. Mater. Res. **29**, 856 (2014).
278 M. S. I. Sarker, T. Nakamura, and S. Sato, J. Nanopart. Res. **17**, 259 (2015).
279 J. L. H. Chau, C. Y. Chen, and C. C. Yang, Arabian J. Chem. **10**, S1395 (2017).
280 B. N. Wanjala, J. Luo, B. Fang, D. Mott, and C. J. Zhong, J. Mater. Chem. **21**, 4012 (2011).
281 A. Cao, R. Lu, and G. Veser, Phys. Chem. Chem. Phys. **12**, 13499 (2010).
282 Y. Hayasaki, T. Hasumura, T. Fukuda, Y. Nagaoka, T. Ukai, S. Iwai, T. Uchida, and T. Maekawa, Heliyon **2**, e00171 (2016).
283 R. Torres-Mendieta, O. Havelka, M. Urbánek, M. Cvek, S. Wacławek, V. V. T. Padil, D. Jašíková, M. Kotek, and M. Černík, Appl. Surf. Sci. **469**, 1007 (2019).
284 M. Sakamoto, M. Fujistuka, and T. Majima, J. Photochem. Photobiol. C-Photochem. Rev. **10**, 33 (2009).
285 P. S. Rao, and E. Hayon, J. Am. Chem. Soc. **96**, 1287 (1974).
286 I. N. Saraeva, N. V. Luong, S. I. Kudryashov, A. A. Rudenko, R. A. Khmelnitskiy, A. L. Shakhmin, A. Y. Kharin, A. A. Ionin, D. A. Zayarny, D. H. Tung, P. V. Duong, and P. H. Minh, J. Photochem. Photobiol. A-Chem. **360**, 125 (2018).
287 M. G. John, and K. M. Tibbetts, Appl. Surf. Sci. **475**, 1048 (2019).
288 F. Lin, J. Yang, S. H. Lu, K. Y. Niu, Y. Liu, J. Sun, and X. W. Du, J. Mater. Chem. **20**, 1103 (2010).
289 D. Ettel, O. Havelka, S. Isik, D. Silvestri, S. Wacławek, M. Urbánek, V. V. T. Padil, M. Černík, F. Yalcinkaya, and R. Torres-Mendieta, Appl. Surf. Sci. **564**, 150471 (2021).
290 H. Zeng, C. Zhao, J. Qiu, Y. Yang, and G. Chen, J. Cryst. Growth **300**, 519 (2007).
291 N. Mintcheva, P. Srinivasan, J. B. B. Rayappan, A. A. Kuchmizhak, S. Gurbatov, and S. A. Kulinich, Appl. Surf. Sci. **507**, 145169 (2020).
292 M. K. Das, J. A. Bobb, A. A. Ibrahim, A. Lin, K. M. AbouZeid, and M. S. El-Shall, ACS Appl. Mater. Interfaces **12**, 23844 (2020).
293 S. O. Gurbatov, E. Modin, V. Puzikov, P. Tonkaev, D. Storozhenko, A. Sergeev, N. Mintcheva, S. Yamaguchi, N. N. Tarasenka, A. Chuvilin, S. Makarov, S. A. Kulinich, and A. A. Kuchmizhak, ACS Appl. Mater. Interfaces **13**, 6522 (2021).
294 J. A. Bobb, A. A. Ibrahim, and M. S. El-Shall, ACS Appl. Nano Mater. **1**, 4852 (2018).
295 J. Lv, S. Wu, Z. Tian, Y. Ye, J. Liu, and C. Liang, J. Mater. Chem. A **7**, 12627 (2019).
296 Y. Yu, L. Yan, M. Yue, and H. Xu, R. Soc. Open Sci. **5**, 171436 (2018).
297 M. Yue, J. Si, L. Yan, Y. Yu, and X. Hou, Opt. Mater. Express **8**, 698 (2018).
298 Y. Yu, L. Yan, J. Si, Y. Xu, and X. Hou, J. Phys. Chem. Solids **132**, 116 (2019).
299 M. Sygletou, P. Tzourmpakis, C. Petridis, D. Konios, C. Fotakis, E. Kymakis, and E. Stratakis, J. Mater. Chem. A **4**, 1020 (2016).
300 S. Moussa, V. Abdelsayed, and M. Samy El-Shall, Chem. Phys. Lett. **510**, 179 (2011).
301 S. Moussa, G. Atkinson, M. SamyEl-Shall, A. Shehata, K. M. AbouZeid, and M. B. Mohamed, J. Mater. Chem. **21**, 9608 (2011).
302 S. Moussa, A. R. Siamaki, B. F. Gupton, and M. S. El-Shall, ACS Catal. **2**, 145 (2012).

303 L. H. Chen, H. T. Shen, W. H. Chang, I. Khalil, S. Y. Liao, W. A. Yehye, S. C. Liu, C. C. Chu, and V. K. S. Hsiao, Nanomaterials **10**, 1985 (2020).
304 Y. Peng, J. Cao, J. Yang, W. Yang, C. Zhang, X. Li, R. A. W. Dryfe, L. Li, I. A. Kinloch, and Z. Liu, Adv. Funct. Mater. **30**, 2001756 (2020).
305 Y. Peng, J. Cao, Y. Sha, W. Yang, L. Li, and Z. Liu, Light Sci. Appl. **10**, 168 (2021).
306 E. Jiménez, K. Abderrafi, R. Abargues, J. L. Valdés, and J. P. Martínez-Pastor, Langmuir **26**, 7458 (2010).
307 P. Liu, H. Chen, H. Wang, J. Yan, Z. Lin, and G. Yang, J. Phys. Chem. C **119**, 1234 (2015).
308 S. Yang, W. Cai, G. Liu, H. Zeng, and P. Liu, J. Phys. Chem. C **113**, 6480 (2009).
309 J. R. González-Castillo, E. Rodriguez, E. Jimenez-Villar, D. Rodríguez, I. Salomon-García, G. F. de Sá, T. García-Fernández, D. B. Almeida, C. L. Cesar, R. Johnes, and J. C. Ibarra, Nanoscale Res. Lett. **10**, 399 (2015).
310 V. A. Ermakov, E. Jimenez-Villar, J. M. C. Silva Filho, E. Yassitepe, N. V. V. Mogili, F. Iikawa, G. F. de Sá, C. L. Cesar, and F. C. Marques, Langmuir **33**, 2257 (2017).
311 A. M. Mostafa, and E. A. Mwafy, J. Mater. Res. Tech. **9**, 3241 (2020).
312 A. M. Mostafa, S. A. Yousef, W. H. Eisa, M. A. Ewaida, and E. A. Al-Ashkar, Appl. Phys. A **123**, 774 (2017).
313 Z. Sheykhifard, M. Ranjbar, H. Farrokhpour, and H. Salamati, J. Phys. Chem. C **119**, 9534 (2015).
314 H. Bao, Y. Wang, H. Zhang, Q. Zhao, G. Liu, and W. Cai, J. Colloid Interface Sci. **489**, 92 (2017).
315 H. Bao, H. Zhang, L. Zhou, G. Liu, Y. Li, and W. Cai, Langmuir **33**, 12934 (2017).
316 A. Chemin, J. Lam, G. Laurens, F. Trichard, V. Motto-Ros, G. Ledoux, V. Jarý, V. Laguta, M. Nikl, C. Dujardin, and D. Amans, Nanoscale Adv. **1**, 3963 (2019).
317 C. Chen, D. Wu, Z. Li, R. Zhang, C. Kuai, X. Zhao, C. Dong, S. Qiao, H. Liu, and X. Du, Adv. Energy Mater. **9**, 1803913 (2019).
318 L. Shang, J. Q. Wang, C. Q. Cheng, Y. Zhang, F. F. Zhang, Y. M. Xie, J. D. Lu, J. Mao, Q. J. Guo, C. K. Dong, H. Liu, and X. W. Du, J. Alloys Compd. **874**, 159909 (2021).
319 F. F. Zhang, C. Q. Cheng, J. Q. Wang, L. Shang, Y. Feng, Y. Zhang, J. Mao, Q. J. Guo, Y. M. Xie, C. K. Dong, Y. H. Cheng, H. Liu, and X. W. Du, ACS Energy Lett. **6**, 1588 (2021).
320 D. Poondi, T. Dobbins, and J. Singh, J. Mater. Sci. **35**, 6237 (2000).
321 S. Yoon, K. S. Yoo, and J. Kim, Appl. Sci. **11**, 1394 (2021).
322 H. Park, D. A. Reddy, Y. Kim, S. Lee, R. Ma, M. Lim, and T. K. Kim, Appl. Surf. Sci. **401**, 314 (2017).
323 Y. Yu, J. Theerthagiri, S. J. Lee, G. Muthusamy, M. Ashokkumar, and M. Y. Choi, Chem. Eng. J. **411**, 128486 (2021).
324 A. M. Mostafa, E. A. Mwafy, N. S. Awwad, and H. A. Ibrahium, J. Mater. Sci.-Mater. Electron. **32**, 11978 (2021).
325 S. Hu, M. Tian, E. L. Ribeiro, G. Duscher, and D. Mukherjee, J. Power Sources **306**, 413 (2016).
326 S. Hu, G. Goenaga, C. Melton, T. A. Zawodzinski, and D. Mukherjee, Appl. Catal. B-Environ. **182**, 286 (2016).
327 S. Hu, K. Cheng, E. L. Ribeiro, K. Park, B. Khomami, and D. Mukherjee, Catal. Sci. Technol. **7**, 2074 (2017).
328 A. M. Darwish, W. H. Eisa, A. A. Shabaka, and M. H. Talaat, Spectr. Lett. **48**, 638 (2015).
329 A. M. Darwish, W. H. Eisa, A. A. Shabaka, and M. H. Talaat, Spectrochim. Acta Part A-Mol. Biomol. Spectr. **153**, 315 (2016).
330 A. M. Mostafa, E. A. Mwafy, and M. S. Hasanin, Optics Laser Tech. **121**, 105824 (2020).
331 S. S. Naik, S. J. Lee, J. Theerthagiri, Y. Yu, and M. Y. Choi, J. Hazard. Mater. **418**, 126269 (2021).
332 C. W. Roske, J. W. Lefler, and A. M. Müller, J. Colloid Interface Sci. **489**, 68 (2017).
333 P. Liu, Y. Liang, X. Lin, C. Wang, and G. Yang, ACS Nano **5**, 4748 (2011).
334 Y. Liang, P. Liu, H. B. Li, and G. W. Yang, Cryst. Growth Des. **12**, 4487 (2012).
335 Y. Liang, P. Liu, H. B. Li, and G. W. Yang, CrystEngComm **14**, 3291 (2012).
336 H. Zhang, J. Liu, Y. Ye, Z. Tian, and C. Liang, Phys. Chem. Chem. Phys. **15**, 5684 (2013).
337 B. M. Hunter, J. D. Blakemore, M. Deimund, H. B. Gray, J. R. Winkler, and A. M. Müller, J. Am. Chem. Soc. **136**, 13118 (2014).
338 B. M. Hunter, W. Hieringer, J. R. Winkler, H. B. Gray, and A. M. Müller, Energy Environ. Sci. **9**, 1734 (2016).
339 H. Lee, D. A. Reddy, Y. Kim, S. Y. Chun, R. Ma, D. P. Kumar, J. K. Song, and T. K. Kim, ACS Sustain. Chem. Eng. **6**, 16734 (2018).
340 M. G. John, and K. M. Tibbetts, Appl. Surf. Sci. **510**, 145037 (2020).
341 M. G. John, and K. M. Tibbetts, J. Phys. Chem. C **124**, 13273 (2020).
342 E. L. Ribeiro, S. A. Davari, S. Hu, D. Mukherjee, and B. Khomami, Mater. Chem. Front. **3**, 1302 (2019).
343 E. L. Ribeiro, E. M. Davis, M. Mokhtarnejad, S. Hu, D. Mukherjee, and B. Khomami, Catal. Sci. Technol. **11**, 3002 (2021).
344 F. Ataei, D. Dorranian, and N. Motakef-Kazemi, J Theor Appl Phys **14**, 1 (2020).
345 F. Ataei, D. Dorranian, and N. Motakef-Kazemi, J Mater Sci-Mater Electron **32**, 3819 (2021).
346 Z. Q. Huang, M. H. Hong, T. B. M. Do, and Q. Y. Lin, Appl. Phys. A **93**, 159 (2008).
347 X. Xie, X. Huang, W. Jiang, X. Wei, W. Hu, and Q. Ren, Optics Laser Tech. **89**, 59 (2017).
348 J. M. Seo, K. K. Kwon, K. Y. Song, C. N. Chu, and S. H. Ahn, Materials **13**, 2977 (2020).
349 W. E. Lu, Y. L. Zhang, M. L. Zheng, Y. P. Jia, J. Liu, X. Z. Dong, Z. S. Zhao, C. B. Li, Y. Xia, T. C. Ye, and X. M. Duan, Opt. Mater. Express **3**, 1660 (2013).
350 Y. Fujita, R. Aubert, P. Walke, H. Yuan, B. Kenens, T. Inose, C. Steuwe, S. Toyouchi, B. Fortuni, M. Chamtouri, K. P. F. Janssen, S. De Feyter, M. B. J. Roeffaers, and H. Uji-I, Nanoscale **9**, 13025 (2017).
351 M. Y. Bashouti, A. V. Povolotckaia, A. V. Povolotskiy, S. P. Tunik, S. H. Christiansen, G. Leuchs, and A. A. Manshina, RSC Adv. **6**, 75681 (2016).
352 A. Povolotckaia, D. Pankin, Y. Petrov, A. Vasileva, I. Kolesnikov, G. Sarau, S. Christiansen, G. Leuchs, and A. Manshina, J. Mater. Sci. **54**, 8177 (2019).
353 A. Vasileva, S. Haschke, V. Mikhailovskii, A. Gitlina, J. Bachmann, and A. Manshina, Nano-Struct. Nano-Objects **24**, 100547 (2020).
354 D. V. Mamonova, A. A. Vasileva, Y. V. Petrov, D. V. Danilov, I. E. Kolesnikov, A. A. Kalinichev, J. Bachmann, and A. A. Manshina, Materials **14**, 10 (2021).
355 C. H. Lin, L. Jiang, Y. H. Chai, H. Xiao, S. J. Chen, and H. L. Tsai, Opt. Express **17**, 21581 (2009).
356 L. Jiang, D. Ying, X. Li, and Y. Lu, Opt. Lett. **37**, 3648 (2012).
357 N. Zhang, X. Li, L. Jiang, X. Shi, C. Li, and Y. Lu, Opt. Lett. **38**, 3558 (2013).
358 Q. Yang, X. Li, L. Jiang, N. Zhang, G. Zhang, X. Shi, K. Zhang, J. Hu, and Y. Lu, Opt. Lett. **40**, 2045 (2015).
359 P. Ran, L. Jiang, X. Li, B. Li, P. Zuo, and Y. Lu, Small **15**, 1804899 (2019).
360 C. Li, J. Hu, L. Jiang, C. Xu, X. Li, Y. Gao, and L. Qu, Nanophotonics **9**, 691 (2020).
361 E. J. Broadhead, and K. M. Tibbetts, Langmuir **36**, 10120 (2020).
362 E. J. Broadhead, A. Monroe, and K. M. Tibbetts, Langmuir **37**, 3740 (2021).
363 J. Bonse, Nanomaterials **10**, 1950 (2020).